

**SHEAR BEHAVIOUR OF CONCRETE BOND IN STRUCTURAL REPAIRS
UNDER FATIGUE LOADING**

by

Joanna Alice Suchta

B.Eng., McMaster University, 2014

A THESIS SUBMITTED IN PARTIAL FULFILLMENT OF
THE REQUIREMENTS FOR THE DEGREE OF

MASTER OF APPLIED SCIENCE

in

THE FACULTY OF GRADUATE AND POSTDOCTORAL STUDIES
(Civil Engineering)

THE UNIVERSITY OF BRITISH COLUMBIA

(Vancouver)

August 2020

© Joanna Alice Suchta, 2020

The following individuals certify that they have read, and recommend to the Faculty of Graduate and Postdoctoral Studies for acceptance, a thesis/dissertation entitled:

Slant Shear Testing of Interfacial Concrete Bond under Fatigue Loading

submitted by Joanna Alice Suchta in partial fulfillment of the requirements for

the degree of Master of Applied Science

in Civil Engineering

Examining Committee:

Dr. Cristina Zanotti, Civil Engineering
Supervisor

Dr. Shahria Alam, Civil Engineering
Supervisory Committee Member

Abstract

A significant portion of concrete infrastructure in North America is deteriorating and will require repair or rehabilitation action in the near future. An effective repair can be jeopardized by a bond which is unable to withstand the subjected loading and durability conditions. Fatigue loads are a cause of structural concrete deterioration and cracking with respect to service load conditions such as vehicular traffic as well as high amplitude loading events such as earthquakes and storms. Currently the response of cementitious repair interfaces tested under fatigue loading is not comprehensively examined in existing literature. In this study, the modified slant shear cylinder test with different bond plane inclinations was used to experimentally determine the bond strength of composite substrate-repair specimens subjected to monotonic and fatigue loading protocols. The effect of both roughened and near-smooth interfacial profiles is considered, as well as the use of steel fiber reinforcement in the repair material. The associated bond parameters are derived from experimental test results using previously identified predictive models and failure envelopes for concrete interfaces. 2D Digital Image Correlation (DIC) is additionally used to examine strain distributions on the surface of slant shear specimens prior to failure. A discussion on the degradation of the adhesive bonding mechanism is presented and the resulting implications on bond strength and bond parameters are examined. The interfacial bond investigation is complemented with a discussion on the limitations of the employed predictive models as well as a review of relevant code provisions and research guidelines pertaining to interfacial shear bond subject to cyclic and fatigue loads.

Lay Summary

A study on the effectiveness and durability of repairs is currently presented, founded on the critical state of deteriorating concrete infrastructure worldwide. The bond plane between an existing concrete structure and a repair material is the governing component of a repair system, however, this interface is generally the weakest component, subject to durability, and strength challenges. Although concrete continues to be studied under fatigue and cyclic loading, further investigation is required on the response of concrete-repair interfaces to enable the design of effective repairs which can accommodate fatigue and cyclic deterioration. An experimental investigation is presented on the bond strength and bond parameters obtained through slant shear testing under static loading and fatigue loading involving the application of 1000 load cycles at a 0.5 Hz frequency. A discussion on the degradation of bond strength for roughened and smooth interfaces is presented, as well as the implications of steel-fiber reinforcement.

Preface

This thesis presents the original, unpublished, independent work undertaken by the author, Joanna Alice Suchta, under the supervision of Dr. Cristina Zanotti.

Table of Contents

| | |
|---|-------------|
| Abstract..... | iii |
| Lay Summary | iv |
| Preface..... | v |
| Table of Contents | vi |
| List of Tables | x |
| List of Figures..... | xi |
| List of Symbols | xiv |
| List of Abbreviations | xv |
| Acknowledgements | xvi |
| Dedication | xvii |
| Chapter 1: Introduction | 1 |
| 1.1 Background | 1 |
| 1.2 Objective & Outline | 2 |
| Chapter 2: Literature Review..... | 4 |
| 2.1 Concrete Interfacial Shear Bond..... | 4 |
| 2.2 Parameters affecting Shear Bond..... | 6 |
| 2.2.1 Interfacial Roughness..... | 6 |
| 2.2.1.1 Roughness Quantification..... | 8 |
| 2.2.2 Fiber Reinforcement | 9 |
| 2.3 Slant Shear Test | 11 |
| 2.4 Failure Envelopes & Models | 14 |
| 2.4.1 Linear Mohr-Coulomb | 14 |

| | | |
|--|---|-----------|
| 2.4.2 | Carol Plasticity Envelope (Modified Mohr-Coulomb) | 15 |
| 2.4.3 | Austin's Polynomial Line Fitting & Griffith's Fracture Criteria | 16 |
| 2.5 | Fatigue & Cyclic Testing of Interfaces | 17 |
| 2.5.1 | Experimental Investigations..... | 17 |
| 2.5.2 | Code Guidelines & Provisions..... | 19 |
| 2.6 | Digital Image Correlation for Bond Tests | 21 |
| Chapter 3: Experimental Program | | 23 |
| 3.1 | Materials & Specimen Preparation | 23 |
| 3.1.1 | Concrete Substrate | 24 |
| 3.1.2 | Surface Preparation..... | 25 |
| 3.1.3 | Repair Mortar..... | 26 |
| 3.2 | Roughness Quantification..... | 28 |
| 3.3 | DIC Preparation | 29 |
| 3.4 | Testing Program..... | 30 |
| 3.4.1 | Monotonic Testing Protocol | 30 |
| 3.4.2 | Fatigue & Cyclic Testing Protocol | 31 |
| 3.5 | Naming Convention | 33 |
| Chapter 4: Results & Discussion | | 34 |
| 4.1 | Quantification of Interfacial Roughness | 34 |
| 4.2 | Experimental Results & Failure Mechanisms..... | 37 |
| 4.2.1 | Monotonic Testing Protocol | 38 |
| 4.2.1.1 | Shear Bond Strength | 38 |
| 4.2.1.2 | Digital Image Correlation | 39 |

| | | |
|-----------------------------------|--|-----------|
| 4.2.2 | Fatigue Testing Protocol | 42 |
| 4.2.2.1 | Shear Bond Strength | 42 |
| 4.2.2.2 | Digital Image Correlation | 44 |
| 4.2.3 | Cyclic Testing Protocol..... | 46 |
| 4.2.3.1 | Shear Bond Strength | 46 |
| 4.2.3.2 | Digital Image Correlation | 47 |
| 4.3 | Failure Envelopes & Modelling..... | 48 |
| 4.3.1 | Monotonic Testing Protocol | 49 |
| 4.3.2 | Fatigue Testing Protocol | 52 |
| 4.4 | Limitations of Failure Envelope Models | 56 |
| 4.4.1 | Limitations | 56 |
| 4.4.2 | Proposed Solution | 57 |
| 4.4.3 | Modified Envelopes | 58 |
| 4.4.4 | Validation with Previous Data | 61 |
| 4.4.5 | Modification Significance..... | 61 |
| 4.5 | Discussion Summary | 62 |
| 4.5.1 | Monotonic Testing Protocol | 62 |
| 4.5.2 | Fatigue Testing Protocol | 64 |
| 4.5.3 | Cyclic Testing Protocol..... | 66 |
| 4.6 | Codes & Design | 67 |
| Chapter 5: Conclusion..... | | 70 |
| 5.1 | Concluding Remarks..... | 70 |
| 5.2 | Recommendations for Future Work..... | 72 |

| | |
|--|-----------|
| References | 73 |
| Appendices | 78 |
| Appendix A - Slant Shear Test Results..... | 78 |
| A.1 Monotonic Loading Protocol | 78 |
| A.2 Fatigue Loading Protocol..... | 79 |
| A.3 Cyclic Loading Protocol | 80 |
| Appendix B - Monotonic DIC Strain Analysis | 82 |
| B.1 Sandblasted Plain | 82 |
| B.2 Sandblasted Fiber | 83 |
| B.3 Wirebrushed Plain..... | 83 |
| B.4 Wirebrushed Fiber | 84 |
| B.5 Strain Pattern Occurrences..... | 84 |
| Appendix C - Fatigue DIC Strain Analysis | 86 |
| C.1 Sandblasted Plain | 86 |
| C.2 Sandblasted Fiber | 86 |
| C.3 Wirebrushed Plain..... | 87 |
| C.4 Wirebrushed Fiber | 87 |
| C.5 Strain Pattern Occurrences..... | 88 |
| Appendix D - Monotonic Failure Envelope Plots..... | 89 |
| Appendix E - Modified Failure Envelopes of Validation Data | 91 |

List of Tables

| | |
|--|----|
| Table 1: Mixture Proportions and Fiber Volume Fraction, V_f , for the Investigated Materials | 24 |
| Table 2: Properties of Steel Fiber | 24 |
| Table 3: Summary of Slant Shear Testing Protocol..... | 32 |
| Table 4: Roughness Quantification of Substrate Specimens | 35 |
| Table 5: Derived Bond Parameters for Monotonic Specimens | 51 |
| Table 6: Extrapolated Tensile Bond Strength..... | 51 |
| Table 7: Derived Bond Parameters for Fatigue-Loaded Specimens..... | 54 |
| Table 8: Average Roughness and Extrapolated Friction Angle..... | 57 |
| Table 9: Updated Carol Parameters including Modified Friction Angle..... | 60 |
| Table 10: Comparison of Adhesive Strength for Cyclic/Fatigue Loading | 69 |
| Table 11: Monotonic Slant Shear Test Results..... | 78 |
| Table 12: Fatigue Slant Shear Test Results | 79 |
| Table 13: Cyclic Slant Shear Test Results..... | 80 |
| Table 14: Validation - 0% Smooth Extrapolated Bond Parameters | 91 |
| Table 15: Validation – 0.5% Steel Smooth Extrapolated Bond Parameters..... | 92 |

List of Figures

| | |
|---|----|
| Figure 1: Slant Shear Test Configuration and Stresses Developed at the Interface | 11 |
| Figure 2: Geometry of Cylinders for Slant Shear Tests (a,b,c) | 13 |
| Figure 3: Geometry of Cylinders for Slant Shear Tests (a,b,c) and Compression Tests (d) | 23 |
| Figure 4: As-Cast Specimen, Wirebrushed Specimen, and Sandblasted Specimen | 26 |
| Figure 5: (a) Insertion of Substrate into Mold; (b) Demolded Specimens | 27 |
| Figure 6: Laser Profilometry Set-Up for Roughness Quantification | 28 |
| Figure 7: (a) Slant-Shear Specimen with Stochastic Pattern; (b) DIC Set-Up | 29 |
| Figure 8: Cropped Sample Plots for Fatigue and Cyclic Tests | 32 |
| Figure 9: Slant Shear Specimen Naming Convention | 33 |
| Figure 10: Quantified Substrate Surface Profiles | 34 |
| Figure 11: Normalized Shear Bond Strength vs Roughness (Monotonic) | 35 |
| Figure 12: Monotonic Shear Bond Strength | 38 |
| Figure 13: Common DIC Strain Distributions in Monotonic Specimens | 39 |
| Figure 14: Comparison of Strain Distributions prior to Failure | 40 |
| Figure 15: Shear Bond Strength of Fatigue-Loaded and Monotonic Specimens | 42 |
| Figure 16: Applied, Normal, and Shear Stresses under Monotonic and Fatigue Loading | 43 |
| Figure 17: Strain Analysis in Monotonic Specimen and Fatigue-Loaded Specimen | 45 |
| Figure 18: Shear Bond Strength of Cyclic-Loaded and Monotonic Specimens | 47 |
| Figure 19: Linear Mohr-Coulomb Envelope for Monotonic Specimens | 50 |
| Figure 20: Carol Plasticity Envelope for Monotonic Specimens | 50 |
| Figure 21: Cohesion Parameter for Monotonic Specimens | 52 |
| Figure 22: Fatigue Envelopes for SB-P | 52 |

| | |
|--|----|
| Figure 23: Fatigue Envelopes for SB-F | 53 |
| Figure 24: Fatigue Envelopes for WB-P | 53 |
| Figure 25: Fatigue Envelopes for WB-F..... | 53 |
| Figure 26: Bond Parameters for Monotonic and Fatigue-Loaded Specimens | 55 |
| Figure 27: Modified Carol Envelope for WB-P | 59 |
| Figure 28: Modified Carol Envelope for WB-P | 59 |
| Figure 29: Modified Carol Envelope for WB-P-(F) | 59 |
| Figure 30: Modified Carol Envelope for WB-F-(F) | 59 |
| Figure 31: Carol Envelope Friction Angles, Updated for WB | 60 |
| Figure 32: Monotonic Carol Envelopes with Modification Factor..... | 62 |
| Figure 33: Comparison of Bond Parameter – CSA A23.3 & Experimental | 68 |
| Figure 34: DIC Strain Distribution – Sandblasted Plain Monotonic | 82 |
| Figure 35: DIC Strain Distribution – Sandblasted Fiber Monotonic | 83 |
| Figure 36: DIC Strain Distribution – Wirebrushed Plain Monotonic..... | 83 |
| Figure 37: DIC Strain Distribution – Wirebrushed Fiber Monotonic..... | 84 |
| Figure 38: Occurrences of Strain Modes - Monotonic | 84 |
| Figure 39: DIC Strain Distribution – Sandblasted Plain Fatigue..... | 86 |
| Figure 40: DIC Strain Distribution – Sandblasted Fiber Fatigue | 86 |
| Figure 41: DIC Strain Distribution – Wirebrushed Plain Fatigue | 87 |
| Figure 42: DIC Strain Distribution – Wirebrushed Fiber Fatigue | 87 |
| Figure 43: Occurrences of Strain Modes - Fatigue..... | 88 |
| Figure 44: Sandblasted Plain Monotonic Carol & Linear Failure Envelope | 89 |
| Figure 45: Sandblasted Fiber Monotonic Carol & Linear Failure Envelope..... | 89 |

| | |
|--|----|
| Figure 46: Wirebrushed Plain Monotonic Carol & Linear Failure Envelope..... | 90 |
| Figure 47: Wirebrushed Fiber Monotonic Carol & Linear Failure Envelope | 90 |
| Figure 48: Modified Carol Envelope - Smooth 0% Specimens..... | 91 |
| Figure 49: Modified Carol Envelope of Smooth 0.5% | 92 |

List of Symbols

| | | |
|-------------------|---|--|
| % | = | percentage |
| ° | = | degrees |
| c | = | interfacial cohesion parameter |
| f_t | = | tensile bond strength |
| GPa | = | giga-pascals unit |
| Hz | = | hertz unit |
| kg/m ³ | = | kilogram-per-cubic-meter unit |
| kN | = | kilo-newtons unit |
| mm | = | millimeters unit |
| MPa | = | mega-pascals unit |
| n | = | number of loading cycles |
| Psi | = | pounds-per-square-inch unit |
| R ² | = | coefficient of correlation |
| R _a | = | average roughness (as per Fib Model Code 2010) |
| T ₀ | = | uniaxial tensile strength defined in Griffith Fracture Criteria |
| V _f | = | volume fraction of fiber reinforcement |
| y _{max} | = | maximum surface profile height |
| \bar{y} | = | mean surface profile height |
| α | = | inclination angle of the slant shear bond plane with the vertical axis |
| μ | = | frictional coefficient |
| σ_0 | = | applied axial stress producing a failure along the bond plane |
| σ_n | = | normal stress acting perpendicular to the bond plane |
| τ_n | = | shear stress acting parallel to the bond plane |
| $\tau_{n,rough}$ | = | shear stress acting parallel to the bond plane for a rough interface |
| $\tau_{n,smooth}$ | = | shear stress acting parallel to the bond plane for a smooth interface |
| ϕ | = | internal angle of friction |
| $\phi_{original}$ | = | friction angle derived from predictive models |
| ϕ_{smooth} | = | modified friction angle for smooth and near smooth interfaces |

List of Abbreviations

| | |
|------|---|
| 2D | Two-Dimensional |
| 3D | Three-Dimensional |
| ACI | American Concrete Institute |
| ASTM | American Society for Testing and Materials |
| CEM | Cement |
| CSA | Canadian Standards Association |
| DIC | Digital Image Correlation |
| ETD | Estimated Textural Depth (as per ASTM E965) |
| FRC | Fiber Reinforced Concrete |
| GU | General Usage |
| LED | Light-Emitting-Diode |
| MC | Mohr-Coulomb |
| MPD | Mean Profile Depth (as per ASTM E1845) |
| MSD | Mean Segment Depth (as per ASTM E1845) |
| MTD | Mean Textural Depth (as per ASTM E1845) |
| PVC | Polyvinyl Chloride |
| RH | Relative Humidity |
| SB-F | Sandblasted Fiber |
| SB-P | Sandblasted Plain |
| SS | Slant Shear |
| UBC | University of British Columbia |
| WB-F | Wirebrushed Fiber |
| WB-P | Wirebrushed Plain |

Acknowledgements

I would like to express my sincerest gratitude to my research supervisor, Dr. Cristina Zanotti, for her continued guidance, support, and kindheartedness for the duration of my graduate studies as well as her invaluable expertise on concrete bonds that enabled me to complete this project.

I am greatly appreciative of the technical support provided by Mr. Doug Hudniuk, Mr. Simon Lee, Mr. Scott Jackson, Mr. Sylvain Picard, Mr. Arthur Mak, and Mr. John Wong during the entirety of my research program in both the Materials Lab as well as the Structures Lab. I also want to extend my gratitude to the Civil Engineering Department and Faculty of Applied Sciences at UBC for granting my research exemption during these unprecedented times, allowing me to complete the mechanical testing of all my specimens. To the entirety of the Civil Engineering Materials Research Group I would like to extend my appreciation and thanks for the assistance provided to me in the laboratory. To my current research group, Madhu, Bardia, Debadri, Rob, and Dr. Farhad Pargar - thank you for your support and friendship!

Finally, I would like to express my deepest gratitude to my parents, Beata and Wojciech, my sister, Marta, and my partner, Cody. Thank you for your unwavering support and motivation over the past two years.

I dedicate my thesis to my parents, Beata & Wojciech, who raised me to be the person I am today and have always supported my professional development in its various forms.

To my sister, Marta, who has always been a role model of perseverance and hard work.

And to my loving partner, Cody, for being my best friend, my source of optimism, and my unsolicited procrastination police.

Chapter 1: Introduction

1.1 Background

Concrete infrastructure in North America is deteriorating and requires effective repair and rehabilitation application. The 2019 Canadian Infrastructure Report Card suggests that a significant portion of public infrastructure is currently categorized as in poor or very poor condition, requiring rehabilitation or replacement of assets in the next 5-10 years [1]. An even larger proportion has been categorized as in “fair” condition, suggesting that as deterioration continues, if strength and durability implications are not addressed, this infrastructure will fall into the poor and very poor conditions. An examination of bridges and tunnel infrastructure in particular suggests that 12.4% of inspected assets fall into the poor or very poor category and 26.3% fall into the fair category [1].

The quality of a repair relies on the strength and durability of its interface with the pre-existing substrate. An effective repair requires a bond between the existing substrate and a compatible new material which can withstand the subjected loading and durability conditions. Beyond static failure loads, fatigue is a cause of structural concrete deterioration and cracking with respect to service load conditions such as vehicular traffic as well as high amplitude events such as earthquakes and storms [2]. Although the behaviour of concrete and cementitious materials in monolithic form has been examined subject to fatigue and cyclic loads extensively, the current literature does not comprehensively investigate the response of repair interfaces tested under fatigue loading. Notwithstanding, the interface of a substrate-repair system is typically the weakest and most vulnerable component. Therefore, in order to enable the development and design of effective concrete repairs under a variety of in-situ conditions it is appropriate to investigate interfacial bond in the context of fatigue and cycling.

Repair interfaces exist under different stress conditions in the field through applications such as jacketing or retro-fitting [3]. Although the consistency among different interfacial and bond tests is continuously being examined [4], individual test procedures can be used to examine interfacial behaviour for an isolated loading condition. The slant shear test is used to experimentally determine the bond strength of a composite specimen subjected to combined shear and compression and is generally representative of some stress conditions in the field involving shear with external confinement. Initially developed to test the strength of epoxy coatings, this test has been adapted to examine the bond strength between cementitious materials, such as substrate concretes and mortar repairs. A modified version of this test procedure, adapted to include several slant orientations, allows for the formulation of a normal/shear stress failure envelope [5]. Data from various bond tests can be included to populate the tension and pure shear portions of said envelope in place of extrapolations based entirely in slant shear data. Nonetheless, the stress criteria obtained via the simple slant shear test alone can provide significant insight into bond behaviour.

1.2 Objective & Outline

The objective of the present investigation is to determine the effects of fatigue loading on interfacial concrete bond in combined shear and compression using the slant shear test. The current works will examine the effects of a fatigue loading protocol on bond strength as well as the associated bond parameters. The impact of interfacial roughness, imparted by surface treatment, and the use of fiber reinforcement in the repair/overlay material will be considered. Furthermore, using Digital Image Correlation (DIC), the prevalent patterns in strain distributions surrounding the interface will be identified. The author will also examine whether the empirical design

approximations for shear bond subject to fatigue/cyclic loading proposed by previous researchers and code provisions are representative of the experimentally demonstrated bond capacity. To date, the substrate-repair bond has not been comprehensively discussed with respect to fatigue loading under a slant shear testing protocol [6].

The herein presented thesis comprises five total chapters. Chapter 1, *Introduction*, describes the background and objectives of the research work. Chapter 2, *Literature Review*, provides an overview of the relevant literature pertaining to interfacial shear bond, parameters affecting bond, and testing protocol. Chapter 3, *Experimental Program*, describes the methodology adopted in the current investigation for specimen preparation, roughness quantification, and slant shear testing. Chapter 4, *Results & Discussion*, presents the results of experimental investigations and mechanical tests, examines applicable predictive models, and describes existing trends identified with DIC. Finally, Chapter 5, *Conclusion*, presents the summarized findings of the investigation and provides recommendations for future related works.

Chapter 2: Literature Review

2.1 Concrete Interfacial Shear Bond

Interfacial shear bond between concretes cast at different times has been investigated extensively to allow empirical estimation of interfacial strength through design codes and guidelines. In 1966, Birkeland and Birkeland proposed a linear expression to evaluate the shear strength of concrete interfaces, based on the interface reinforcement ratio and internal friction angle [7]. The expression was adopted in reinforced concrete design codes and is recognized worldwide as the original *shear-friction theory* [7]. Typically described using a simple saw-tooth model, the theory is based purely on frictional resistance of an interface involving compressive clamping forces generated by interfacial reinforcement and induced by dilation of the joint [6], [7]. Through the years, the shear friction theory has been extended to include an explicit parameter for “cohesion”. The updated *modified shear friction* theory by Mattock & Hawkins and subsequent *extended shear friction* theory, developed by Randl for Fib Model Code 2010, identify three primary bonding mechanisms: cohesion, friction, and dowel action requiring steel reinforcement or connectors across the interface [6].

Cohesion can be accepted as a interfacial material property consisting of mechanical interlock as well as adhesive bonding [3], [6]. For the purpose of macro-considerations and design expressions it is convenient to examine cohesion and adhesion as a single bond mechanism, an overstrength beyond frictional capacity. However, some research examines bond-adhesive and bond-cohesive as two distinct interfacial mechanisms. Espeche & Leon suggest that where bond-adhesive depends on the soundness, cleanliness, and roughness of the substrate, cohesive-bond is related to the porosity and structure of the interfacial transition zone in an overlay concrete [3]. Sadowski defines adhesion specifically as the force of energy necessary to separate two bodies

and outlines three principle adhesive sub-mechanisms: interlocking by friction and dovetailing, physical bonding of *van der waals* forces and chemical bonding through ionic bonding [8].

Randl's description of cohesion, as included in the extended shear friction theory, examines the parameter through both an adhesion component, which is a function of chemical/physical bonding at the interface, as well as a mechanical interlocking component [6]. Chemical and physical bonding capacity, related to interfacial *van der waals* forces, is supported by material composition and porosity, but is moreover highly dependent on the effective contact area of an interface. The surface contact area, described by a "modified Wenzel coefficient" is related to surface wetting behaviour and the relationship between interfacial roughness and hydrophobicity [6]. In the second component, micro-mechanical factors such as localized fracturing, interlocking, overturning, are also engaged by interfacial roughness [6], [9]. Zanotti and Randl have suggested that interlocking and overriding are active only in roughened interfaces [4], [6], [9]. For the current works the definition of cohesion discussed herein, and adopted by Randl & Zanotti, will apply.

Frictional bond resistance is related to interfacial roughness and requires compression or confinement of the interface. Compressive forces perpendicular to the interface may be applied externally or through a resultant clamping mechanism generated by interfacial reinforcement, connectors, or shear studs. The frictional resistance developed is proportional to the applied compressive force. Generally, a rougher interface is associated with a higher frictional force due to increased aggregate interlock [6]. The use of reinforcing steel bars or connectors at an interface is a common strengthening application for concrete interfaces and often induces a more ductile failure along the interface. The use of reinforcement engages clamping forces through joint dilation for additional normal stresses and activates a dowel action mechanism. Nonetheless, the use of steel reinforcement across the interface it is not examined in the present study. As such, a brittle

behaviour or rigid bond slip is anticipated, which can accommodate only minimal shear slips at the interface prior to bond failure [6].

Although the abovementioned bonding mechanisms are distinct in nature with individual impacts on interfacial behaviour, researchers suggest that there is indeed interaction of bond resistance mechanisms and that these mechanisms can work in unison [4], [6]. The degree of activity of each mechanism and extent of interactions is dependent on the composition of the interfacial system and will be examined further in the current investigation.

2.2 Parameters affecting Shear Bond

2.2.1 Interfacial Roughness

Interfacial roughness, typically imparted by surface treatment of the concrete substrate, is related to both the adhesive/cohesive capacity of the interface, as well as an increased frictional capacity. As identified previously, a deciding parameter of the adhesive bonding mechanism is the real surface contact area along the bond plane. As interface roughness increases, the physical surface area of the profile expands, thereby increasing the contact area capacity for surface wetting [6]. In a study on roughness and friction angle, Mohamad and Ibrahim similarly suggest that the surface roughness affects both the angle of internal friction as well as the cohesion value due to the increase in surface area for cohesion bonding to occur along the interface [10]. Secondly, the impact of localized mechanical effects attributed to adhesion, such as fracturing, interlocking, and crushing, are also highly dependent on roughness and interfacial tortuosity [4], [6], [9]. As noted, some of these micro-mechanisms are only active in roughened interfaces, engaged by asperities along the surface profile.

Regarding frictional capacity, an increase in interfacial roughness is generally associated with an increase in the frictional coefficient derived for a bond plane [3]. It would follow, then, that an increase in roughness is also associated with an increase the extrapolated internal angle of friction. In Espeche & Leon an increase in friction angle was observed with increasing substrate roughness but it is important to note that all specimens considered were deemed “rough” [3]. The literature does not extensively discuss differences in extrapolated friction angles when related to smooth interfaces (low roughness value) and rough interfaces (high roughness value), although suggested values for internal friction angles are recommended in [3] and [11].

The roughness of an interface also has been shown to impact other bond properties. In Zanotti et al, the use of steel fibers in the overlay was examined in conjunction with smooth and roughened interfaces tested under a slant shear set-up [9]. Although smooth interfaces did not result in significant benefits from fibers, roughened interface exhibited strength increases as well as increases in extrapolated cohesion values. The investigation suggested that with enough engaged substrate roughness, a micro- “dowel effect” occurred at the interface, associated with the stiffness of the steel fibers. The study suggested, that, on account of profile roughening encouraging deviation of the fracture plane into the repair material, fibers were able to cross the shifted plane and more effectively connect the repair to the substrate. Overall, roughness increased steel fiber efficacy, thereby increasing the associated cohesion parameter of the bond. Similar strength and cohesion increases were presented by Zanotti & Randl [4]. Previous research therefore suggests that interfacial roughness, through profile tortuosity, engages fiber-induced benefits which are not necessarily active in a smooth profile.

2.2.1.1 Roughness Quantification

Different quantification systems can be used to quantify the surface profile roughness for use in empirical expressions evaluating interfacial bond strength. A common method for profile quantification used in the field is the Sand Patch Test as per ASTM E965 which provides a “Mean Textural Depth” (MTD) quantifier. This procedure is generally used to determine the average depth of a pavement surface macrotexture and involves the application of a known quantity of consistently graded sand to the surface, which is compacted and spread using a smooth disc tool, followed by a measurement of the diameter of the resulting sand [12]. MTD is calculated using a volumetric calculation, based on the concept of an “idealized cylinder” created along the surface profile. This method has been used in previous research on concrete bond to quantify roughness [4]. The main limitation of this method is that only one roughness parameter can be derived for a tested profile.

As an alternative to a physical, contact-oriented quantification method, non-contact laser profilometry may also be used to measure the exact topography and depth of a surface profile, and has been demonstrated previously at the University of British Columbia [13], [14]. Based on the acquired profile, different methods can subsequently be used to quantify surface roughness. As an extension of the contact Sand Patch Test, ASTM E1845 provides guidelines to calculate the “Estimated Texture Depth” (ETD) from a two-dimensional surface profile [15]. A transformation equation is required to transform the calculated Mean Profile Depth (MPD) to the three-dimensional surface contact-oriented method of ETD, which is compared to the MTD obtained through the Sand Patch Test method. The MSD can be evaluated from laser profilometry data and subsequently converted into an ETD value.

The following procedure is adapted from [15] and applies to a segment along a surface profile of approximately 100mm length:

$$\text{Mean Segment Depth (MSD)} = \frac{\text{Peak Level 1} + \text{Peak Level 2}}{2}$$

$$\text{Peak Level 1} = y_{\max} - \bar{y} \text{ for } 0 \leq x < 50 \text{ mm}$$

$$\text{Peak Level 2} = y_{\max} - \bar{y} \text{ for } 50 \leq x < 100 \text{ mm}$$

$$\text{Mean Profile Depth (MPD)} = \frac{1}{n} \sum_{i=1}^n \text{MSD}_i$$

$$\text{ETD} = 0.2 + 0.8 \text{ MPD}$$

Finally, a quantifier outlined in Fib Model Code 2010 called the “Average Roughness” is defined as the average deviation of the surface profile from a mean line and can be calculated based on the following formula for the data points obtained with laser profilometry [13]:

$$\text{Average Roughness (R}_a\text{)} = \frac{1}{l} \cdot \int_0^l |y(x) - \bar{y}| \cdot dx \approx \frac{1}{n} \sum_{i=1}^n |y(x) - \bar{y}|$$

$$\bar{y} = \frac{1}{l} \cdot \int_0^l y(x) \cdot dx \approx \frac{1}{n} \sum_{i=1}^n y_i$$

$$l = \text{the assessment length}$$

$$y(x) = \text{profile height at position } x$$

Average roughness, R_a , is one of the most common quantifiers of interfacial roughness according to Espeche & Leon [3].

2.2.2 Fiber Reinforcement

The use of fiber reinforcement in concrete and cementitious materials has demonstrated improvements in crack growth impact and fatigue resistance. The research of Mindess and Banthia

et al attributed these enhancements to the ductility of some types of fibers, such as steel, and their ability to maintain stress transfer capability across a crack. [16], [17]. In the context of a fiber reinforced repair material, Zanotti et al suggested that the strength and durability of the bond is improved in the following ways [5]:

- Decrease in concrete/mortar bleeding
- Reduced pre-damage due to handling and shrinkage
- Greater energy and load required for cohesive failure
- Frictional failure at smaller crack separation and damage requiring higher energy and load compared to plain

However, Zanotti & Randl suggest that the impact of fiber reinforcement on bond strength can depend on different factors, such as interfacial roughness, material properties, stress conditions and fiber properties [4]. As previously outlined, in roughened interfaces, the use of steel fibers in the repair mortar resulted in an increase in the cohesion parameter extrapolated from the deduced failure envelope. Notable bond strength improvements were exhibited primarily in specimens with a lower applied compressive stress and therefore less engaged frictional resistance [4].

Regarding a fracture mechanics approach, the use of fibers has been suggested to increase the fracture resistance of the repair material, thereby improving the fracture properties of the overall interface [9]. Zanotti et al suggest that the use of fibers may encourage deviation of the “fracture plane” from the actual bond plane towards a more cohesive type of fracture. As such, the extrapolated frictional values may be slightly reduced [9]. Although slight changes have been reported with steel fibers, they are considered a second order effect and may be caused by a change in the cohesion value [5].

2.3 Slant Shear Test

A slant shear test is often recommended by standards to assess the strength of a repair bond in place of more challenging tensile bond tests [5]. A compressive load is applied to a composite cylinder in which the overlay and substrate material are bonded together on an inclined plane. Interfacial shear and normal stresses can be evaluated from the stresses at failure based on the inclination orientation of the specimen. With reference to Figure 1:

$$\tau_n = \frac{1}{2} \sigma_0 \sin (2\alpha) \quad (1)$$

$$\sigma_n = \sigma_0 \sin^2 \alpha \quad (2)$$

σ_0 is the applied axial stress that produced failure along the bond plane

σ_n is the normal stress acting perpendicular to the bond plane

τ_n is the shear stress acting parallel to the bond plane

α is the inclination angle of the bond plane with the vertical axis

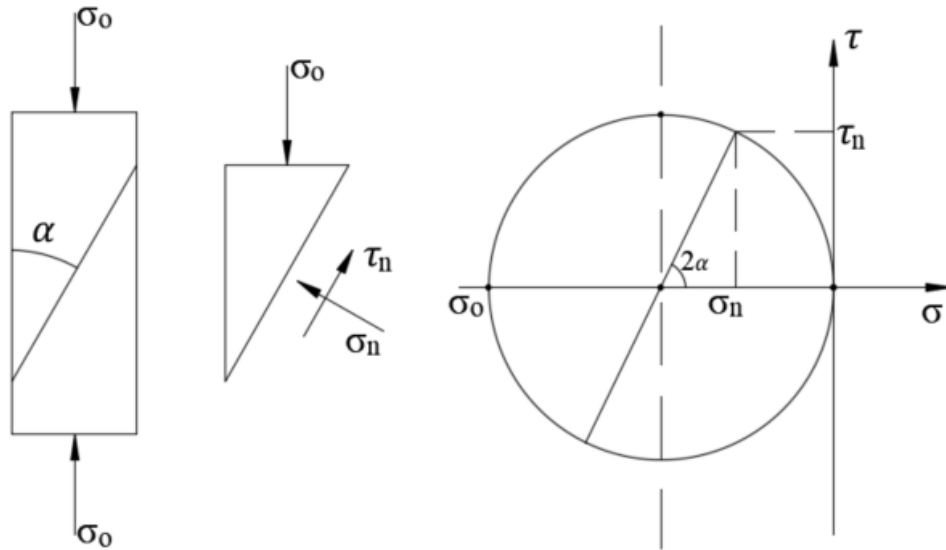


Figure 1: Slant Shear Test Configuration and Stresses Developed at the Interface

The original Slant Shear test according to ASTM C882, originally developed for the evaluation of bond strength between concrete and epoxy-resins, recommends a single interfacial inclination of 30° to the vertical [18]. However, Austin et al discuss the limitations of using a single slant shear orientation in [11]. Based on the investigation of a critical bond angle, or the bond angle at which the load required to produce a bond failure is at the minimum, it was suggested that the development of a bond failure in a slant shear specimen is dependent on bond plane inclination as well interfacial roughness [11]. The likelihood of obtaining a bond failure with the standard specimen inclination of 30° is reduced due to the stress distribution along the interface. This limitation is further emphasized in specimens with rougher interfaces which were shown to have a lower critical bond angle and are predominantly under greater applied normal stresses and therefore engage substantial frictional resistance [11]. It was concluded that a single interfacial inclination is representative of only a single proportion of shear to normal stresses along the bond plane (“stress state”), as such the bond information produced does not provide the full picture.

Based on these limitations, Zanotti et al developed a variable bond angle approach for slant shear testing and cylindrical specimens with three different geometries were adopted [5]. The same testing protocol will be adopted in the current works. In addition to the standard bond plane inclination of 30° , angles of 25° and 20° to the vertical are used to provide information on different interfacial stress states. In order to maintain a consistent bond contact area amongst the three types of orientations, the diameters of the cylinders were modified. Additionally, the height of the overall cylindrical specimens was modified to include a diameter’s distance between the loading edge of the cylinder and the start of the interfacial plane. This height modification was adopted to ensure uniform stress transfer from the loading plates to the bond plane, and to avoid frictional effects of loading plates resulting in an undesirable tri-axial stress distribution [5]. The dimensions adopted

by Zanotti et al, and used in the current investigation, are presented in Figure 2. Standard testing protocol involves the substrate portion of the specimen to be oriented on the bottom and the repair/overlay layer is oriented on the top.

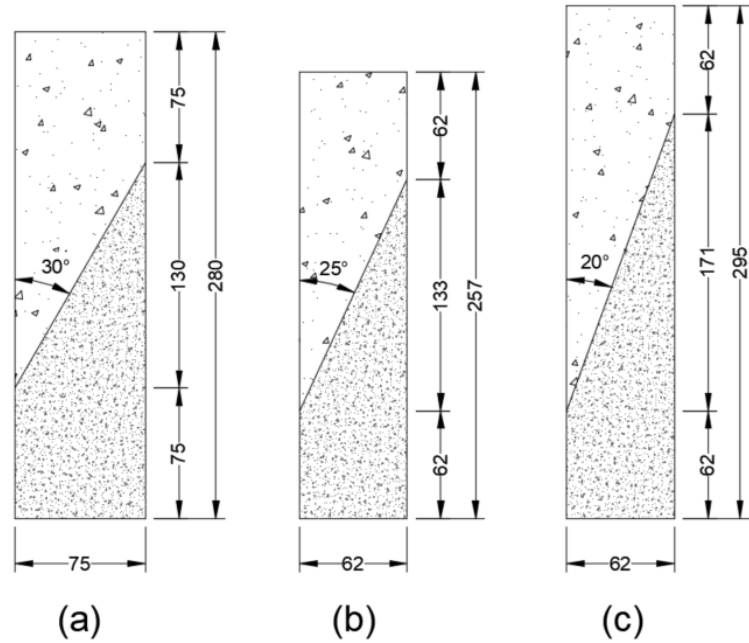


Figure 2: Geometry of Cylinders for Slant Shear Tests (a,b,c) [All dimensions in mm]

Adoption of three slant shear inclinations allows for investigation of several stress states along the bond plane. Investigation of different stress states can provide insight into bonding features which are otherwise not evident in other stress states. For example, the 30° orientation results in the largest compression-shear ratio at the interface, generating a large degree of friction and interlocking, however the 20° orientation has the least frictional contribution and largest “pure shear” or adhesive/cohesive contribution. Furthermore, the experimental data can be used to characterize shear bond strength as a function of normal interfacial stresses through the application of several failure envelopes via regression (line fitting). Through development of failure envelopes, the cohesion and internal friction angle bond parameters can be extrapolated.

2.4 Failure Envelopes & Models

Using a minimum of three slant shear inclinations, a failure envelope outlining shear stress in terms of applied normal stress can be applied via line fitting and can be extended to examine the interfacial repair-substrate bond behaviour in tension and pure shear beyond the combined shear-compression information provided via experimental investigation. Compression is assumed to be positive in the following discussion and presented predictive models.

2.4.1 Linear Mohr-Coulomb

The Mohr-Coulomb (MC) failure envelope, adapted to concrete shear bond from traditional rock mechanics, describes a linear relationship between normal stress and shear stress at a cementitious interface. Fitting of experimental data can provide a linear approximation that allows extrapolation of the cohesion of the interface (y-intercept) and the friction angle of the interface (slope):

$$\tau_n = c + \mu \sigma_n = c + \tan\phi \cdot \sigma_n \quad (3)$$

τ_n is the evaluated shear stress acting parallel to the bond plane

σ_n is the normal stress acting perpendicular to the bond plane

c is the interfacial cohesion

μ is the frictional coefficient and $\mu = \tan\phi$

ϕ is the internal angle of friction

Previous researchers have commented that, through the study of rock mechanisms, the linear MC envelope tends to overestimate shear strength in the tensile region [11]. Espeche & Leon also suggested that the tensile strength obtained through MC is almost always overestimated [3].

2.4.2 Carol Plasticity Envelope (Modified Mohr-Coulomb)

Using Carol's Theory of Plasticity Espeche and Leon proposed a modified Mohr-Coulomb envelope by incorporating a hyperbolic curve at the end of the linear approximation [3]. Carol's paper is an extension of a frictional/dilatant model for normal/shear cracking in quasi-brittle materials adapted to be implemented as a constitutive law for interfacial elements [19]. Extending from Carol's fracture mechanics approach, the modified envelope incorporates a representative cracking envelope, involving evolution towards a "cracked" interface, to the traditional MC criterion [3]. The authors suggest that this modified envelope more accurately describes tensile behavior in order to provide a more realistic representation of bond strength at the interface [3]. The Carol Plasticity Envelope is presented below assuming compression to be positive:

$$\tau_n = \sqrt{(c + \sigma_n \cdot \tan\phi)^2 - (c - f_t \cdot \tan\phi)^2} \quad (4)$$

τ_n is the evaluated shear stress acting parallel to the bond plane

σ_n is the normal stress acting perpendicular to the bond plane

c is the interfacial cohesion

ϕ is the internal angle of friction

f_t is the tensile bond strength of the interface

The Carol envelope can incorporate experimentally determined values for tensile strength. Nonetheless, in place of experimentally derived strength, Zanotti & Randl suggested a relationship between tension and cohesion for interfaces roughened using sandblasting surface preparation [4]:

$$c = 2.8 \cdot f_t$$

Austin et al describe a relation for smooth interface, derived from Griffith's fracture criteria [11]:

$$c = 2.0 \cdot f_t$$

The current investigation will apply the Carol plasticity envelope by incorporating these relations in place of experimentally derived tensile bond strength data:

$$\tau_{n,rough} = \sqrt{(c + \sigma_n \cdot \tan\phi)^2 - \left(c - \frac{c}{2.8} \cdot \tan\phi\right)^2} \quad (4a)$$

$$\tau_{n,smooth} = \sqrt{(c + \sigma_n \cdot \tan\phi)^2 - \left(c - \frac{c}{2} \cdot \tan\phi\right)^2} \quad (4b)$$

2.4.3 Austin's Polynomial Line Fitting & Griffith's Fracture Criteria

Austin et al examined experimental slant shear results with best-fit second order polynomial curves [11]. As a function of the normal stress, the y-intercept value of the polynomial curve allows extrapolation of the “cohesion” value of the bond plane. However, a frictional coefficient is not defined. In the same study, an approach involving Griffith's fracture criteria for brittle materials was examined in order to provide a more accurate representation of the tensile portion of the envelope. The form of this envelope is more consistent with the Carol model; however, it also does not provide a parameter for frictional coefficient [11]:

$$\tau^2 = 4 \cdot T_0 (\sigma_n + T_0) \quad (5)$$

τ_n is the evaluated shear stress acting parallel to the bond plane

σ_n is the normal stress acting perpendicular to the bond plane

T_0 is uniaxial tensile strength [*pure shear strength* = $2 T_0$]

It is important to note that the authors describe pure shear strength in terms of uniaxial tensile strength. Pure shear strength is interpreted in the current investigation as the “cohesion” parameter described by the other models. Furthermore, the authors suggest that although Griffith fracture criteria is not applicable to soil and rocks, the fracture mechanics approach may be more

suitable for concrete and cementitious materials [11]. Nonetheless, the limitation of both the Austin and Griffith models for the current experimental investigation is that a frictional coefficient or friction angle is not defined in either equation. Therefore, only the cohesion can be extrapolated.

Based on the models adopted by previous researchers and consistency of derived parameters it was selected to focus primarily on the Linear MC and Carol Plasticity Theory envelopes via linear and nonlinear regression for the current investigation.

2.5 Fatigue & Cyclic Testing of Interfaces

2.5.1 Experimental Investigations

Fatigue and cyclic loading of monolithic plain concretes, reinforced concretes, and fiber reinforced concretes have been studied previously and in detail. These studies will not be discussed herein for the purpose of brevity, but relevant to the current investigation, it has been demonstrated that the interfacial bond between fibers and cementitious matrix in FRC is subject to fatigue bond degradation as is the interfacial bond between reinforcing bars and the cementitious matrix [20], [21]. Cao & Chung studied the degradation of the bond between concrete and rebar and suggested that a higher applied stress range caused significant bond degradation and resulted in bond failure at a lower number of cycles [20]. Furthermore, Li & Matsumoto, who examined fatigue damage at the fiber-matrix interface in flexural specimens in a crack growth and fracture mechanics context, suggest that the use of fibers can lead to fatigue crack arrest, and that fibers may be effective in extending the fatigue life of concrete structures [21].

Tassios and Vintzeleou examined concrete-to-concrete friction along cracked interfaces (no adhesion) subject to cyclic push-off tests. Shear stiffness of the interface under cyclic loading was found to degrade significantly in rough interfaces but not noticeably in smooth interfaces, and

was attributed to repeating deterioration of interfacial asperities due to cutting off of aggregate peaks in the rough surface [22]. Hu, Li, and Liu examined slant shear specimens subjected to quasi-static and dynamic loading while considering strain rate effects, the slant angle, surface roughness, and age of interfaces on bond behaviour [23]. The researchers suggested that where the strain rate and slant angle had significant influence on the failure modes, the effects of surface roughness and interface age were not significant. The experimental results suggested that although the strain rate had a great effect on the slant shear bond strength, an increase in strain rate was not necessarily proportional to greater damage [23]. Finally, Figueira et al examined the effects of cyclic loading on steel reinforced interfaces subject to a shear push-off test to reproduce an interfacial conditions between precast beams and a cast-in-place slabs [24]. Different cyclic stress range protocols in the form of low, medium, and high amplitude tests were conducted until specimen failure or one million load cycles. The researchers suggested that as the applied stress amplitude decreases there is an increase in the number of resisting load cycles. Although the interfaces examined in the study are of a more ductile nature due to the interfacial reinforcement, significant insight was provided into the preparation of a cyclic and fatigue loading protocol.

Additional studies on fatigue loading of concrete and cementitious interfaces have been conducted which are relevant to the current investigation. The relevant methodologies and observations are presented:

- Cyclic loading of beams overlaid with fiber reinforced mortar to represent wheel-loading stresses. Loads were cycled between a minimum of 1 kN and a maximum of 45-65% of the static flexural strength at a frequency of 5 Hz (100,000 cycles) [25].

- Cyclic loading of FRC repaired corroded RC beams suggesting that fatigue life is directly related to load range and at 75% of the static strength the rate of loading strongly influences the fatigue strength through creep effects [26].
- Walraven et al examined cyclic push-off tests with a repeating sinusoidal wave at 1 Hz frequency alternating between 46% and 66% of ultimate load to confirm whether an expression for monotonically derived tests is applicable for specimens subjected to cyclic loading. The results suggested that cyclic loading did not influence shear capacity [27].

Regarding the specific loading regimes presented in the literature for cyclic and fatigue testing of interfacial concrete, minimum and maximum load limits are typically based on a percentage of the static load strength. Fatigue testing is typically performed using a sinusoidal wave function at a frequency of 1 Hz or greater until specimen failure or a predefined cycle limit. Details on previous cyclic and fatigue investigations are as follows:

- Ong applied a minimum of 1 kN cycled to 45%, 55%, and 65% of ultimate static load at 5 Hz frequency to a limit of 100,000 cycles [25]
- Anderson applied fatigue loads at frequency of 2 Hz up to 1 million cycles [26]
- Naderi applied a minimum of 10% and maximums of 40%, 60%, and 80% of the static load under a 0.5 Hz frequency sinusoidal wave to a limit of 50,000 cycles or failure [28]
- Daud applied a minimum load of 15% to maximum load of 70% and 80% the static strength at a frequency of 1 Hz [29]

2.5.2 Code Guidelines & Provisions

Although specific protocols for fatigue and cyclic loading of cement-based slant shear specimens are not explicitly described in codes, discussions on cyclic and fatigue loading are presented and can be adapted to suit the current experimental investigation. ACI 215R for the

design of concrete structures subjected to fatigue loading describes low-cycle fatigue protocols as consisting of less than 100 cycles and fatigue protocols as consisting of greater than 1000 cycles [2]. Similarly, ACI 408.2R for the Bond of Steel Reinforcing Bars under Cyclic Loads suggests two types of loading regimes. Low cycle, high stress is representative of earthquake loads and requires high loads with a low number of cycles, specifically less than 100 [30]. This ACI report also suggests that stress reversals from tension to compression are required for true earthquake conditions. However, fatigue loading involves unidirectional loading at a low load with a higher number of cycles ($n > 100$) [30]. Additional guidelines and from relevant reports and associations are as follows:

- ACI 215R-74 suggests that variations of frequency of loading between 1.2 Hz – 15 Hz have little effect on fatigue strength, provided that the maximum applied stress is less than 75% of the static strength of a specimen/structure [2].
- ACI 437R and ACI 47.1R require a minimum of six loading/unloading cycles for cyclic strength evaluation of existing concrete buildings and concrete structures [31], [32].
- ACI 544.9R17, the Report on Measuring Mechanical properties of Hardened Fiber-Reinforced Concrete, suggests applying a higher maximum stress with a small number of cycles and at a lower loading rate. Similarly, a lower maximum stress for a large number of cycles should be applied at a higher loading rate. This report outlines the possibility of concrete strength gain with time when performing long-duration cyclic tests [33].
- ASTM E2126 for Cyclic Testing of Vertical Elements of the Lateral Force Resisting Systems for Buildings suggests a loading rate of 0.2 to 0.5 Hz [34].
- Finally, although shear resistance of repair interfaces subjected to fatigue loading has not been investigated comprehensively [6], researchers have presented simplified design

approaches to account for these conditions. According to Randl, adhesive bond should be reduced to 50% under cyclic loading for rigid bond [6]; Mattock suggests that the shear strength of a concrete-to-concrete interface under cyclic loading should be taken equal to 0.9 of the shear strength under monotonic loading for monolithic specimens and rough interfaces; if bond between concrete parts is nonexistent (i.e. pure sliding) the shear strength under cyclic loading should be taken as 0.6 of the shear strength under monotonic loading [35].

2.6 Digital Image Correlation for Bond Tests

Digital image correlation is a non-contact optical technique adopted for the analysis of surface displacements [36]. A high frequency digital camera is employed to capture images of the specimen surface before and after the occurrence of deformation. Displacements are tracked from an un-deformed reference image to a deformed image. According to Shah & Kishen, an image is represented by a discrete function which describes the grey level of each of the pixels contained within the image [36]. The discrete function representing the reference or un-deformed image is transformed into another discrete function after deformation occurs. Correlation calculations evaluate the displacements between groups of pixels (“patterns”) amongst the two images on the basis that within each pattern of pixels the displacement field is assumed to be homogeneous [36]. The grey level of pixels is activated with a stochastic pattern applied to specimen surface. A virtual mesh is generated and DIC software is able to calculate strain tensors as well as other relative deformation parameters.

Although DIC is widely applied to measurements of displacements in various fields, the technique is often adopted for concrete specifically to allow direct observation of the cracking and

fracture processes, which can be brittle and abrupt in nature and hard to capture with the human eye [36], [37]. A stochastic pattern is typically applied with white and black spray paint using a speckling effect. 2D DIC can be used to measure displacement, stress intensity of cracks, as well as stress and strain behavior of a specimen undergoing testing [36]-[39]. In the current study 2D Digital Image Correlation is used in a qualitative method to examine the strain patterns of specimens subjected to monotonic, fatigue, and cyclic loading protocol prior to failure.

Chapter 3: Experimental Program

3.1 Materials & Specimen Preparation

The slant shear test was the primary experimental methodology undertaken in the presented investigation. Compression tests were also conducted as per ASTM C39 [40] to determine the 28-day strength of the substrate and repair/overlay materials on cylinders of 75mm diameter and 150mm height. Dimensions of slant shear and cylindrical specimens are presented in Figure 3.

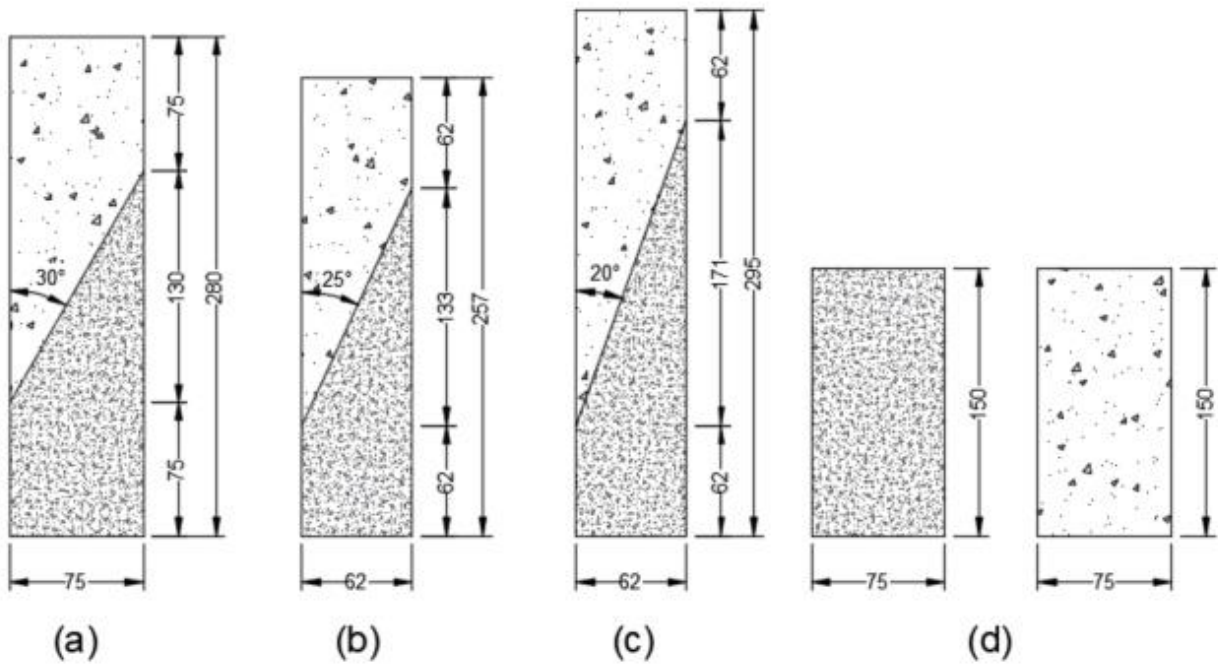


Figure 3: Geometry of Cylinders for Slant Shear Tests (a,b,c) and Compression Tests (d) [All dimensions in mm]

A single normal strength concrete substrate was maintained for all specimens. The substrate was treated with two surface preparation methods to impart different degrees of interfacial roughness. The repair mortars were also normal strength and were applied to the substrate with and without fiber reinforcement. A table of the three mixed designs used is presented in Table 1. A volume fraction of $V_f = 0.5\%$ of 13mm long, straight uncoated steel fibers was

selected, based on previous investigations in [9] and [4]. Table 2 presents the properties of the steel fiber. Accounting for a minimum of three replicates for each specimen type in addition to extra replicates, a total of 144 slant shear specimens were prepared, comprising of four material and surface preparation types encompassing three slant shear inclinations and allocated to three types of loading protocols.

Table 1: Mixture Proportions and Fiber Volume Fraction, V_f , for the Investigated Materials

| | GU CEM [kg/m ³] | Fly Ash Type F [kg/m ³] | Sand [kg/m ³] | Aggregate [kg/m ³] | Water [kg/m ³] | V_f [%] |
|-------------------------|--------------------------------|--|------------------------------|-----------------------------------|-------------------------------|-----------|
| Substrate | 450 | - | 1165 | 776 | 189 | - |
| NS Repair – 0% | 840 | 210 | 1680 | - | 420 | - |
| NS Repair – 0.5% | 840 | 210 | 1680 | - | 420 | 0.5 |

Table 2: Properties of Steel Fiber

| Diameter [mm] | Length [mm] | Tensile Strength [MPa] | Elastic Modulus [GPa] |
|------------------|----------------|------------------------------|-----------------------------|
| 0.21 | 13 | 2750 | 200 |

3.1.1 Concrete Substrate

To avoid potential damage and microcracks along the interface induced by cutting or sawing of cylindrical specimens, substrates were pre-cast at inclinations using a machined PVC slant shear “insert” form. After installing the inserts inside the cylindrical slant shear (SS) molds, the molds and inserts were oiled, and the substrate concrete was placed into the molds in three layers. After placing each layer, the material was tamped 25 times as suggested by ASTM guidelines and vibrated for a total of two minutes. After all the three layers were cast, tamped, and vibrated, the top of the mold was rodded and rolled to level and smooth the surface. Specimens

were covered with a polyethylene sheet for 24 hours in standard lab conditions and subsequently demolded. The specimens were then placed in a humidity-controlled curing room with relative humidity maintained at 50%. Cylindrical compressive specimens were also cast alongside the slant shear specimens. These specimens were tested for compressive strength after 28-days as per ASTM C39 [40] under a load-controlled rate of 0.250 MPa/second.

3.1.2 Surface Preparation

In order to impart varying degrees of interfacial roughness and examine the effects of roughness on fatigue and cyclic loading, sandblasting and light wirebrushing were selected as surface preparation methods. Sandblasting was used to generate a medium rough to rough interface with exposed aggregates along the bond plane in similar fashion to previous research conducted at UBC [4], [9]. An initial round of sandblasting took place three weeks after initial casting, prior to specimens reaching full strength (specimen ages 21-24 days). A sandblasting unit, in the form of a modified pressure washer, was used with an abrasive medium to expose the aggregates in the substrate at a pressure of 4000 psi or 27.6 MPa. A second round of sandblasting occurred 7 weeks after casting to impart additional roughness on the specimens. Wirebrushing was selected to generate an essentially smooth interface. Light abrasion in the form of wirebrushing was selected to remove potential surface laitance in comparison to a left “as-cast” substrate. Wirebrushing took place three weeks after initial casting (specimen ages 22-25 days). A steel wire-brush attachment on a battery-powered drill was used to brush and scour the interface of a clamped specimen for a set period of time depending on the interfacial contact area. Figure 4 presents two specimens having undergone the surface preparation methods in comparison to an “as-cast” specimen.



Figure 4: [From left-to-right] As-Cast Specimen, Wirebrushed Specimen, and Sandblasted Specimen

In addition to surface preparation, the ends of the substrate were grinded before the 28-day period. Specimens were removed from the humidity-controlled curing room in order to undergo surface preparation. Upon completion they were returned to the curing room and allowed to age until the scheduled repair casting.

3.1.3 Repair Mortar

In order to represent aged infrastructures, the author opted to allow the substrate to age beyond 28-days. The repair mortar was cast when the substrate specimens were 10 weeks or 70 days old. 24 hours prior to casting, the substrate batch was removed from the curing room and allowed to dry in standard laboratory conditions. The goal was to achieve specimens which were dried-back from a saturated surface dry condition at the time of repair application, as indicated in [41]. The specimens were cleaned with compressed air and carefully inserted into lightly oiled

cylindrical molds to avoid contamination of the interface with any oil. Normal strength plain mortar and normal strength fiber reinforced mortar were used as the repair material. During casting of the mortars, dry material was first mixed to allow for distribution of materials before adding water. For the fiber-reinforced batches, steel fibers were incrementally added once the initial plain mortar was well mixed. In a similar fashion to the substrate, the repair mortars were placed in three separate layers on top of the substrate, cast in a vertical direction. After each layer the material was tamped 25 times and vibrated for 30 seconds. The repair material was much more flowable than the substrate. After the third and final layer the specimens were rolled and levelled, and subsequently covered with a polyethylene sheet for 24 hours in standard laboratory conditions. The specimens were carefully demolded the next day and placed in the humidity-controlled curing room to await testing. Extra attention was given to the particularly delicate wirebrushed specimens, in order to avoid interface damage and specimen breakage during the demolding process. Prior to testing, the repair portion of the specimens were also grinded as required.

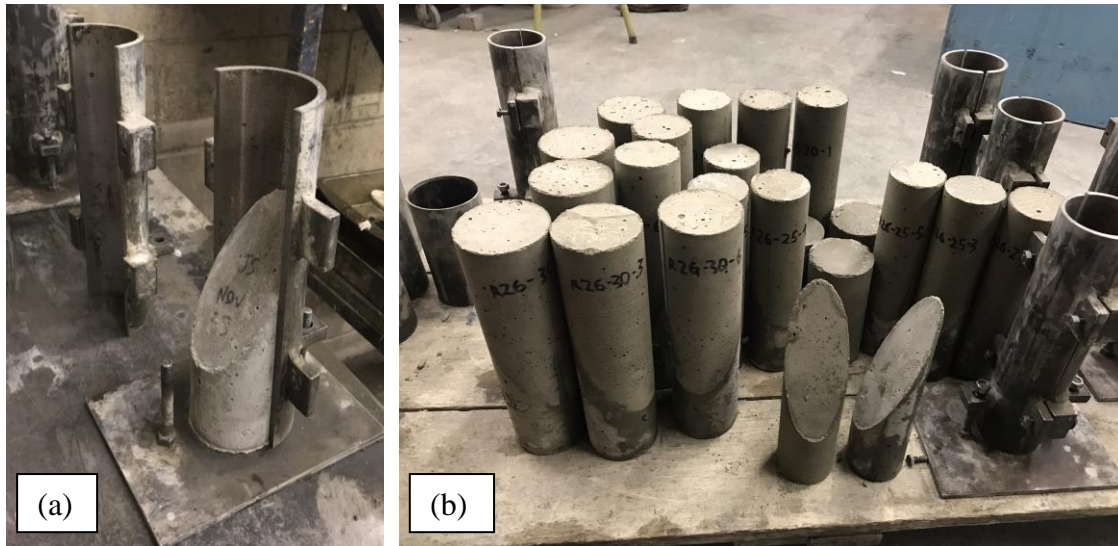


Figure 5: (a) Careful Insertion of Substrate into Mold prior to Repair Casting; (b) Demolded Specimens

3.2 Roughness Quantification

In advance of repair layer casting, the roughness profile of each of the substrate specimens was quantified using 2D laser profilometry with a *Microtrack 3 Laser Scanner*. The substrate specimens were fixed in front of and perpendicular to the laser unit, within an appropriate optical range. The laser was fixed on a plate attached to a linearly translating rod at the slowest speed setting, adapted from a traditional fiber pull-out set-up. The profilometry set-up is presented in Figure 6. A single profile line along the entire interfacial length of each the specimens was captured by the translating laser which would record the depth of the point of the profile from the laser. Therefore, the peaks of the profile were characterized by the minimum values of the laser depth and the valleys of the specimen profile were characterized by the maximum values of the laser depth. Data was acquired at a rate of 100 samples/second and will be used for surface roughness quantification using the methods discussed in Section 2.2.1.1. A single line of quantification was selected for all specimens to ensure consistency of surface preparation methods instead place of a more rigorous profile quantification of a select few representative specimens.



Figure 6: Laser Profilometry Set-Up for Roughness Quantification

3.3 DIC Preparation

Before slant shear testing may commence, a stochastic pattern must be applied to the surface of the specimens to engage Digital Image Correlation software via appropriate groupings of pixels in greyscale. A stochastic pattern was applied to the front surface of the cylindrical specimens in the form of spray paint speckling. First, a layer of white matte spray paint was applied to create an even base with maximum contrast. Next, using a “speckling” technique with black matte spray-paint, a stochastic pattern is applied to the surface of the specimen. A failed specimen with a clearly defined stochastic pattern via speckling is shown in Figure 7(a). Based on the literature, the camera is installed 1 – 2m from the specimen with consistent illumination of the specimen surface[36]–[39]. As such, the high-frequency camera used for acquisition of DIC sequences was set-up approximately 1 meter from the tested specimen, directly behind a LED work light tripod for surface illumination as shown in Figure 7(b). Complying with laboratory safety protocol, the camera was required to be installed behind a clean, translucent safety screen.

DIC camera set-up remained consistent for all testing protocols.

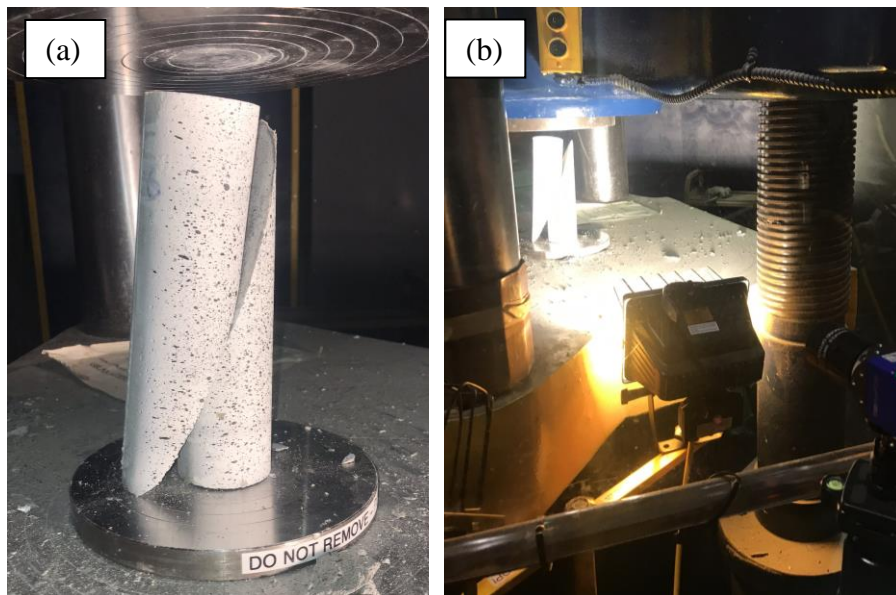


Figure 7: (a) Slant-Shear Specimen with Stochastic Pattern Applied with Speckling; (b) DIC Set-Up

3.4 Testing Program

The testing program consisted of three testing protocols: **monotonic, fatigue, and cyclic**. The monotonic tests were completed first in order to establish a baseline/control failure envelope and provide appropriate limits for fatigue and cycling. Due to campus-wide facility limitations, the fatigue tests were started approximately 1.5 months after completion of the monotonic, with the longer duration cyclic tests started immediately after completion of fatigue tests but spanning a duration of over 2 months.

2D Digital Image Correlation using a high-speed camera was used to investigate strain patterns around the specimen interface prior to failure for all testing protocols. A third party DIC-oriented image acquisition software, *GOM Snap*, was used to capture and store the images at a high frequency during the tests. Exposure settings for image acquisition remained constant for all specimens to ensure comparable strain results.

3.4.1 Monotonic Testing Protocol

The monotonic tests followed the ASTM C882 protocol for testing the bond strength of composite systems by slant shear [18]. Specimens were loaded in a compression-faced Baldwin Machine at a load-controlled rate 0.250 MPa/second until failure. The peak loads were recorded, allowing for evaluation of normal and shear stresses based on specimen orientation. Based on the loading rate of 0.250 MPa/s, specimens were loaded at 66 kN/min and 45 kN/min for the 30° and 25°/20° specimen orientations, respectively. A minimum of three replicates for each orientation and material type were tested monotonically. Monotonic tests were used to generate a baseline for fatigue and cyclic test load limits.

3.4.2 Fatigue & Cyclic Testing Protocol

Design of the fatigue and cyclic testing protocol was primarily adapted from a shear push-off test investigation involving high amplitude and low amplitude cycling of reinforced interfaces by Figueira et al [24]. This literature outlined a “Low Amplitude” protocol cycling between 5% and 60% of the monotonic push-off strength and a “High Amplitude” protocol cycling between 5% and 80% of the monotonic strength. Modifications to the cited protocols were based on, first, the brittle nature of unreinforced slant shear interface examined in the current investigation, and secondly, the limitations of the Baldwin Machine employed for testing such as frequency and load-control. The testing protocols were also developed in conjunction with the discussions and guidelines presented in Section 2.5, namely regarding number of cycles and appropriate loading rates and functions.

The load limits on the fatigue tests were selected as a minimum load of 15% of the peak monotonic slant shear load (failure load) and a maximum of 55% of the monotonic load. Fatigue specimens were loaded to 1000 cycles between these limits using a modified sinusoidal wave function maintained in uniaxial compression at a frequency of 0.5 Hz (1 cycle per 2 seconds) in the Baldwin Machine under load control. The frequency of these tests is adapted from previous fatigue investigations in the literature but was limited by the static nature of the Baldwin machine as well the load-controlled nature of the data acquisition. Fatigue discussions include total cycle numbers ranging from 1000 up to several million, with the latter typically implementing dynamic based testing equipment. The load limits on the cyclic tests were selected as a minimum of 10% and a maximum load of 75% of the peak monotonic slant shear load. These tests involved a standard ramping function between the load limits, at a rate adopted from ASTM C882 of 0.25 MPa/second, consistent with the monotonic loading rate. The cyclic tests involved loading of the

specimens up to 100 cycles also under load control in uniaxial compression with the Baldwin Machine. In the literature, 100 or less number of cycles is described as low cycle, high amplitude conditions which are representative of storm and seismic loading. The exception is that the protocol in the current investigation is under uniaxial compression while true seismic loading requires load reversal between compression and tension.

Both the fatigue and cyclic tests were preceded by brief preliminary cyclic tests between 2 kN and 10% of the peak monotonic for 10 cycles. Upon completion, the fatigue and cyclic tests were followed by monotonic testing to failure, using the procedure adapted from ASTM C822 as discussed above. A summary of the three loading protocols applied in this investigation is presented in Table 3. Figure 8 presents a cropped plot of the applied load and time for a sample fatigue and sample cyclic test. Because the duration of the cyclic tests is directly dependent on the applied load range through the applied loading rate, cyclic tests were significantly longer than fatigue tests, especially for high-strength monotonic specimens (i.e. sandblasted).

Table 3: Summary of Slant Shear Testing Protocol

| | Load Rate | Minimum [% Monotonic] | Maximum [% Monotonic] | Number of Cycles n | Load Function |
|------------------|-------------|--------------------------|--------------------------|-------------------------|-----------------|
| Monotonic | 0.250 MPa/s | - | - | - | - |
| Fatigue | 0.5 Hz | 15% | 55% | 1000 | Sinusoidal Wave |
| Cyclic | 0.250 MPa/s | 10% | 75% | 100 | Ramping |

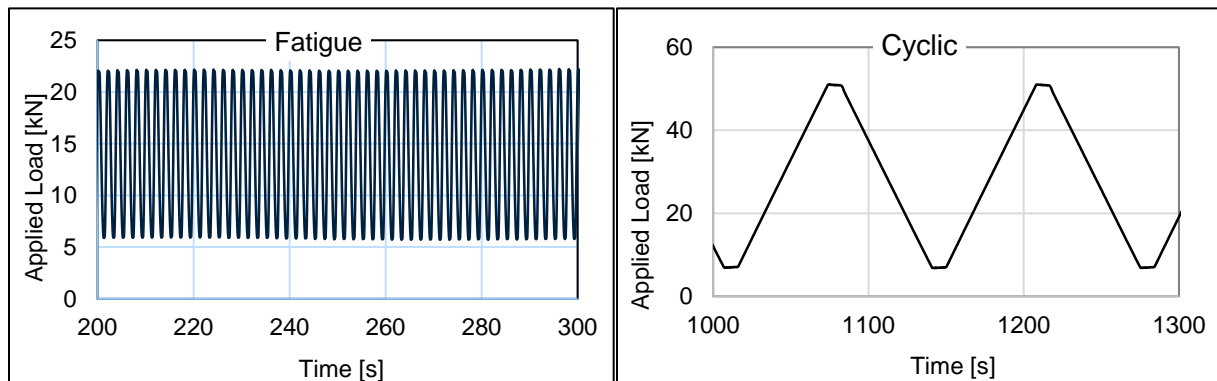


Figure 8: Cropped Sample Plots for Fatigue and Cyclic Tests

3.5 Naming Convention

The specimens are primarily categorized based on the surface preparation method, repair material, and slant inclination. Testing protocol may also be used to describe some of the specimens and resulting figures. As such the figures presented in the following section will refer to the naming conventions prescribed herein, indicated in Figure 9:

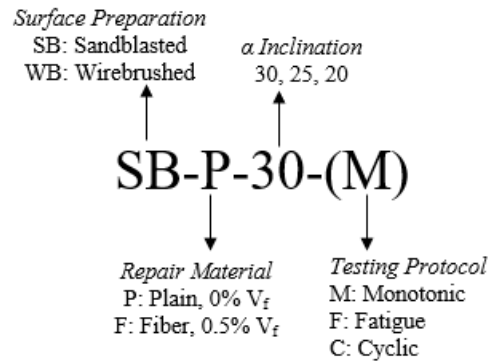


Figure 9: Slant Shear Specimen Naming Convention

A total of 144 slant shear specimens was prepared for the presented investigation, comprising of four material and surface preparation types (SB-P, SB-F, WB-P, WB-F) encompassing three slant shear inclinations (30°, 25°, 20°) and allocated to three types of loading protocols (M, F, C). A minimum of three replicates were typically tested for each specimen type, with the exception of those that were subject to premature failure during cyclic/fatigue testing.

Chapter 4: Results & Discussion

4.1 Quantification of Interfacial Roughness

The surface profile of all specimens was acquired using two-dimensional laser profilometry. After the profile was suppressed from any inclination caused by human or set-up error, it was quantified using the Fib Model Code 2010 average roughness value (R_a) as well as the ASTM Mean Profile Depth method to compare with specimens previously quantified via the Sand Patch Test. A representative surface profile of a wirebrushed specimen (smooth) and sandblasted specimen (rough) including the evaluated roughness values is presented in Figure 10.

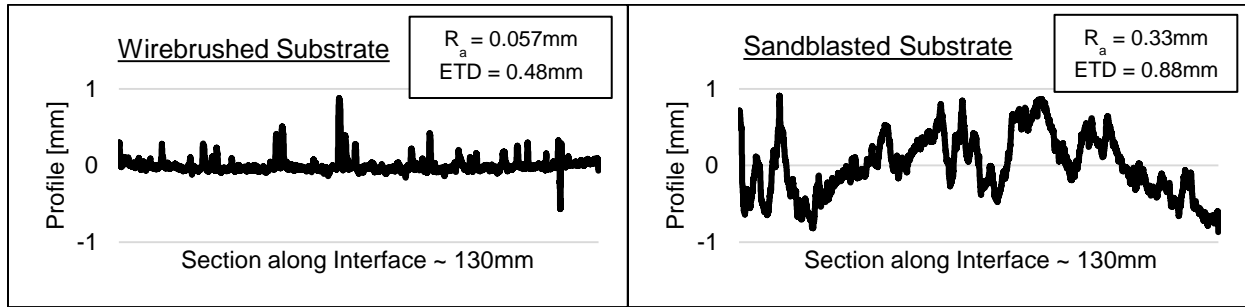


Figure 10: Quantified Substrate Surface Profiles

The average, maximum, and minimum values as well as the standard deviation are presented for both types of surface preparation in Table 4. These values are based on the roughness quantification of all 144 specimens. The average R_a for sandblasted and wirebrushed specimens is 0.50 and 0.074, respectively, while the average ETD for sandblasted and wirebrushed is 0.36 and 1.20, respectively. The difference between rough and smooth specimens is emphasized to a greater extent by the R_a quantification. The normalized shear strength is plotted against the roughness value for monotonically tested specimens in Figure 11(a) for the R_a value and in Figure 11(b) for

the ETD value. Although the scale of roughness varies significantly between both methods, the correlation factor between roughness and bond strength is the same among the two methods.

Table 4: Roughness Quantification of Substrate Specimens

| | Mean Roughness (R_a) | | Estimated Textural Depth (ETD) | |
|---------------------------|--------------------------|-------------|--------------------------------|-------------|
| | Wirebrushed | Sandblasted | Wirebrushed | Sandblasted |
| Average | 0.074 | 0.50 | 0.36 | 1.20 |
| Maximum | 0.17 | 0.85 | 0.54 | 2.80 |
| Minimum | 0.019 | 0.14 | 0.23 | 0.48 |
| Standard Deviation | 0.033 | 0.16 | 0.059 | 0.33 |

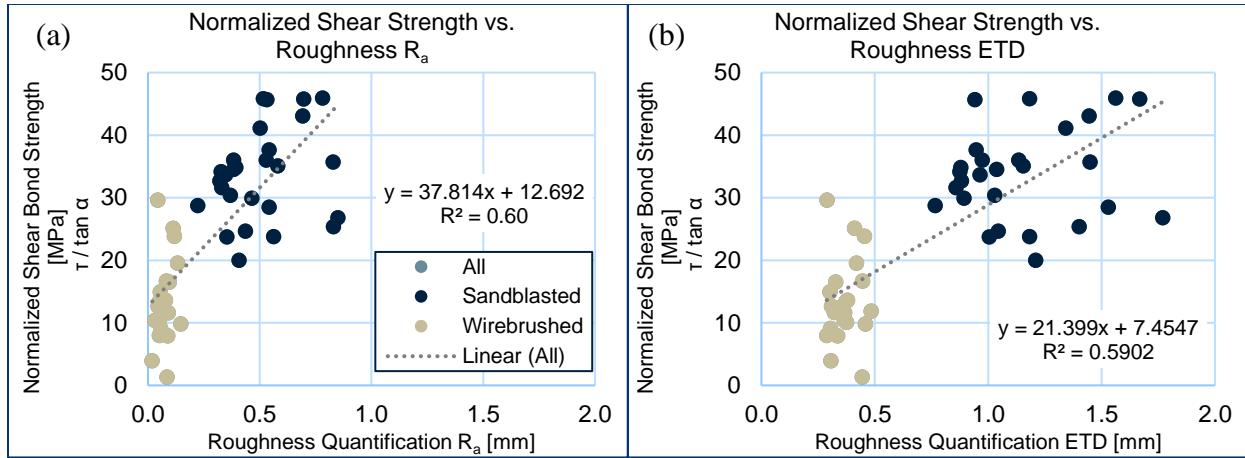


Figure 11: Normalized Shear Bond Strength vs Roughness (Monotonic)

It is important to note that MTD and R_a are not necessarily providing the same information and it may be misleading to compare the two values or use them interchangeably. Where the ETD value presents the maximum deviation between a profile peak and a mean line, the R_a value is focused on the overall deviation between peaks and valleys from a mean line. The literature indicates that both the adhesive bonding mechanism as well as the frictional resistance of an interface are related to the roughness of the substrate [3], [6]. Randl also suggests, that, in addition to the “mean roughness” value, parameters that describe the topography of the surface profile are also necessarily to quantify bond [6]. When we consider the implications of the different

roughness quantifiers on the mechanisms that affect bond strength, we can gain information from both quantification systems. ETD can be interpreted as a general quantification of profile “tortuosity” and roughness in a macro-context. Through this method the following insights can be gained:

- Tortuosity of the sandblasted profile can engage effects of some fibers along the interface, i.e. rigid steel fibers, as demonstrated in [4]
- Frictional resistance in the context of a sawtooth model (fracturing, crushing, dilation), superior in the sandblasted substrate, can be descriptive of interlocking and overriding effects due to the identified asperities of aggregates and surface peaks; some mechanisms require roughness to be activated [9]

Alternatively, the average roughness implied by the R_a value can be descriptive of mechanisms relating to adhesive bond, a result of chemical and physical bonding, which is dependent on the surface contact area of the interface as well as micro-mechanisms, both of which are interrelated to roughness in a micro-scale. Randl suggests that the bond-adhesion mechanism is responsible for bond strength even in low roughness interfaces where macro-frictional resistance is not apparent [6]. The roughness quantification results suggest that the Fib Model Code 2010 R_a value is a more conservative roughness quantifier compared to ETD and the associated MTD, and it is not necessarily descriptive of a sawtooth style interface.

4.2 Experimental Results & Failure Mechanisms

The average 28-day compressive cylinder strength of the substrate concrete was 37 MPa. The average 28-day strength of the plain repair mortar was 59 MPa and for fiber-reinforced repair the average 28-day strength was 63 MPa. A table of the experimentally determined failure loads and failure modes for all slant shear specimens as well as the evaluated applied, normal, and shear stresses are presented in Appendices A.1, A.2, and A.3 for monotonic, fatigue, and cyclic protocols, respectively. Regarding failure modes, the wirebrushed (smooth) specimens all exhibited a failure along the interface. However, a portion of the sandblasted specimens resulted in material failure, predominantly in the form of substrate material compression. In this scenario the failure load provides a lower bound estimate of bond strength and is not fully representative of the interfacial strength [5]. In the case of interfacial bond failure for all three protocols, fibers were not visible on the substrate portion of the failed specimen suggesting that fibers in the repair mortar did not cross the interface into the substrate, as was indicated by Zanotti et al in [9].

Based on the DIC image sequences acquired during testing, a third-party DIC software, *GOM Correlate*, was used to qualitatively assess the technical strain distribution on the surface of the slant shear specimens near the interface. The presented DIC investigation involves observations of strain distributions around the interface prior to specimen failure in order to identify trends among different types of specimens pertaining to the dominant bond mechanisms. A fixed number of DIC images prior to specimen failure were examined at fixed strain limits. A representative replicate was selected for each material, testing protocol, and interfacial inclination. Selections were based on failure mode (interfacial), and failure load – load anomalies were not selected for examination. Furthermore, only replicates whose failure was caught by the Digital Image Correlation Setup were examined.

4.2.1 Monotonic Testing Protocol

4.2.1.1 Shear Bond Strength

The monotonic shear bond strength is presented in Figure 12.

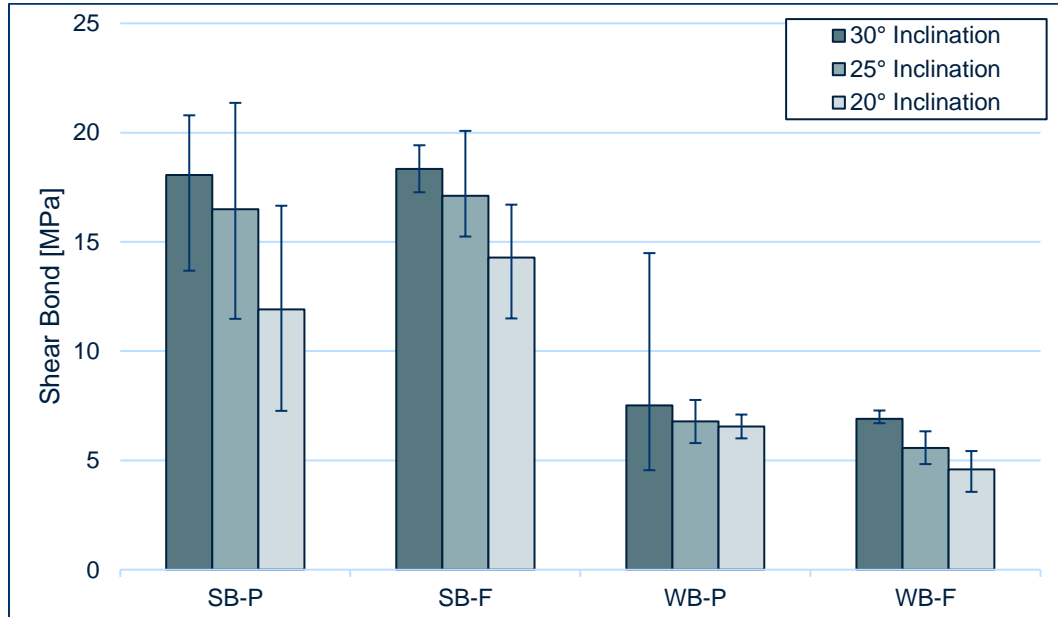


Figure 12: Monotonic Shear Bond Strength

Amongst all the material types (material including surface preparation method) a higher bond strength is exhibited by specimens with a higher normal-shear stress ratio and thereby the largest amount of interfacial friction. Similar results were presented in [4] and [9] where the bond strength is highest with an orientation of 30°, followed by 25°, then 20°. It is clear that sandblasted specimens are of a significantly higher strength than wirebrushed specimens, attributed to a rougher interface yielding both a higher adhesive bond in addition to high friction and aggregate interlock [6]. The use of steel fibers slightly increased the bond strength in sandblasted specimens. The strength increase is more noticeable in specimens with lower frictional component, where the cohesion component has a larger impact – consistent with [4]. However, there is no significant increase in bond strength in wirebrushed specimens reinforced with steel fibers. Rigid steel fibers

potentially require more tortuosity to engage fiber-induced benefits and may actually disrupt porosity at the interface thereby reducing adhesive and cohesive bond [4], [9]. Finally, the wirebrushed plain specimens exhibited the least clearly defined trends as the most brittle and challenging interface. Overall, smooth specimens have little frictional resistance at the interface to counteract shear slip when adhesion is lost and are sensitive to micro-cracks and defects as indicated in [9].

4.2.1.2 Digital Image Correlation

The main forms of strain distribution around the interface of monotonically loaded specimens as identified by Digital Image Correlation are presented in Figure 13.

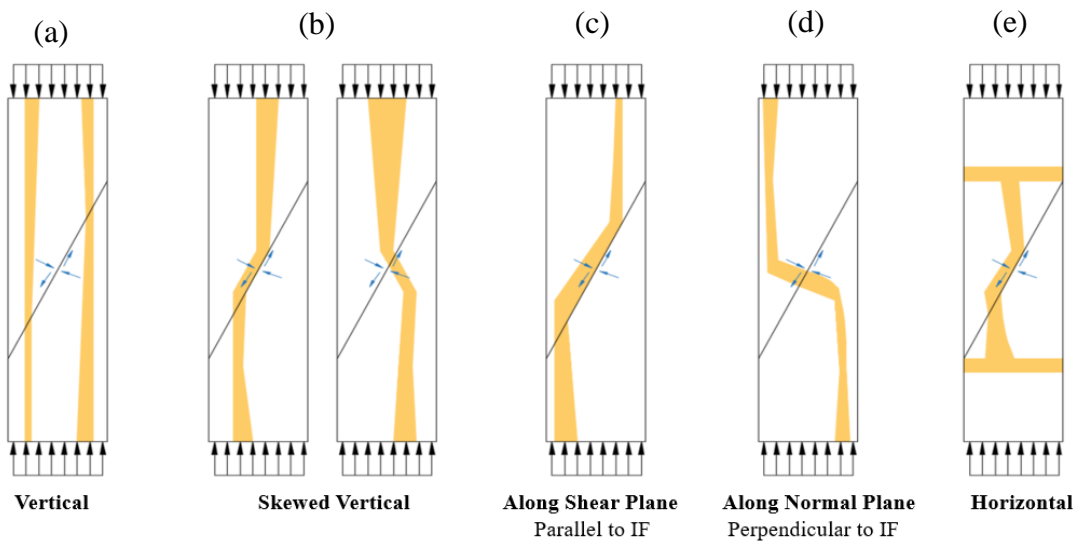


Figure 13: Common Strain Distributions Identified by DIC in Monotonically Loaded Specimens

In sandblasted specimens, concentrations of strain perpendicular to the interface, in the form of Figure 13d, developed during-loading and remained fixed in all images until failure. Prior to failure this distribution contained the highest magnitude of strain. Detailed DIC images of sandblasted specimens are included in Appendix B.1 and Appendix B.2 for plain and fiber

reinforced repairs, respectively. Appearances of strain concentration along the interface, in the form of Figure 13c, were less frequently occurring in sandblasted specimens. Similar patterns of strain distribution were exhibited by sandblasted specimens with a fiber-reinforced repair. These specimens demonstrated noticeably less occurrences of strain along the interface than their plain repaired counterparts. Alternatively, in wirebrushed specimens a fixed concentration of strain perpendicular to the interface, as exhibited by sandblasted specimens, was not demonstrated. Although this strain mode was captured by DIC intermittently, the dominant strain concentrations took the form of distributions along the interface such as those shown in Figure 13c. These concentrations along or parallel to the interface were the most commonly occurring. A comparison of strain distributions prior to failure in a wirebrushed and sandblasted specimen is presented in Figure 14. For wirebrushed specimens with fiber repairs, the occurrences of strain distribution along the interface were shown to decrease slightly while the occurrences of strain distribution perpendicular to the interface increased slightly. Detailed DIC images of wirebrushed specimens are included in Appendix B.3 and Appendix B.4. Appendix B.5 contains details of strain distribution occurrences prior to failure amongst the four material types.

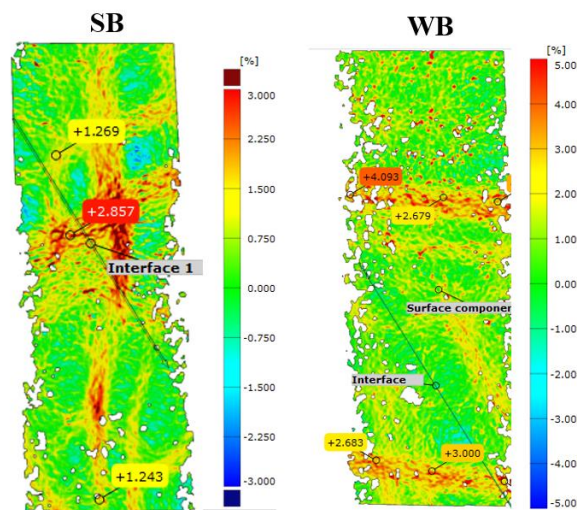


Figure 14: Comparison of Strain Distributions prior to Failure, [Sandblasted (left) and Wirebrushed (right)]

Strain distributions perpendicular to the interfacial plane (Figure 13d), dominant in sandblasted specimens, are believed to be representative of a type of adhesive bonding mechanism. As such, occurrences of this distribution are not proportional to the ratio of applied normal stress, since bond adhesive depends on soundness, cleanliness, and roughness of the substrate [3]. More specifically, the bond-adhesive mechanism is highly dependent on surface roughness which increases surface contact and additionally activates physical micro-mechanisms (crushing, fracturing, interlock) [4], [6]. Espeche & Leon suggest that, when interfacial degradation occurs at high loads, bond-cohesion is damaged and shear cracking occurs surrounding “a series of struts that transmit diagonal compression” [3]. These perpendicular distributions may also be indicative of said struts. The adhesive mechanism is not as evident in wirebrushed as in sandblasted specimens, attributed to a smoother interface with reduced surface contact area and lack of micro-mechanical bonding attributes.

In contrast, it is believed that localized loss of adhesion resulting in localized shear slip is demonstrated by strain distributions along the interface (Figure 13c), which are less frequent in sandblasted specimens and much more significant in wirebrushed specimens. A more prominent loss of adhesion at the wirebrushed interface may result in greater localized shear slip because the interface is not conducive of aggregate interlock [6]. Development of localized slip may engage localized frictional resistance along the interface, which is proportional to the applied normal stress and highest in specimens of 30° inclination. This feature is generally complemented by the observation of increasing occurrences of this strain mode as the proportion of normal stress increases, exclusive to wirebrushed specimens.

DIC observations suggest that the use of fibers increase the frequency of “bond-adhesive” strain modes in both sandblasted and wirebrushed specimens. However, this is only reflected by

the bond strength increase of sandblasted fiber-repair specimens, particularly the orientations with a lower proportion of frictional resistance.

4.2.2 Fatigue Testing Protocol

4.2.2.1 Shear Bond Strength

The shear bond strength of specimens subjected to a fatigue loading protocol is presented in Figure 15, with monotonic bond strength included for comparison. In examining the fatigue bond strength results exclusively, the strength difference between fiber repaired and plain specimens is most evident for sandblasted interfaces. Like monotonic specimens, wirebrushed interfaces have less significant bond strength advantages through the use of steel fibers.

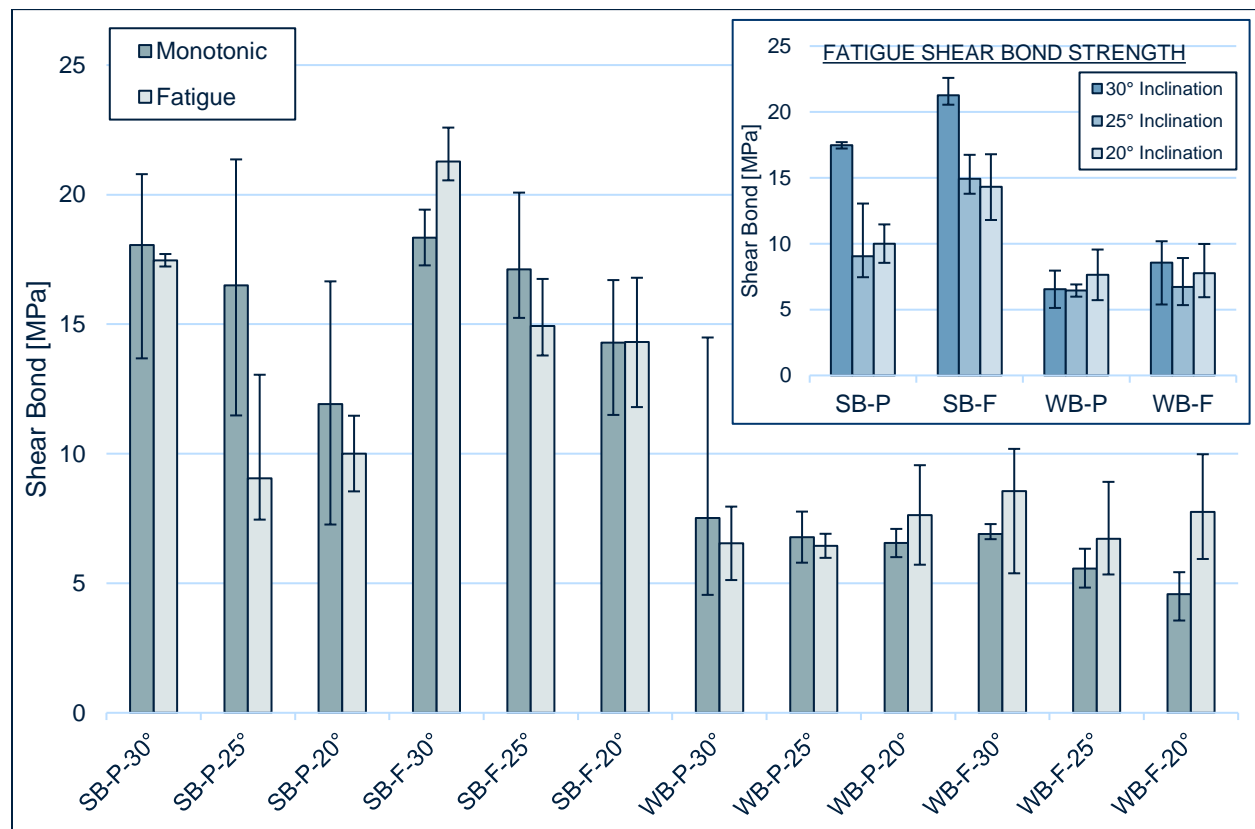


Figure 15: Shear Bond Strength of Fatigue-Loaded and Monotonic Specimens

The bond stresses resulting from monotonic and fatigue protocol are presented for the four material types in Figure 16:

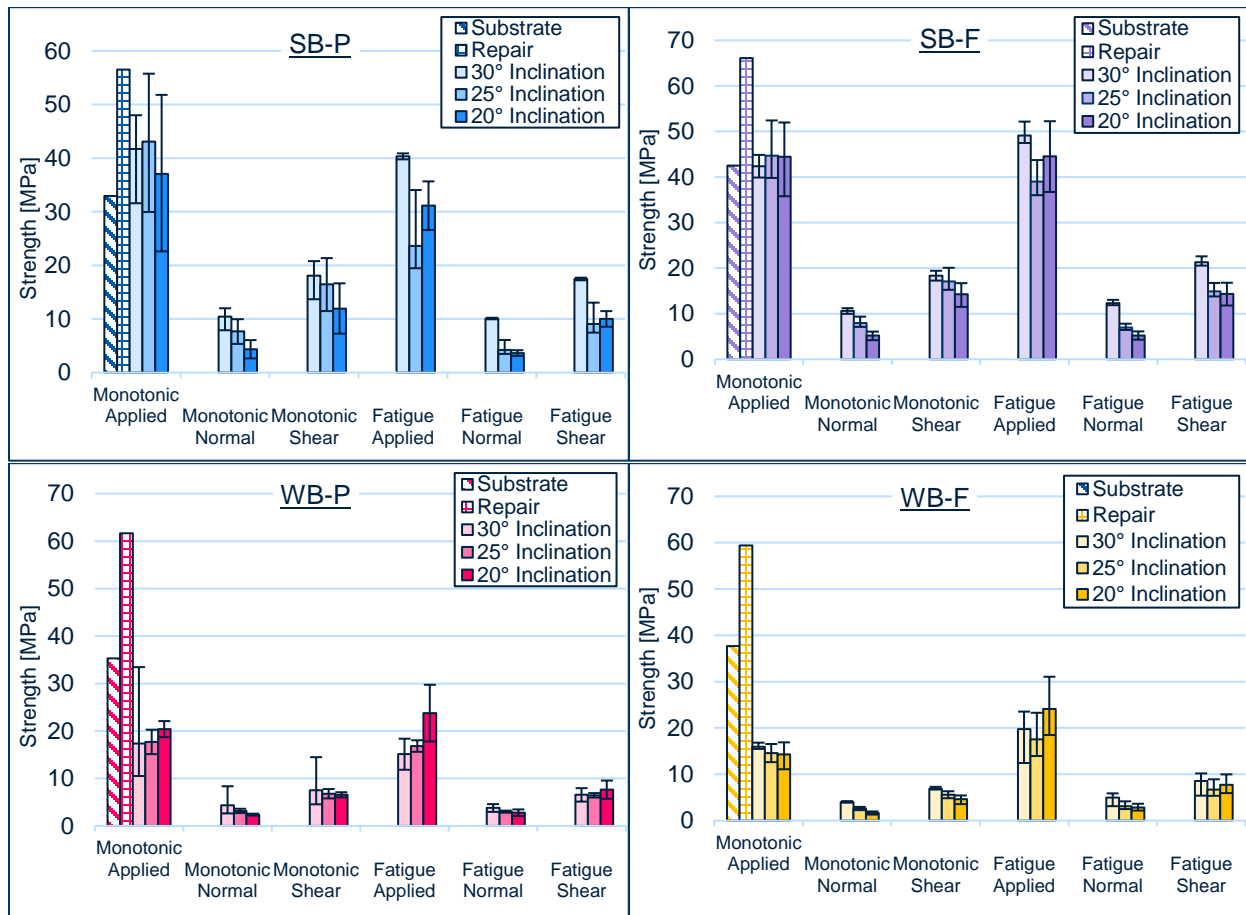


Figure 16: Applied, Normal, and Shear Stresses under Monotonic and Fatigue Loading

A notable strength decrease is evident in sandblasted specimens with plain repairs subject to fatigue loading. The most significant strength decrease is indicated by specimens with a lower friction component (i.e. slant inclinations of 25° and 20°). However, bond strength is significantly retained in sandblasted-fiber repair specimens. It is important to note that, likewise in SB-P, the highest magnitude of strength decrease in SB-F is demonstrated by specimens with a lower frictional component. A slight strength decrease is demonstrated by wirebrushed specimens with plain repairs. Generally, the trends relating to specimen inclination and proportion of applied

normal stress are not as apparent in WB-P specimens, attributed to the sensitivity of the interface type. Wirebrushed specimens with fiber repairs exhibit no change in shear strength under fatigue loading. The benefit of steel fibers in retaining bond strength is further evidenced by these specimens. Slight bond strength increases of fatigue loaded specimens are indicated in Figure 15, these are attributed to the increase in load rate of fatigue specimens (0.5 Hz).

The experimental results suggest that high roughness interfaces undergo more significant bond strength degradation compared to smooth interfaces, when subjected to fatigue loading. Similar observations regarding concrete-to-concrete friction under cyclic loading were presented in [22]. However, bond strength degradation in the current investigation is attributed primarily to a deterioration of the adhesive bonding mechanism rather than a “frictional” degradation of the surface profile under fatigue (evidenced by strength decrease in low friction specimen orientations). This degradation may be associated with material damage and microcracking near the bond plane as well as damage to physical micro-mechanisms through repeated loading. The minor strength decrease of the wirebrushed (smooth) interface suggests that although strength degradation may not be related purely to frictional capacity, it is indeed associated with interfacial roughness, a parameter that significantly affects adhesion through surface contact area and localized interlock, crushing, and fracturing. Furthermore, the results suggest that steel fibers reduce the magnitude of bond strength reduction at the interface when subjected to fatigue loading, demonstrated in both sandblasted specimens and wirebrushed specimens. Beneficial effects of fibers are discussed in [21] as extending fatigue life of concrete structures.

4.2.2.2 Digital Image Correlation

Strain analysis of fatigue-loaded specimens with DIC overall presents a more scattered, disjointed, and ambiguous selection of strain distributions compared to monotonic analysis. Strain

concentrations as presented in Figure 13 can be identified to a certain extent but with less clear confinement. A comparison of a DIC image prior to failure in a monotonic specimen and a fatigue specimen is presented in Figure 17. These observations are attributed to the material damage and microcracking induced during fatigue loading. DIC analysis of sandblasted-plain specimens demonstrates an obvious change in the previously identified “adhesive” strain mode. Concentrations are not consistently present in DIC frames prior to failure. Similarly, these specimens exhibit an increase in strain distributions associated with loss of adhesion. These trends are also demonstrated in sandblasted specimens with fiber repairs, although the “adhesive” strain concentration is more evident in SB-F than SB-P. In wirebrushed specimens, both with plain repairs and fiber repairs, there is also a decrease of strains perpendicular to the interface. In all materials types a mix or overlapping of strain concentrations is apparent, suggesting multiple or different failure mechanisms active at the interface. Detailed DIC images are presented in Appendix C.1 for sandblasted plain, Appendix C.2 for sandblasted fiber, Appendix C.3 for wirebrushed plain, and Appendix C.4 for wirebrushed fiber.

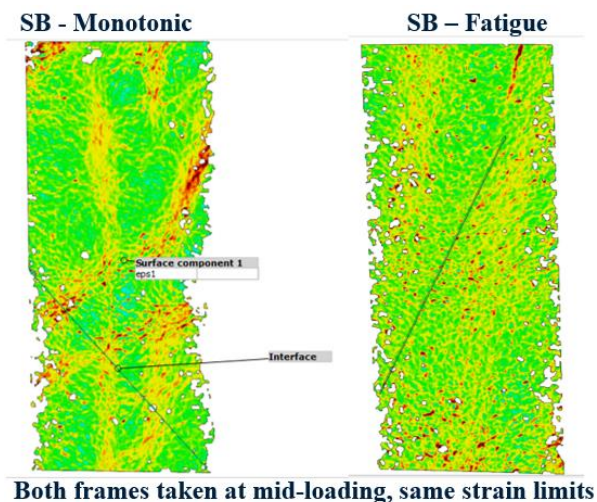


Figure 17: Strain Analysis in Monotonic Specimen and Fatigue-Loaded Specimen

A reduction of concentrations perpendicular to the interface, particularly pronounced in sandblasted specimens, may suggest a degradation of previously identified adhesive bonding mechanism. The overall increase in concentrations along interface may reflect increase in localized sliding/shear slip due to loss of adhesion. This is reflected by a notable decrease in bond strength of fatigue-loaded sandblasted specimens. The degradation of adhesive bonding mechanisms may be demonstrated to a lesser extent with the use of steel fibers. This observation is again most pronounced in sandblasted specimens but is reflected by both the diminished bond strength decrease in SB-F specimens and the lack of evident strength change in fatigued loaded WB-F. Material damage and micro-cracking induced by the loading protocol is reflected in the increased ambiguity and overlapping of strain concentrations. Appendix C.5 contains details of strain distribution occurrences prior to failure for specimens subjected to a fatigue loading protocol.

4.2.3 Cyclic Testing Protocol

4.2.3.1 Shear Bond Strength

The shear bond strength of specimens subjected to a cyclic loading protocol is presented in Figure 18, with monotonic bond strength included for comparison. The results are variable and generally inconclusive. Compared to monotonic and fatigue-loaded specimens, there is a notable increase in bond strength in the examined cyclic specimens, especially in fiber-reinforced repairs. A late stage bond strength-gain potentially occurred in the cyclic specimens due to the delayed schedule. Further investigation is recommended to examine bond behavior under cyclic loading, specifically under a high amplitude and low cycle testing protocol, as outlined in the experimental program. It is recommended to examine whether interfacial profile degradation would occur in the form of frictional degradation as discussed in [22] (interfacial “smoothing” of rough interfaces) or, rather, in the form of adhesive degradation as demonstrated by fatigue loaded specimens.

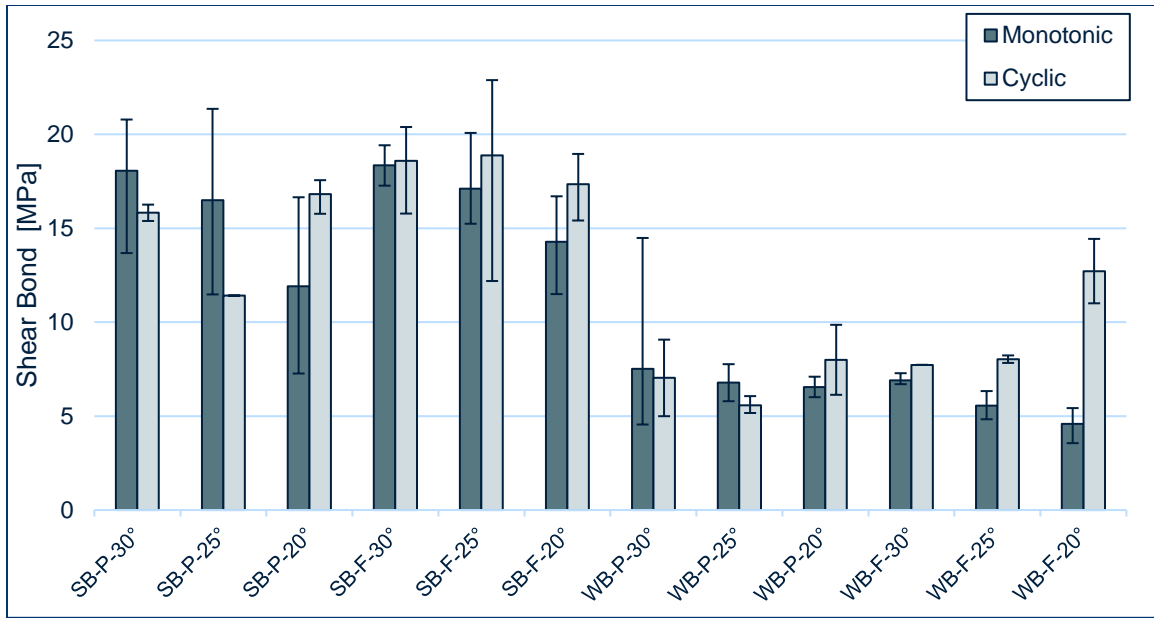


Figure 18: Shear Bond Strength of Cyclic-Loaded and Monotonic Specimens

4.2.3.2 Digital Image Correlation

DIC investigation of specimens loaded under a cyclic protocol identifies strain concentrations that are more scattered and disjointed than monotonic specimens, similar to fatigue specimens. Regarding strain concentration amongst material types the following has been observed:

- **SB-P:** Strain distributions are not clearly defined, and a mix of strain modes is evident.
- **SB-F:** Distributions are more consistent with observations of fatigue specimens – fewer perpendicular distributions along interface (representing adhesive bond) after cyclic loading.
- **WB-P:** An increase in mixed and overlapping strain distributions is apparent.
- **WB-F:** Strain distributions are unique with notable occurrences of concentrations perpendicular to the interface (representing an adhesive bonding mechanism).

4.3 Failure Envelopes & Modelling

From the peak applied loads at failure obtained through experimental slant shear testing, the applied stresses are obtained. Interfacial shear and normal stresses are subsequently evaluated using equations (1) and (2).

$$\tau_n = \frac{1}{2} \sigma_0 \sin (2\alpha) \quad (1)$$

$$\sigma_n = \sigma_0 \sin^2 \alpha \quad (2)$$

σ_0 is the applied axial stress that produced failure along the bond plane

σ_n is the normal stress acting perpendicular to the bond plane

τ_n is the shear stress acting parallel to the bond plane

α is the inclination angle of the bond plane with the vertical axis

The experimental shear-normal stress data is plotted, and line fitting of predictive models is used to produce a failure envelope. Linear regression is used to determine the respective Linear-Mohr Coulomb failure envelope for each of the four material types, in the form of equation (3). Nonlinear regression is used to determine the respective Carol Plasticity failure envelope in the form of equation (4a) for roughened interfaces (SB-P, SB-F) and equation (4b) for wirebrushed, near-smooth interfaces (WB-P, WB-F). The Carol equations presented below have incorporated a tensile-cohesion relation adopted from [4] and [11] in place of experimentally derived tensile bond strengths. More specifically, excel solver is adopted to determine the optimized parameters of c and ϕ through the minimization of the sum of the square residual. The following equations are presented in a form assuming compression as positive:

$$\tau_n = c + \mu \sigma_n = c + \tan \phi \cdot \sigma_n \quad (3)$$

$$\tau_{n,rough} = \sqrt{(c + \sigma_n \cdot \tan\phi)^2 - \left(c - \frac{c}{2.8} \cdot \tan\phi\right)^2} \quad (4a)$$

$$\tau_{n,smooth} = \sqrt{(c + \sigma_n \cdot \tan\phi)^2 - \left(c - \frac{c}{2} \cdot \tan\phi\right)^2} \quad (4b)$$

τ_n is the evaluated shear stress acting parallel to the bond plane

σ_n is the normal stress acting perpendicular to the bond plane

c is the interfacial cohesion

μ is the frictional coefficient and $\mu = \tan\phi$

ϕ is the internal angle of friction

The interfacial cohesion and internal angle of friction bond parameters can be derived from the presented failure envelopes for each material type under monotonic and fatigue loading. These parameters will be examined herein.

4.3.1 Monotonic Testing Protocol

The plotted monotonic linear Mohr-Coulomb envelopes are presented in Figure 19 and the plotted monotonic Carol Envelopes are presented in Figure 20. The derived bond parameters and coefficient of correlation are presented in Table 5. In sandblasted specimens, the use of steel fibers increases the derived cohesion parameter and slightly decreases the friction angle. This trend is consistent among both envelopes, with the linear portion of the Carol envelope aligned with the linear MC envelope. A similar effect of steel fibers is demonstrated by wirebrushed specimens. It is important to note that large clusters of low strength wirebrushed data result in a high slope value in both the Carol and Linear MC envelopes and consequently a high internal friction angle is derived. Finally, it is evident from the envelope plots that the Carol Plasticity envelope provides a

much more conservative estimation of the extrapolated tensile bond strength, as originally proposed by [3]. Extrapolated tensile bond strength, f_t , is presented in Table 6. Additional monotonic failure envelope plots, presented for each material type, are included in Appendix D.

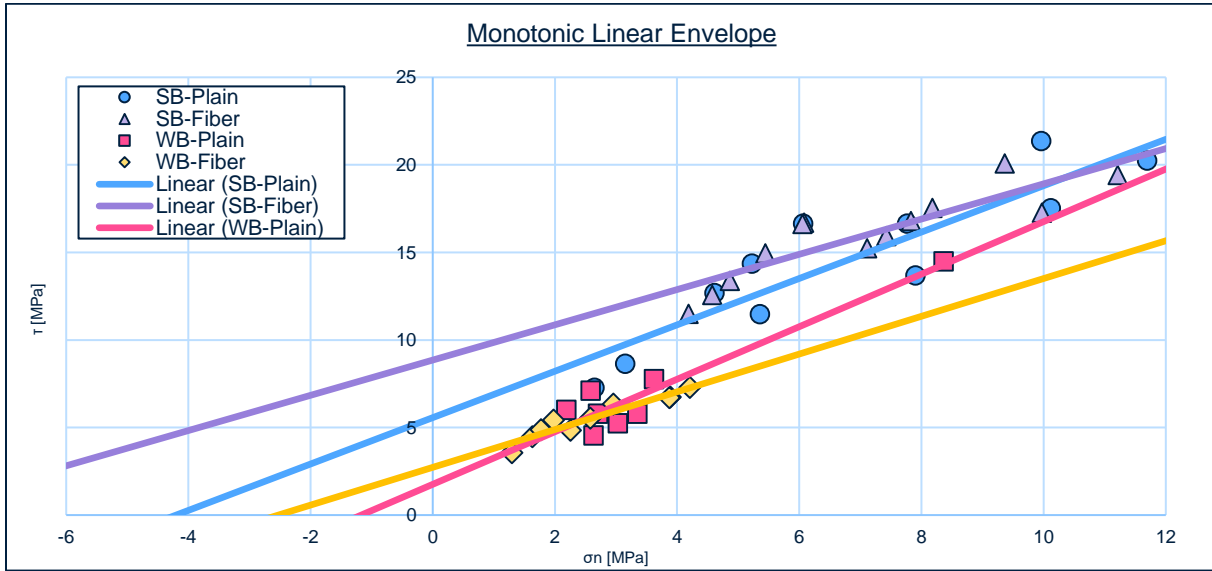


Figure 19: Linear Mohr-Coulomb Envelope for Monotonic Specimens

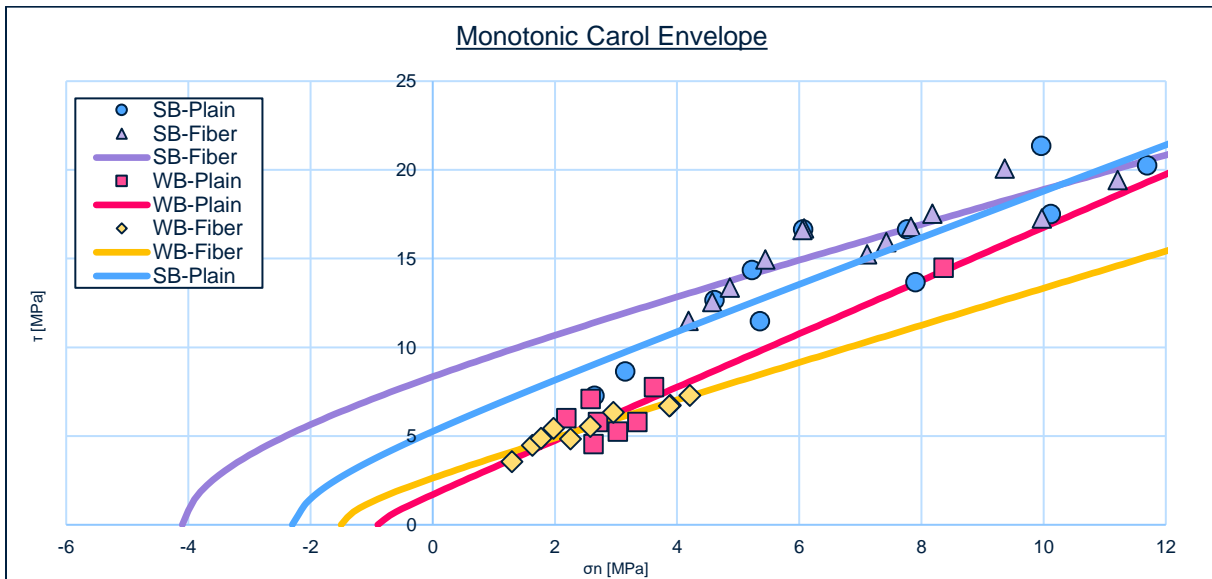


Figure 20: Carol Plasticity Envelope for Monotonic Specimens

Table 5: Derived Bond Parameters for Monotonic Specimens

| Monotonic Linear | | | | Monotonic Carol | | |
|-------------------------|----------------|--------------------------------|-------------------------|------------------------|--------------------------------|-------------------------|
| | c [MPa] | ϕ (deg) | R^2 | c [MPa] | ϕ (deg) | R^2 |
| SB-P | 5.57 | 53.0 | 0.8469 | 6.26 | 52.1 | 0.85 |
| SB-F | 8.85 | 45.2 | 0.77 | 11.33 | 42.2 | 0.78 |
| WB-P | 1.76 | 56.3 | 0.90 | 1.78 | 56.3 | 0.90 |
| WB-F | 2.73 | 49.5 | 0.92 | 3.05 | 46.0 | 0.99 |

Table 6: Extrapolated Tensile Bond Strength

| | Linear | Carol |
|-------------|-------------------------------|-------------------------------|
| | f_t [MPa] | f_t [MPa] |
| SB-P | 4.20 | 2.23 |
| SB-F | 8.80 | 4.05 |
| WB-P | 1.17 | 0.89 |
| WB-F | 2.53 | 1.52 |

Trends in derived parameters are consistent among both envelopes, although cohesion is slightly overestimated by the Carol envelope, particularly in sandblasted specimens with a fiber repair. The derived friction angle is lower in the Carol envelope than in the linear envelope. These slight differences are consistent with the discussion on predictive models presented in [4]. The cohesion value in sandblasted specimens is significantly higher than wirebrushed specimens. A visual representation of cohesion values is presented in Figure 21. Similar results were demonstrated by Zanotti et al in [9]. This is attributed to a greater bond-adhesive mechanism generated by increased surface contact area and micro-mechanical bonding capacity, both of which are contingent on interfacial roughness [4], [6]. The addition of steel fibers increases cohesion in both sandblasted and wirebrushed specimens, with a larger increase demonstrated by the Carol envelope. It also causes a decrease in the friction angle which was discussed in [4] and [9] as a

steel-fiber induced result of the deviation of the fracture plane beyond the bond plane causing a decrease in roughness.

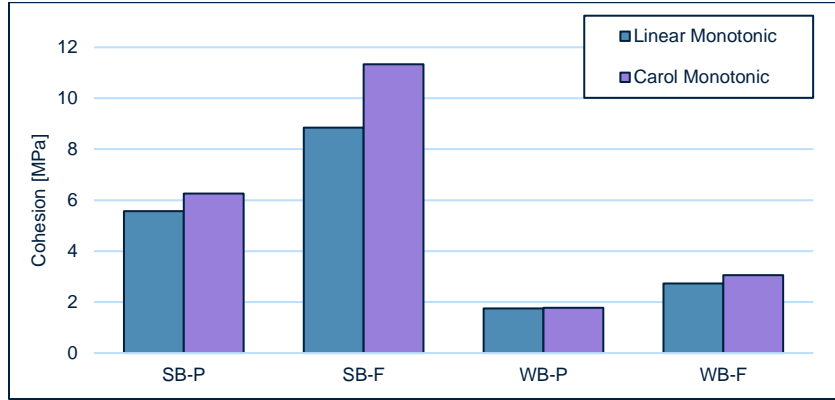


Figure 21: Cohesion Parameter for Monotonic Specimens

4.3.2 Fatigue Testing Protocol

Plots of fatigue failure envelopes have been represented with the control monotonic envelopes. Figures 22, 23, 24, and 25 present the Linear MC and Carol Plasticity envelopes for Sandblasted-Plain, Sandblasted-Fiber, Wirebrushed-Plain, and Wirebrushed-Fiber specimens, respectively. For both monotonic and fatigue envelopes, the derived bond parameters and coefficient of correlation are included in Table 7.

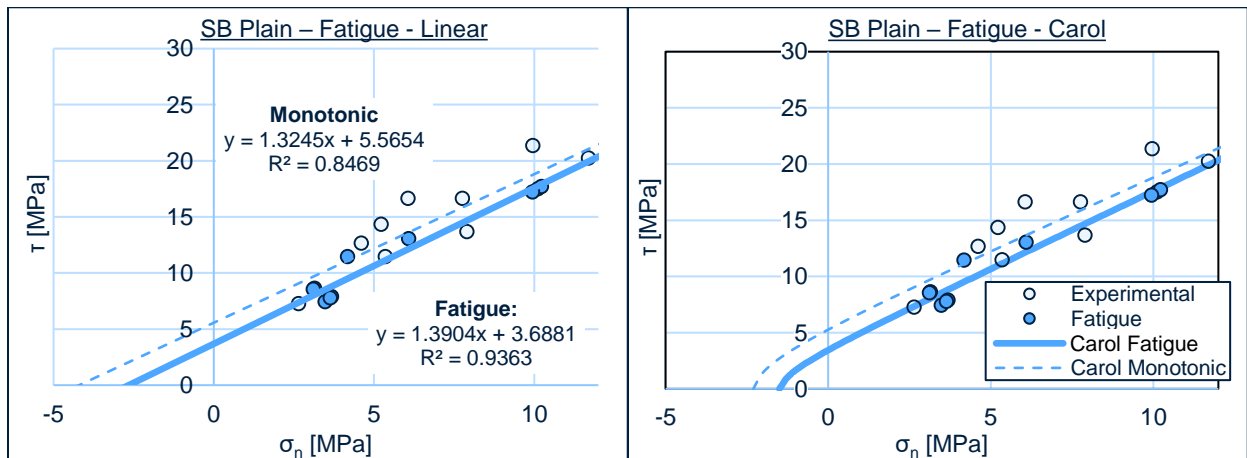


Figure 22: Fatigue Envelopes for SB-P

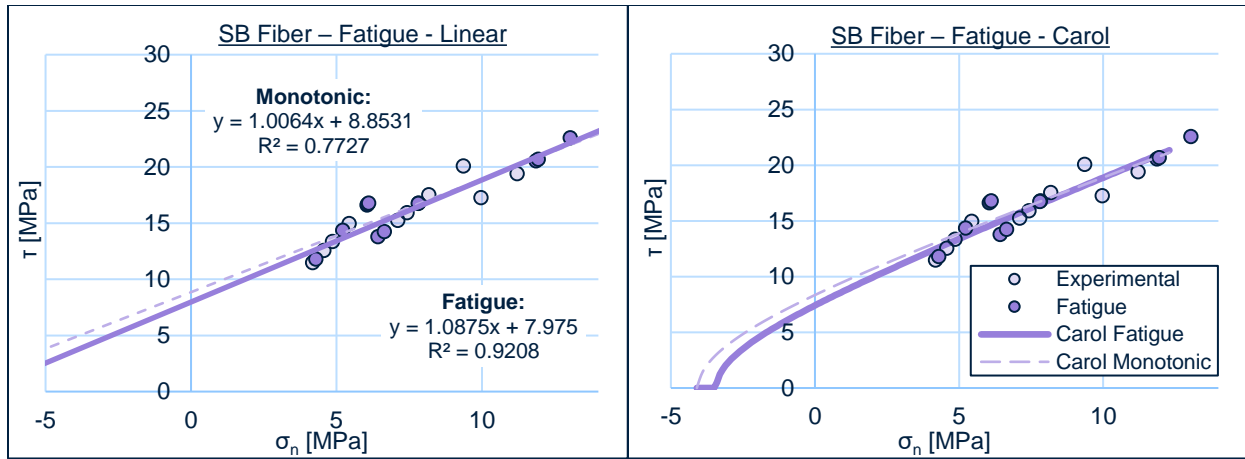


Figure 23: Fatigue Envelopes for SB-F

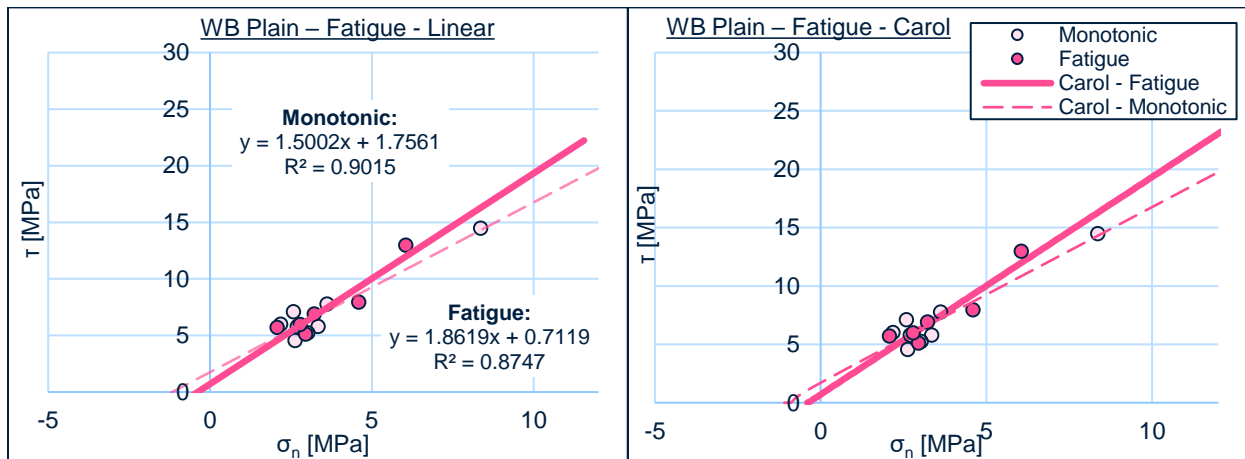


Figure 24: Fatigue Envelopes for WB-P

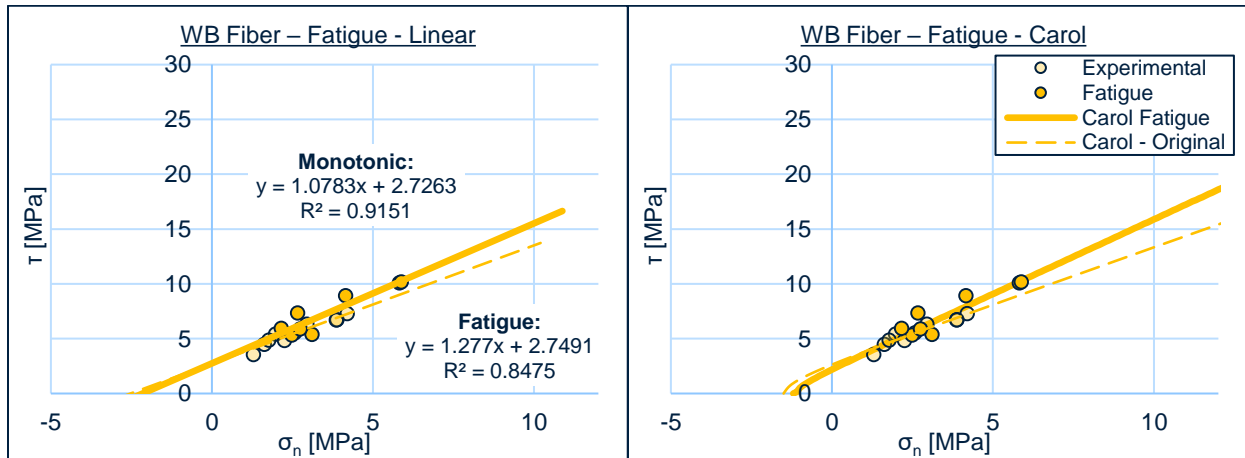


Figure 25: Fatigue Envelopes for WB-F

Table 7: Derived Bond Parameters for Fatigue-Loaded Specimens

| | Monotonic Linear | | | Fatigue Linear | | | Monotonic Carol | | | Fatigue Carol | | |
|-------------|------------------|--------------|-------|----------------|--------------|-------|-----------------|--------------|-------|---------------|--------------|-------|
| | c | ϕ (deg) | R^2 | c | ϕ (deg) | R^2 | c | ϕ (deg) | R^2 | c | ϕ (deg) | R^2 |
| SB-P | 5.57 | 53.0 | 0.85 | 3.69 | 54.3 | 0.94 | 6.26 | 52.1 | 0.85 | 4.00 | 53.9 | 0.94 |
| SB-F | 8.85 | 45.2 | 0.77 | 7.97 | 47.4 | 0.92 | 11.33 | 42.2 | 0.78 | 9.58 | 45.7 | 0.92 |
| WB-P | 1.76 | 56.3 | 0.90 | 0.71 | 61.8 | 0.87 | 1.78 | 56.3 | 0.90 | 0.71 | 61.8 | 0.87 |
| WB-F | 2.73 | 49.5 | 0.92 | 2.75 | 51.9 | 0.85 | 3.05 | 46.0 | 0.99 | 2.32 | 53.6 | 0.90 |

In sandblasted-plain specimens fatigue loading is associated with a decrease in the cohesion value and a minor increase in the angle of internal friction. This trend is very consistent among both envelopes. In sandblasted-fiber repair specimens the decrease in cohesion value is less than in plain specimens, although the increase in friction angle is greater. The trend is generally consistent among both envelopes; however, the Carol criterion suggest a slightly higher magnitude of cohesive degradation. In wirebrushed-plain specimens a decrease in cohesion and increase in friction angle is also demonstrated, but the increase in friction angle (slope) is more pronounced in comparison with sandblasted specimens. Both envelopes present near-identical changes in the associated bond parameters. For wirebrushed specimens with fiber repair the decrease in cohesion is less than in the plain repair specimens. The linear envelope interestingly exhibits no change in the cohesion parameter, whereas the Carol envelope exhibits a slight decrease as well as a notable increase in friction angle.

The presented failure envelopes and extrapolated bond parameters suggest that the fatigue loading protocol has the most significant impact on cohesion, rather than the frictional coefficient or friction angle. This observation is consistent with bond strength results, which exhibit a more pronounced strength reduction in specimens with lower frictional resistance. It is also consistent with DIC strain analysis where the most notable pattern was a decrease in strain concentrations

representative of an adhesive bonding mechanism. Therefore, it appears that fatigue loading may cause degradation of the adhesive/cohesive bonding mechanism rather than degradation of the surface asperities and resulting frictional resistance. This degradation can be associated with material damage and microcracking at and around the interfacial plane resulting in damage to physical micro-mechanisms and surface contact area (chemical bond) which are responsible for adhesive bond along the interface. A summary of extrapolated bond parameters is presented by Figure 26(a) and (b).

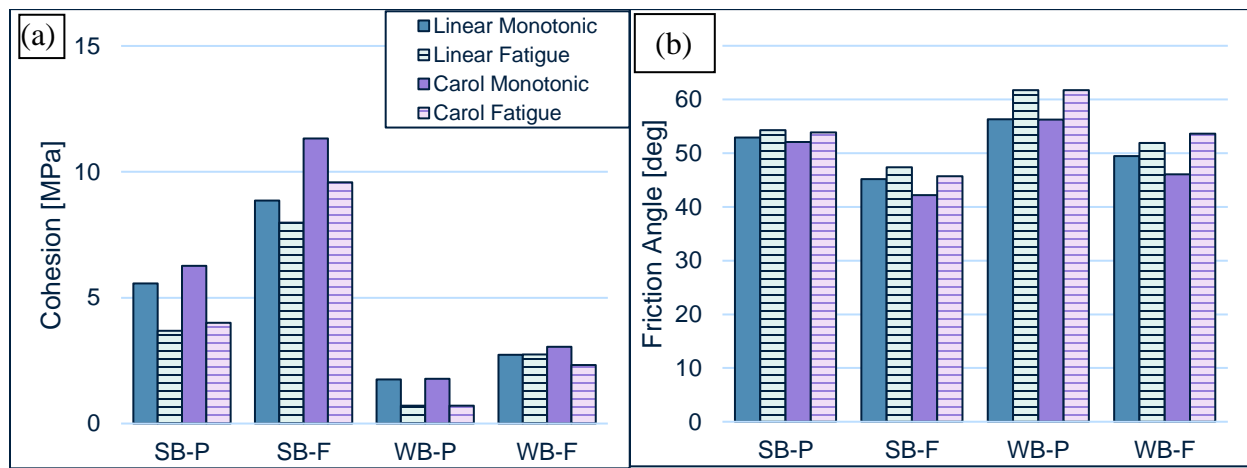


Figure 26: Bond Parameters for Monotonic and Fatigue-Loaded Specimens [(a) Cohesion; (b) Friction Angle]

Cohesive degradation is more significant in sandblasted, roughened specimens than wirebrushed, near-smooth specimens. Furthermore, cohesive degradation is reduced in specimens with fiber-reinforced repairs. This suggests that the magnitude of adhesive bond deterioration is interrelated to interfacial roughness although the physical profile and asperities do not significantly degrade like in [22], which attributes the deterioration of push-off shear stiffness to surface degradation and interfacial smoothing. The use of fibers retains material integrity, and thereby cohesive and adhesive bond strength and is effective in extending fatigue like as indicated in [21]. Specifically, the increased load and energy absorption capacity of the repair material imparted by ductile steel

fibers may be generating increased resistance under rapidly applied repeating fatigue loads [16], [17]. The ability of fiber reinforcement to maintain stress transfer across cracks may be beneficial against the imparted material damage and micro-cracking, especially at the bond interface [4], [9].

In all material types examined, a decrease in the cohesion parameter is typically associated with an increase in friction angle parameter, though the change in friction angle is less significant. As cohesive and adhesive bond mechanisms degrade, the fracture plane may be encouraged to shift back towards the bond plane resulting in increased “identified” roughness. Zanotti et al discuss deviation of fracture plane with use of steel fibers [9] – perhaps, in relation to this research, deviation of fracture plane is encouraged by adhesive bonding mechanisms overall, and engagement of this mechanism increased with use of fibers.

Regarding the examined failure envelopes, the trends of derived parameters are generally consistent with monotonic tests. The exception is the wirebrushed-fiber specimens; however, this anomaly is associated solely with the linear envelope and is attributed to a modelling limitation.

4.4 Limitations of Failure Envelope Models

4.4.1 Limitations

The friction angle for monotonic and fatigue-loaded specimens, extrapolated from two bond envelopes, has been examined and is outlined in Figure 26(b). Table 8 presents the derived friction angles in relation to the average roughness value, R_a , of each material grouping. Based on discussions of the frictional coefficient in relation to substrate roughness in the literature, it is generally accepted that friction angle is related to the roughness of the substrate and increases proportionally with interfacial roughness [3], [4], [7], [11].

Table 8: Average Roughness and Extrapolated Friction Angle

| | R_a | φ (deg) | | | |
|-------------|----------------------|---------------------|-----------------------|--------------------|----------------------|
| | (mm) | Linear Mono. | Linear Fatigue | Carol Mono. | Carol Fatigue |
| SB-P | 0.49 | 53.0 | 54.3 | 52.1 | 53.9 |
| SB-F | 0.51 | 45.2 | 47.4 | 42.2 | 45.7 |
| WB-P | 0.078 | 56.3 | 61.8 | 56.3 | 61.8 |
| WB-F | 0.068 | 49.5 | 51.9 | 46.0 | 53.6 |

The friction angle for a smooth interface has been reported to range from 35° to 39°, while the friction angle for medium rough to rough interface is reported to range from 45° to 54°, according to [3],[11]. Although the sandblasted friction angles are consistent with the values reported in literature, the extrapolated friction angle is severely overestimated for wirebrushed specimens in both envelopes and under both loading protocols [3],[11]. This inconsistency is attributed to the difficulty of modelling the wirebrushed bond stresses, which comprise clusters of low-strength data points, in both of the investigated predictive models. Although the extrapolated cohesion parameters are consistent with previous research, [4], [9], [14], the slope and thereby friction angle is overemphasized for near-smooth wirebrushed-plain and wirebrushed-fiber specimens.

4.4.2 Proposed Solution

In order to resolve the limitation presented in the predictive models for smooth and near smooth slant-shear specimens, a semi-empirical modification to Carol's equation is proposed. A friction angle modification factor was evaluated through the optimized nonlinear regression of existing slant shear data with imposed friction angle "constraints". The maximum allowable friction angle was set to 45°, slightly higher than the value discussed in the literature accounting for the roughness imparted by wirebrushing treatment (specimens are not purely "as-cast" smooth) and also accounting for the trend of friction angle increases after fatigue-loading. A modification

factor of **1.5** was obtained, first derived from the data of wirebrushed-plain repairs under monotonic loading, and subsequently validated with remaining three data sets from the current investigation (WB-F-M, WB-P-F, WB-F-F) and two data sets from a previous investigation at UBC involving “as-cast” interfaces. The resulting semi-empirical modification to Carol’s original equation (3) is proposed for the failure envelope of smooth and near-smooth interfaces, as per equation 6a. Equation 6b incorporates the tensile strength-cohesion relations for smooth interfaces, from [11]. It is important to note that the extrapolated cohesion value remains unchanged using this modification:

$$\tau_{n,smooth} = \sqrt{(c + \sigma_n \cdot \tan(1.5 \cdot \phi))^2 - (c - f_t \cdot \tan(1.5 \cdot \phi))^2}, \phi < 45^\circ \quad (6a)$$

$$\tau_{n,smooth} = \sqrt{(c + \sigma_n \cdot \tan(1.5 \cdot \phi))^2 - \left(c - \frac{c}{2} \cdot \tan(1.5 \cdot \phi)\right)^2}, \phi < 45^\circ \quad (6b)$$

From the equations presented above, a simplified semi-empirical modification can be suggested for the friction angles derived from either the original Carol equation or the Linear Mohr-Coulomb equation for smooth and near-smooth interfaces:

$$\phi_{smooth} = \frac{\phi_{original}}{1.5} \quad (7)$$

ϕ_{smooth} is the modified friction angle for smooth and near smooth interfaces

$\phi_{original}$ is the friction angle derived from the linear MC or original Carol Plasticity equation

4.4.3 Modified Envelopes

Using the proposed equation and resulting “modified” friction angle, an *Experimental Carol Envelope* is plotted for the smooth interface which pertains to the experimental dataset. Through input of the acquired “modified” friction angle into the original Carol equation, a rotated *Modified Carol Envelope* is presented, more representative of stress criterion for smooth and near

smooth interfaces. Updated envelopes for monotonic specimens are presented in Figures 27 and 28, for plain repairs and fiber repairs, respectively. Original friction angles of 56.3° and 46.0° are modified to 37.6° and 30.7° for plain repairs and fiber repairs, respectively, while the cohesion parameters and extrapolated tensile bond strength values remain unchanged. Similarly, updated envelopes for fatigue-loaded specimens are presented in Figure 29 and 30. Original friction angles of 61.8° and 53.6° are modified to 41.2° and 35.8° for plain repairs and fiber repairs, respectively.

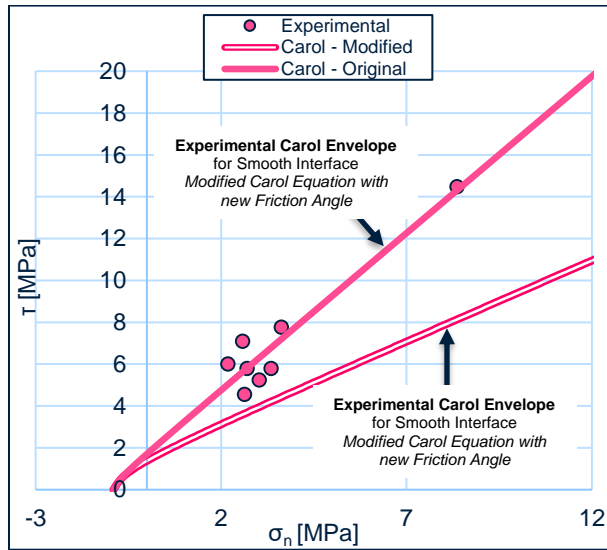


Figure 27: Modified Carol Envelope for WB-P

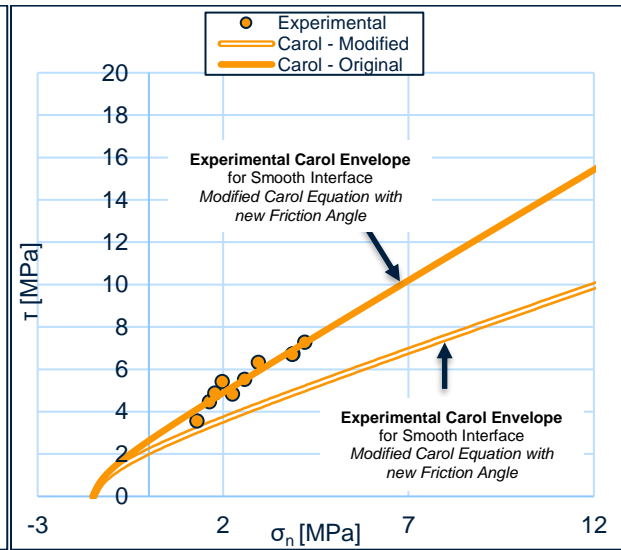


Figure 28: Modified Carol Envelope for WB-P

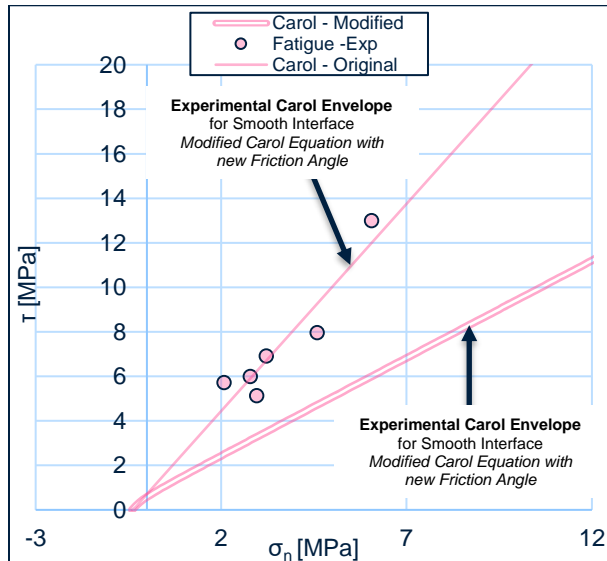


Figure 29: Modified Carol Envelope for WB-P-(F)

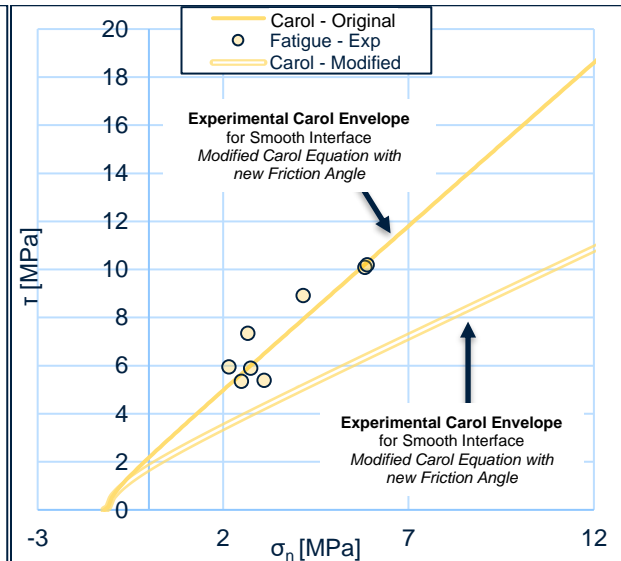


Figure 30: Modified Carol Envelope for WB-F-(F)

Table 9 presents an updated summary of bond parameters derived from the Carol envelope, including these modified friction angles for wirebrushed specimen. Figure 31 additionally provides a visual representation of the updated angles. The modified friction angles are consistent with values anticipated in the literature and are proportional to the average roughness of the wirebrushed specimens, which is lower than the sandblasted specimens. Comparing monotonic and fatigue-loaded envelopes, for both plain and fiber repair wirebrushed specimens, the angle of internal friction is shown to increase with a decrease of the extrapolated cohesion parameter.

Table 9: Updated Carol Parameters including Modified Friction Angle

| | Monotonic Carol | | | Fatigue Carol | | |
|-------------|-----------------|--------------|-------|---------------|--------------|-------|
| | c | ϕ (deg) | R^2 | c | ϕ (deg) | R^2 |
| SB-P | 6.26 | 52.1 | 0.85 | 4.00 | 53.9 | 0.94 |
| SB-F | 11.33 | 42.2 | 0.78 | 9.58 | 45.7 | 0.92 |
| WB-P | 1.78 | 37.6 | 0.90 | 0.71 | 41.2 | 0.87 |
| WB-F | 3.05 | 30.6 | 0.99 | 2.32 | 35.8 | 0.90 |

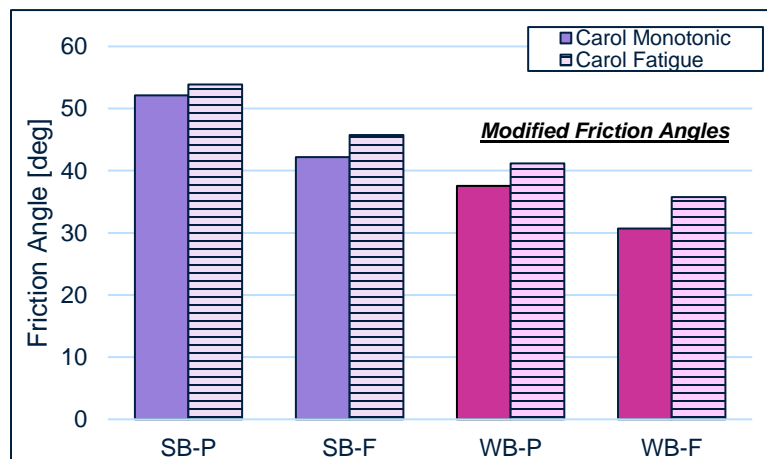


Figure 31: Carol Envelope Friction Angles, Updated for WB

4.4.4 Validation with Previous Data

Validation of the proposed semi-empirical modification factor was also completed using previous UBC slant shear data involving the same material mix designs with a left “as-cast” smooth interface. One of the datasets comprised a concrete substrate with a plain normal strength repair and the other dataset comprised a steel-fiber reinforced repair with 0.5% fibers by volume. Using the constraints and methodology as previously discussed (angle limit of 45°), the same modification factor of 1.5 was obtained through regression resulting in a modified friction angle and unchanged cohesion value. The original friction angle of 54° for the smooth specimens with plain repair mortar became 36°, while the original friction angle of 54.4° for the fiber repair became 36.3°. Where, in the previous investigation, the originally derived friction angles were inconsistent with the quantified surface roughness and derived frictional values for sandblasted (roughened) specimens, the modified values herein presented are more in agreement with the anticipated trends. The modified failure envelopes obtained for the smooth “as-cast” specimens studied previously at UBC are outlined further in Appendix E.

4.4.5 Modification Significance

A modification factor of 1.5 was obtained using regression of different slant shear data sets for wirebrushed (near smooth) and as-cast (smooth) interfaces:

$$\phi_{smooth} = \frac{\phi_{original}}{1.5} \quad (7)$$

Figure 32a presents the original Carol envelope plotted for all four specimen types examined in the current investigation under the monotonic protocol. Figure 32b consists of the modified Carol envelope for the wirebrushed specimens (WB-P and WB-F). A reduced slope is demonstrated by

wirebrushed fittings in 32b. Applying the original envelope (32a) to near-smooth interfaces for the purpose of empirical evaluation of interfacial shear bond strength may result in overestimation and inaccuracy, attributed to the limitations of the envelope model involving clusters of low strength data. However, the modified friction angle, used in conjunction with linear MC equation or original Carol plasticity equation, provides a more conservative estimate of smooth interfacial failure envelopes and therefore calculated shear bond capacity.

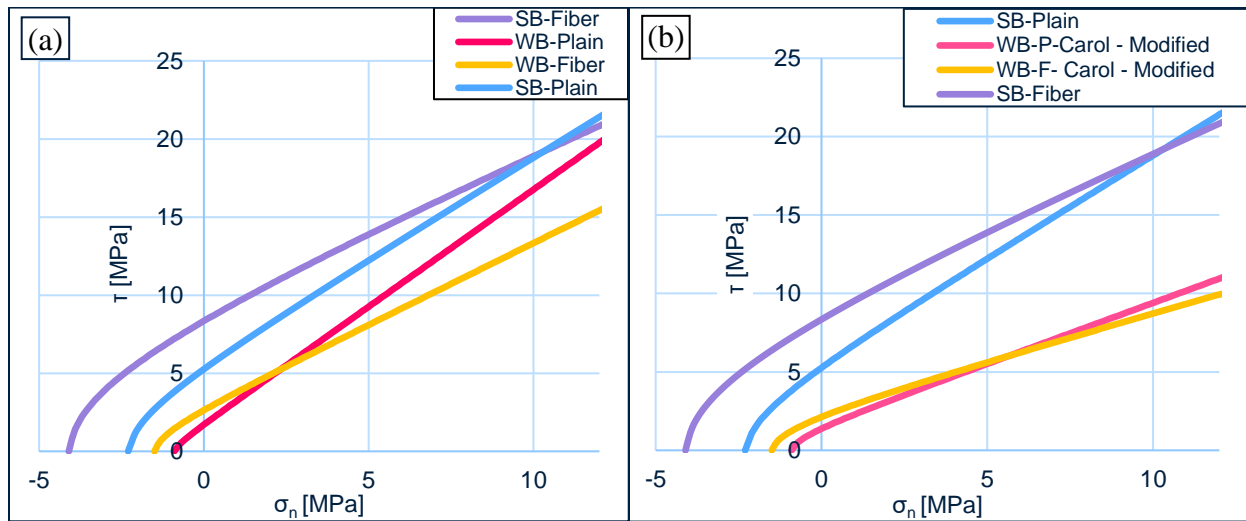


Figure 32: Monotonic Carol Envelopes before and after Implementation of Modification Factor

4.5 Discussion Summary

4.5.1 Monotonic Testing Protocol

In addition to a high frictional capacity, an adhesive bonding mechanism is prevalent at the roughened interface of sandblasted specimens. Bond adhesion is related to chemical and physical bonding at the micro-scale and depends on soundness, cleanliness, roughness of the substrate; the real surface contact area is a deciding parameter for adhesive bonding capacity [3], [6], [9]. The increase in surface contact area of the sandblasted specimens is more clearly communicated by the

“ R_a ” roughness value which quantifies the overall deviation of the surface profile, taken to be represent the interfacial surface area to a larger extent than MTD or ETD. The R_a value of the sandblasted interface is significantly higher than that of the wirebrushed interface, suggesting the substantial difference in contact area engaged by a roughened interface. Alternatively, the ETD/MTD appears to be generally representative of interfacial tortuosity and asperities which may provide greater insight to frictional effects.

In addition to an increase in surface contact area generated by roughening which can affect the chemical bonding capacity of an interface, roughening also imparts considerable physical micro-mechanical activity that contributes to adhesive bond such as localized interlocking, fracturing, and crushing. As well as a larger friction angle in sandblasted specimens which demonstrates the frictional capacity of the interface, these specimens also demonstrate significantly higher cohesive parameters extrapolated from failure envelopes – confirming that roughness is indeed a controlling factor for some types of adhesive bonding mechanisms.

DIC strain analysis prior to specimen failure reflects the superior adhesive bonding mechanism in sandblasted specimens compared to wirebrushed specimens by identifying fixed strain concentrations which are perpendicular to the interface and descriptive of an adhesive mechanism. Strain concentrations indicative of adhesion loss are more prevalent in wirebrushed specimens, reflective of overall lower bond strength, specifically adhesive capacity. The occurrences of these strain concentrations are more prevalent with increasing normal stress, suggesting a possible relationship with engaged frictional resistance as a result of localized shear slip due to adhesion loss.

The addition of steel fibers to sandblasted specimens resulted in a bond strength increase most pronounced in specimens with low proportions of applied stress, demonstrating beneficial

effects on a type of adhesive or cohesive bonding mechanism. The use of steel fibers in the repair material presents an increase in the extrapolated cohesion parameter more significantly in sandblasted specimens – potentially attributed to the high tortuosity and textural depth of interface (as described by ETD/MTD) which engages benefits at the interface. Although micro-dowel effects of steel fibers were observed by Zanotti et al., it is likely that the fibers in the current specimens may be contributing to adhesion and cohesion via enhanced material integrity, energy absorption, and crack-bridging at the interface as well [9], [17]. DIC strain analysis prior to specimen failure presents an increase in concentrations descriptive of an adhesive bonding mechanism in both fiber sandblasted and wirebrushed specimens which further suggests a general strengthening of adhesion due to the addition of fibers. Although, the addition of fibers to wirebrushed specimens does not necessarily increase bond strength significantly, it is reflected by an increase in extrapolated cohesion parameter. This is attributed to insufficient profile tortuosity required to engage fiber benefits generating tangible bond strength increases.

4.5.2 Fatigue Testing Protocol

The fatigue loading protocol consists of applying a high number of cycles comprising a low bond stress range ($n > 100$). Fatigue loading causes degradation of an adhesive bonding mechanism and its associated micro-parameters and is potentially induced by material damage and micro-cracking at and around the interface as well as damage to bond-adhesive mechanisms. Although present in both sandblasted and wirebrushed specimens, adhesive degradation is more significant in sandblasted specimens with a roughened interface. Adhesive degradation is reflected by a reduction in the extrapolated cohesion parameter as well as a slight increase in friction angle which may be attributed to a potential deviation of the “fracture plane” back into physical bond plane as adhesion is lost at the interface. Examining the bond envelopes, it is evident that the

fatigue loading protocol has a more significant impact on the extrapolated cohesion parameter, rather than the frictional coefficient.

“Macro-degradation” of the surface profile and its asperities (interfacial smoothing) is not induced by fatigue loading, demonstrated by bond strength results and failure envelope parameters that do not present significant changes in frictional capacity. Nonetheless adhesive degradation is still highly reliant on interfacial roughness in terms of chemical bonding (surface contact area) and physical micro-mechanisms (localized interlocking, fracturing, and crushing) and as such the magnitude of overall bond strength degradation is related to the roughness of the interface:

- *Physical Micro-Mechanical Effects:* localized micro-fracturing and crushing along the roughened interface from repeated loading, these are also disruptive of chemical bonding associated with surface contact area.
- *Chemical Bonding:* van der Waals forces which are primarily dependent on surface contact area which a function of roughness and is degraded as localized crushing, fracturing and damage of interface occurs.

In specimens with a smooth interface these micro-mechanisms are not as significant [9] and have less effects on the chemical forces. As such the adhesive degradation is to a much lower extent.

Bond strength results and extrapolated parameters are complemented by patterns in DIC strain analysis which present a decrease in strain concentrations descriptive of adhesive bond. Likewise, there is an increase in concentrations descriptive of adhesion loss (due to localized micro-fracturing and crushing); the changes in strain patterns are more severe in sandblasted specimens than wirebrushed specimens. Overall, the material damage induced by fatigue loading, which may be a factor contributing to adhesive degradation, is reflected in the visual ambiguity of strain patterns of fatigue specimens.

Use of steel fibers in the repair material may be beneficial in reducing adhesive degradation by maintaining material integrity and soundness of the interfacial zone through fiber ductility, energy absorption capacity, and crack-bridging [17]. Fibers were shown to retain adhesive bond capacity in bond strength results, failure envelopes and DIC strain analysis. Although the use of steel fibers in wirebrushed specimen was observed to have little benefit amongst monotonic specimens, in fatigue-loaded specimens this material was shown to retain some type of adhesive or cohesive bond mechanism demonstrated by an increase in extrapolated cohesion compared to plain specimens as well as present no decrease in shear bond strength compared to monotonically loaded specimens. This observation is consistent with the marks of Li and Matsumoto who, based on study of flexural specimens, suggest that the use of fibers can lead to fatigue crack arrest, and that fibers may be effective in extending the fatigue life of concrete structures [21].

4.5.3 Cyclic Testing Protocol

Cyclic bond strength results, strain analysis patterns, and extrapolated bond parameters are not clearly represented by the current data due to inconsistent trends; attributed to late stage strength gain of cyclic specimens tested at an older age. Further investigation is recommended to study the nature of interfacial degradation associated with a higher bond stress range applied. Overall DIC strain analysis also presented more ambiguous and mixed strain patterns which are difficult to define. These patterns are potentially associated with the counteractive strength increase of interface due to age mixed with degradation due to cyclic loading.

4.6 Codes & Design

The current Canadian code for the design of concrete structures, CSA A23.3, contains provisions for the design of interfacial shear bond, including bond parameters for different interface conditions. The predictive formula for evaluating shear bond strength is similar to the modified shear friction theory discussed and is a function of cohesion and friction, as well as shear friction reinforcement crossing the plane. For the purpose of examining code provisions in the context of the present investigation, the reinforcement component will not be considered, and rather the focus will be on the relevant bond parameters used for empirical evaluation of interfacial shear strength. For concrete placed against hardened concrete with the surface clean but not intentionally roughened, a cohesion strength of 0.25 MPa is recommended with a friction angle of 31° . Comparing these values to experimental parameters for wirebrushed specimens repaired with plain mortar derived using the modified Carol envelope, the cohesive strength is 1.8 MPa while the friction angle is 38° . Furthermore, for the same specimens under a fatigue loading protocol the cohesive strength is 0.7 MPa and the friction angle is 41° . Alternatively, for concrete placed against hardened concrete with a clean surface roughened to at least 5mm, CSA A23.3 recommends a cohesion value of 0.5 MPa and a friction angle of 45° . Bond parameters derived using the Carol envelope for sandblasted specimens with a plain mortar repair suggest a cohesive strength of 6.3 MPa and a friction angle of 52° . Sandblasted specimens subjected to fatigue loading resulted in a cohesive strength of 4.0 MPa and a friction angle of 54° . Therefore, based on the present slant shear experimental results, CSA A23.3 code provisions for interfacial cohesion and friction angles are conservative for specimens subjected to both monotonic and fatigue loading protocols. A comparison of bond parameters outlined in the code and those derived experimentally are presented in Figure 33.

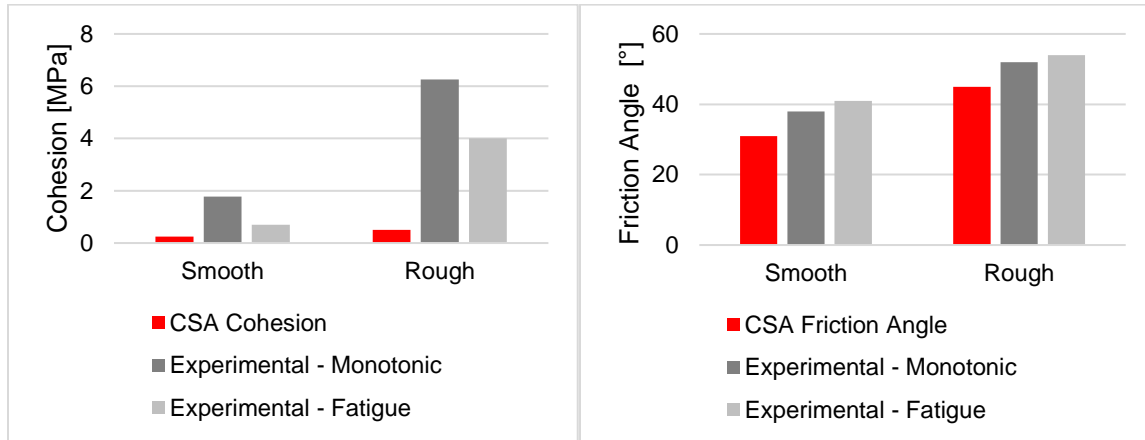


Figure 33: Comparison of Bond Parameter – CSA A23.3 & Experimental

Several researchers have also recommended provisions for the design of interfaces in relation to cyclic and fatigue loading. Randl recommends, that, for a rigid bond without reinforcement across the interface, the adhesive bond strength should be reduced to 50% [6]. Mattock suggests that the overall shear strength of a concrete interface under cyclic loading shall be 90% of the monotonic strength for rough interfaces and 60% for smooth interfaces assuming bond between concrete parts is not existent and the interface behaves under pure sliding [35]. In order to examine these recommendations in the context of the current experimental investigation, sandblasted specimens will be categorized as rough interfaces and wirebrushed specimens will be categorized as smooth interfaces. For simplification purposes only the adhesive/cohesive bond strength will be considered, although Mattock's recommendation refers to overall shear strength consisting of cohesive strength and friction. Cohesion parameters derived for fatigue-loaded specimens using the Carol envelope are presented in Table 10 as a percentage of the respective monotonic cohesion. The guideline proposed by Randl is consistent for roughened interfaces as well as the wirebrushed interface with fiber-reinforced repair. However, the guideline suggested

by Mattock would seemingly overestimate the fatigue capacity of the sandblasted specimens as well as the plain repair wirebrushed interface. Therefore, the recommendation of adhesive bond strength reduction of 50% by Randl is more consistent with the current experimental results for fatigue-loaded slant-shear interfaces.

Table 10: Comparison of Adhesive Strength for Cyclic/Fatigue Loading

| | Randl [3] | Mattock [35] | Experimental Fatigue |
|----------------------|-----------|--------------|----------------------|
| SB-P (Rough) | 50% | 90% | 67% |
| SB-F (Rough) | 50% | 90% | 85% |
| WB-P (Smooth) | 50% | 60% | 40% |
| WB-F (Smooth) | 50% | 60% | 76% |

Chapter 5: Conclusion

5.1 Concluding Remarks

The purpose of this study was to investigate the effects of fatigue loading on interfacial bond and the associated bond parameters. Modified slant shear tests were conducted at the University of British Columbia under monotonic, fatigue, and cyclic loading protocols examining the effects of interfacial roughness and steel-fiber reinforcement. Based on the bond strength results, failure envelopes were modelled in order to extrapolate the relevant bond parameters: cohesion and friction angle. Digital Image Correlation was also used to assess the strain patterns in the specimens prior to failure. The main conclusions can be summarized as follows:

- a) Independent of the applied normal stress in a slant shear specimen, there is a type of adhesive bonding mechanism active at the interface. This adhesion is related to chemical bonding at the micro-scale, engaged by the interfacial surface contact area, as well physical micro-mechanical activities such as localized fracturing, interlocking, and crushing.
- b) In addition to the improvement in frictional capacity, interfacial roughness, imparted by sandblasting, increases the surface contact area and activates physical micro-mechanisms. As such the adhesive bonding mechanism is highly evident in sandblasted specimens, demonstrated by the presented bond strength results, strain patterns, and extrapolated cohesion parameters. The adhesive bond is exhibited to a lesser extent in the wirebrushed, near-smooth specimens, attributed to a lack of localized bonding characteristics and overall reduced contact area.
- c) The Average Roughness (R_a), as presented in Fib Model Code 2010 and defined as the arithmetic deviation from a mean line, is a roughness quantification method that is more representative of the potential interfacial surface contact area, a deciding parameter for

adhesive bonding capacity. Quantifiers such as Estimated Textural Depth (ETD) and Mean Textural Depth (MTD) are more representative of frictional capacity.

- d) When subjected to a fatigue loading protocol, in the form of applied loads repeated at a high speed and low stress range, the adhesive bond mechanism at the interface degrades, resulting in a reduced bond strength, modified strain distributions, and decrease in extrapolated cohesion. Adhesive degradation is more pronounced in sandblasted specimens, attributed to greater deterioration of micro-mechanical features exposed to repeated loads as well as material deterioration of the surface contact area. Wirebrushed specimens do not demonstrate the same extent of adhesive deterioration.
- e) Interfacial smoothing or decrease of interfacial “macro” roughness is not exhibited by fatigue-loaded specimens. Extrapolated friction angles are not significantly modified and specimen orientations with a higher proportion of frictional resistance (30°) experience the least amount of bond strength decrease.
- f) The use of steel fibers in the repair material is beneficial in increasing adhesive capacity, primarily in sandblasted specimens, demonstrated by bond strength and cohesion parameter increases, as well as strain patterns. Interfacial tortuosity is required to activate the strengthening effects of steel fibers. Notwithstanding, steel fibers contribute in both sandblasted and wirebrushed specimens by retaining adhesive bond during fatigue loading. This is attributed to supporting material soundness at and near the interface.
- g) Both the Linear Mohr-Coulomb and the Carol Plasticity predictive models overestimate the angle of internal friction for wirebrushed (near-smooth) specimens, due to challenges with large clusters of low-strength data. A semi-empirical reduction factor of 1.5 applied to the extrapolated friction angle is proposed to obtain a more conservative estimate of the

failure envelope for smooth and near smooth specimens. This factor is validated with a total of six datasets from present and previous experimental investigations at UBC.

- h) A comparison of the experimental results with code provisions suggests that CSA A23.3 code provisions for interfacial cohesion and friction angles are conservative for slant shear specimens subjected to both monotonic and fatigue loading protocols. An adhesive bond strength reduction of 50%, as suggested by Randl, is also generally conservative for the current experimental results for fatigue-loaded slant-shear interfaces.

5.2 Recommendations for Future Work

Further investigation is recommended to examine interfacial bond behaviour under a cyclic loading protocol involving a load applied at a rate of 0.250 MPa/s between 10% and 75% of the peak monotonic load for a low number of cycles ($6 < n < 100$). Conclusive cyclic loading results may provide additional insight to the current works discussing the adhesive degradation exhibited by fatigue-loaded slant shear specimens. Repeated loading at a higher bond stress range may demonstrate “interfacial smoothing” along the slant shear bond plane as indicated in shear push-off specimens in [22]. Additionally, potential changes to the extrapolated internal friction angle may be identified, as well as the effects of different interfacial roughness profiles and fiber reinforcement in the repair.

It is also recommended to incorporate the use of strain gauges or shear slip measuring devices in order to quantify the magnitude of shear slip that occurs prior to the brittle failure of the slant shear specimens. On the basis that shear slip occurs upon failure of adhesive bond [6], the a quantification of slip may provide significant insight into the frictional capacity of the interface and how it may degrade when subjected to different loading protocols.

References

- [1] Canadian Infrastructure Report Card, “Monitoring the State of Canada's Core Public Infrastructure: The Canadian Infrastructure Report Card 2019,” 2019. [Online]. Available: <http://canadianinfrastructure.ca/downloads/canadian-infrastructure-report-card-2019.pdf>
- [2] *Considerations for the Design of Concrete Structures Subjected to Fatigue Loading*, ACI Committee Report 215R-74, ACI Committee 215, American Concrete Institute, Farmington Hills, MI, 1992 (Revised).
- [3] A. D. Espeche and J. León, “Estimation of bond strength envelopes for old-to-new concrete interfaces based on a cylinder splitting test,” *Constr. Build. Mater.*, vol. 25, no. 3, pp. 1222–1235, Mar. 2011, doi: 10.1016/j.conbuildmat.2010.09.032.
- [4] C. Zanotti and N. Randl, “Are concrete-concrete bond tests comparable?,” *Cem. Concr. Compos.*, vol. 99, pp. 80–88, May 2019, doi: 10.1016/j.cemconcomp.2019.02.012.
- [5] C. Zanotti, N. Banthia, and G. Plizzari, “A study of some factors affecting bond in cementitious fiber reinforced repairs,” *Cem. Concr. Res.*, vol. 63, pp. 117–126, Sep. 2014, doi: 10.1016/j.cemconres.2014.05.008.
- [6] N. Randl, “Design recommendations for interface shear transfer in *fib* Model Code 2010,” *Struct. Concr.*, vol. 14, no. 3, pp. 230–241, Sep. 2013, doi: 10.1002/suco.201300003.
- [7] P. M. D. Santos and E. N. B. S. Júlio, “A state-of-the-art review on shear-friction,” *Eng. Struct.*, vol. 45, pp. 435–448, Dec. 2012, doi: 10.1016/j.engstruct.2012.06.036.
- [8] Ł. Sadowski, *Adhesion in Layered Cement Composites*, vol. 101. Cham: Springer International Publishing, 2019.
- [9] C. Zanotti, G. Rostagno, and B. Tingley, “Further evidence of interfacial adhesive bond strength enhancement through fiber reinforcement in repairs,” *Constr. Build. Mater.*, vol. 160, pp. 775–785, Jan. 2018, doi: 10.1016/j.conbuildmat.2017.12.140.

- [10] M. E. Mohamad and I. S. Ibrahim, "Interface Shear Strength of Concrete-to-Concrete Bond with and without Projecting Steel Reinforcement," *J. Teknol.*, vol. 75, no. 1, Jun. 2015, doi: 10.11113/jt.v75.3707.
- [11] S. Austin, P. Robins, and Y. Pan, "Shear bond testing of concrete repairs," *Cem. Concr. Res.*, vol. 29, no. 7, pp. 1067–1076, Jul. 1999, doi: 10.1016/S0008-8846(99)00088-5.
- [12] *Standard Test Method for Measuring Pavement Macrotexture Depth Using a Volumetric Technique*, ASTM Standard E965-15, ASTM International, West Conshohocken, PA, 2015.
- [13] Y. Du, "Durability Performance of Eco-Friendly Ductile Cementitious Composite (EDCC) as a Repair Material" M.A.Sc. thesis, Dept. Civil Eng., Univ. British Columbia, Vancouver, BC, 2016.
- [14] G. Rostagno, "Enhancement of bond in concrete repairs through fiber reinforcement (Miglioramento dell'aderenza in calcestruzzi da riparazione mediante fibrorinforzo)," M.A.Sc. thesis, Dept. Civil Eng., Univ. Brescia, Brescia, Italy, 2016.
- [15] *Standard Practice for Calculating Pavement Macrotexture Mean Profile Depth*, ASTM Standard E1845-15, ASTM International, West Conshohocken, PA, 2015.
- [16] A. Bentur and S. Mindess, *Fibre Reinforced Cementitious Composites*, 2nd ed. Boca Raton, FL, USA: CRC Press Taylor & Francis Group, 1990.
- [17] N. Banthia, K. Chokri, Y. Ohama, and S. Mindess, "Fiber-reinforced cement based composites under tensile impact," *Adv. Cem. Based Mater.*, vol. 1, no. 3, pp. 131–141, Mar. 1994, doi: 10.1016/1065-7355(94)90044-2.
- [18] *Standard Test Method for Bond Strength of Epoxy-Rein Systems Used With Concrete By Slant Shear*, ASTM Standard C882-13a, ASTM International, West Conshohocken, PA, 2013.
- [19] I. Carol, P. C. Prat, and C. M. López, "Normal/Shear Cracking Model: Application to Discrete Crack Analysis," *J. Eng. Mech.*, vol. 123, no. 8, pp. 765–773, Aug. 1997, doi: 10.1061/(ASCE)0733-9399(1997)123:8(765).

- [20] J. Cao and D. D. L. Chung, "Degradation of the bond between old and new mortar under cyclic shear loading, monitored by contact electrical resistance measurement," *Cem. Concr. Res.*, vol. 31, no. 11, pp. 1647–1651, Nov. 2001, doi: 10.1016/S0008-8846(01)00607-X.
- [21] V. C. Li and T. Matsumoto, "Fatigue crack growth analysis of fiber reinforced concrete with effect of interfacial bond degradation," *Cem. Concr. Compos.*, vol. 20, no. 5, pp. 339–351, Oct. 1998, doi: 10.1016/S0958-9465(98)00010-9.
- [22] T. P. Tassios and E. N. Vintzēleou, "Concrete-to-Concrete Friction," *J. Struct. Eng.*, vol. 113, no. 4, pp. 832–849, Apr. 1987, doi: 10.1061/(ASCE)0733-9445(1987)113:4(832).
- [23] B. Hu, Y. Li, and Y. Liu, "Dynamic slant shear bond behavior between new and old concrete," *Constr. Build. Mater.*, vol. 238, p. 117779, Mar. 2020, doi: 10.1016/j.conbuildmat.2019.117779.
- [24] D. Figueira, C. Sousa, R. Calçada, and A. S. Neves, "Push-Off Tests in the Study of Cyclic Behavior of Interfaces between Concretes Cast at Different Times," *J. Struct. Eng.*, vol. 142, no. 1, p. 04015101, Jan. 2016, doi: 10.1061/(ASCE)ST.1943-541X.0001364.
- [25] K. C. G. Ong, P. Paramasivam, and M. Subramanian, "Cyclic Behavior of Steel-Fiber Mortar Overlaid Concrete Beams," *J. Mater. Civ. Eng.*, vol. 9, no. 1, pp. 21–28, Feb. 1997, doi: 10.1061/(ASCE)0899-1561(1997)9:1(21).
- [26] M. Anderson, "Effect of FRCM Repair on the Bond Behaviour of Corroded Reinforced Concrete Beams Subjected to Static and Cyclic Loading," M.S. thesis, Univ. Minnesota, Minneapolis, MN, 2017.
- [27] J. Walraven, "Rough Cracks Subjected to Earthquake Loading," *J. Struct. Eng.*, vol. 120, no. 5, pp. 1510-1524, May 1994, doi: 10.1061/(ASCE)0733-9445(1994)120:5(1510).
- [28] M. Naderi, "Effects of Cyclic Loading, Freeze-Thaw and Temperature Changes on Shear Bond Strengths of Different Concrete Repair Systems," *J. Adhes.*, vol. 84, no. 9, pp. 743–763, Sep. 2008, doi: 10.1080/00218460802352934.

- [29] R. A. Daud, “Behaviour of Reinforced Concrete Slabs Strengthened Externally with Two-Way FRP Sheets Subjected to Cyclic Loads,” Ph.D. dissertation, Dept. of Mech., Aerospace, Civil Eng., Univ. Manchester, Manchester, UK, 2015.
- [30] *Report on Bond of Steel Reinforcing Bars under Cyclic Loads*, ACI Committee Report 408.2R-12, Joint ACI-ASCE Committee 408, American Concrete Institute, Farmington Hills, MI, 2012.
- [31] *Strength Evaluation of Existing Concrete Buildings*, ACI Committee Report 437R-03, ACI Committee 437, American Concrete Institute, Farmington Hills, MI, 2003.
- [32] *Load Tests of Concrete Structures: Methods, Magnitude, Protocols, and Acceptance Criteria*, ACI Committee Report 437.1R-07, ACI Committee 437, American Concrete Institute, Farmington Hills, MI, 2007.
- [33] *Report on Measuring Mechanical Properties of Hardened Fiber-Reinforced Concrete*, ACI Committee Report 544.9R-17, ACI Committee 544, American Concrete Institute, Farmington Hills, MI, 2017.
- [34] *Standard Test Methods for Cyclic (Reversed) Load Test for Shear Resistance of Vertical Elements of the Lateral Force Resisting Systems for Buildings*, ASTM Standard E2126-19, ASTM International, West Conshohocken, PA, 2019.
- [35] A. K. Mattock, “Report SM 76-3 Shear Transfer under Monotonic Loading, Across an Interface between Concretes Cast at Different Times,” Dept. Civil Eng., Univ. Washington, Seattle, WA, USA, Sept. 1976.
- [36] S. G. Shah and J. M. Chandra Kishen, “Fracture Properties of Concrete–Concrete Interfaces Using Digital Image Correlation,” *Exp. Mech.*, vol. 51, no. 3, pp. 303–313, Mar. 2011, doi: 10.1007/s11340-010-9358-y.
- [37] Y. Yao, “Application of 2D DIC method to Damage Characterization of Cementitious Composites under Dynamic Tensile Loads,” M.S. thesis, Arizona State Univ., Tempe, AZ, 2013.

- [38] H. Koerber, J. Xavier, and P. P. Camanho, “High strain rate characterisation of unidirectional carbon-epoxy IM7-8552 in transverse compression and in-plane shear using digital image correlation,” *Mech. Mater.*, vol. 42, no. 11, pp. 1004–1019, Nov. 2010, doi: 10.1016/j.mechmat.2010.09.003.
- [39] P. C. Wilbur, “Damage Identification in Reinforced Concrete Beams using Digital Image Correlation,” M.A.Sc. thesis, Dept. Civil Env. Eng., Univ. Windsor, Windsor, Ontario, 2011.
- [40] *Standard Test Method for Compressive Strength of Cylindrical Concrete Specimens*, ASTM Standard C39-18, ASTM International, West Conshohocken, PA, 2018.
- [41] D. R. Morgan, “Compatibility of concrete repair materials and systems,” *Constr. Build. Mater.*, vol. 10, no. 1, pp. 57–67, Feb. 1996, doi: 10.1016/0950-0618(95)00060-7.

Appendices

Appendix A - Slant Shear Test Results

The experimental failure loads, failure modes, and corresponding applied, normal, and shear stresses along the bond plane are presented for the slant shear specimens considered in the presented results and analysis.

A.1 Monotonic Loading Protocol

Table 11: Monotonic Slant Shear Test Results

| Specimen | # | V_f | P_{max} | σ_0 | σ_n | τ_n | Failure Mode |
|-------------|---|-------|-----------|------------|------------|----------|--------------|
| SB-P-30-(M) | 1 | 0 | 139.58 | 31.59 | 7.90 | 13.68 | MIXED |
| SB-P-30-(M) | 2 | 0 | 178.76 | 40.46 | 10.12 | 17.52 | INTERFACE |
| SB-P-30-(M) | 3 | 0 | 212.12 | 48.01 | 12.00 | 20.79 | MATERIAL |
| SB-P-30-(M) | 4 | 0 | 206.61 | 46.77 | 11.69 | 20.25 | INTERFACE |
| SB-P-25-(M) | 1 | 0 | 90.47 | 29.97 | 5.35 | 11.48 | MATERIAL |
| SB-P-25-(M) | 2 | 0 | 168.37 | 55.77 | 9.96 | 21.36 | MIXED |
| SB-P-25-(M) | 3 | 0 | 131.22 | 43.47 | 7.76 | 16.65 | MATERIAL |
| SB-P-25-(M) | 1 | 0 | 134.81 | 44.65 | 5.22 | 14.35 | INTERFACE |
| SB-P-20-(M) | 2 | 0 | 156.43 | 51.81 | 6.06 | 16.65 | MATERIAL |
| SB-P-20-(M) | 3 | 0 | 68.27 | 22.61 | 2.65 | 7.27 | INTERFACE |
| SB-P-20-(M) | 4 | 0 | 119.01 | 39.42 | 4.61 | 12.67 | INTERFACE |
| SB-P-20-(M) | 5 | 0 | 81.20 | 26.90 | 3.15 | 8.64 | MIXED |
| SB-F-30-(M) | 1 | 0.5 | 198.14 | 44.85 | 11.21 | 19.42 | INTERFACE |
| SB-F-30-(M) | 2 | 0.5 | 176.19 | 39.88 | 9.97 | 17.27 | MATERIAL |
| SB-F-25-(M) | 1 | 0.5 | 125.51 | 41.57 | 7.42 | 15.92 | INTERFACE |
| SB-F-25-(M) | 2 | 0.5 | 132.33 | 43.83 | 7.83 | 16.79 | MATERIAL |
| SB-F-25-(M) | 3 | 0.5 | 120.15 | 39.80 | 7.11 | 15.24 | INTERFACE |
| SB-F-25-(M) | 4 | 0.5 | 158.26 | 52.42 | 9.36 | 20.08 | MATERIAL |
| SB-F-25-(M) | 5 | 0.5 | 138.25 | 45.79 | 8.18 | 17.54 | MIXED |
| SB-F-20-(M) | 1 | 0.5 | 156.90 | 51.97 | 6.08 | 16.70 | INTERFACE |
| SB-F-20-(M) | 2 | 0.5 | 140.47 | 46.53 | 5.44 | 14.95 | INTERFACE |
| SB-F-20-(M) | 3 | 0.5 | 125.53 | 41.58 | 4.86 | 13.36 | MATERIAL |
| SB-F-20-(M) | 4 | 0.5 | 118.01 | 39.09 | 4.57 | 12.56 | MATERIAL |
| SB-F-20-(M) | 5 | 0.5 | 156.12 | 51.71 | 6.05 | 16.62 | INTERFACE |
| SB-F-20-(M) | 6 | 0.5 | 108.00 | 35.77 | 4.18 | 11.50 | INTERFACE |
| WB-P-30-(M) | 1 | 0 | 46.45 | 10.51 | 2.63 | 4.55 | INTERFACE |
| WB-P-30-(M) | 2 | 0 | 147.80 | 33.45 | 8.36 | 14.49 | MIXED |
| WB-P-30-(M) | 3 | 0 | 59.13 | 13.38 | 3.35 | 5.80 | INTERFACE |
| WB-P-30-(M) | 4 | 0 | 53.50 | 12.11 | 3.03 | 5.24 | MIXED |
| WB-P-25-(M) | 1 | 0 | 45.67 | 15.13 | 2.70 | 5.79 | INTERFACE |
| WB-P-25-(M) | 2 | 0 | 61.21 | 20.28 | 3.62 | 7.77 | INTERFACE |
| WB-P-20-(M) | 1 | 0 | 56.44 | 18.69 | 2.19 | 6.01 | MIXED |
| WB-P-20-(M) | 2 | 0 | 66.68 | 22.09 | 2.58 | 7.10 | MIXED |

| Specimen | # | V_f | P_{max} | σ_0 | σ_n | τ_n | Failure Mode |
|-------------|---|-------|-----------|------------|------------|----------|--------------|
| WF-P-30-(M) | 1 | 0.5 | 68.68 | 15.55 | 3.89 | 6.73 | INTERFACE |
| WF-P-30-(M) | 2 | 0.5 | 74.32 | 16.82 | 4.21 | 7.28 | MIXED |
| WF-P-30-(M) | 3 | 0.5 | 68.38 | 15.48 | 3.87 | 6.70 | INTERFACE |
| WF-P-30-(M) | 4 | 0.5 | 9.41 | 2.13 | 0.53 | 0.92 | INTERFACE |
| WF-P-25-(M) | 1 | 0.5 | 43.62 | 14.45 | 2.58 | 5.53 | INTERFACE |
| WF-P-25-(M) | 2 | 0.5 | 49.92 | 16.53 | 2.95 | 6.33 | INTERFACE |
| WF-P-25-(M) | 3 | 0.5 | 38.09 | 12.62 | 2.25 | 4.83 | INTERFACE |
| WF-P-20-(M) | 1 | 0.5 | 50.99 | 16.89 | 1.98 | 5.43 | INTERFACE |
| WF-P-20-(M) | 2 | 0.5 | 42.03 | 13.92 | 1.63 | 4.47 | INTERFACE |
| WF-P-20-(M) | 3 | 0.5 | 33.46 | 11.08 | 1.30 | 3.56 | INTERFACE |
| WF-P-20-(M) | 4 | 0.5 | 45.78 | 15.16 | 1.77 | 4.87 | INTERFACE |

A.2 Fatigue Loading Protocol

Italicized entries refer to specimens not considered due to premature failure during fatigue testing.

Table 12: Fatigue Slant Shear Test Results

| Specimen | # | V_f | P_{max} | σ_0 | σ_n | τ_n | Failure Mode |
|--------------------|----------|------------|--------------|--------------|-------------|-------------|-------------------|
| <i>SB-P-30-(F)</i> | <i>1</i> | <i>0</i> | <i>68.96</i> | <i>15.61</i> | <i>3.90</i> | <i>6.76</i> | <i>CY 1 - MAT</i> |
| SB-P-30-(F) | 2 | 0 | 180.67 | 40.89 | 10.22 | 17.71 | MATERIAL |
| SB-P-30-(F) | 3 | 0 | 175.75 | 39.78 | 9.95 | 17.23 | MATERIAL |
| SB-P-25-(F) | 1 | 0 | 62.21 | 20.61 | 3.68 | 7.89 | CY 500 - MIX |
| SB-P-25-(F) | 2 | 0 | 58.77 | 19.47 | 3.48 | 7.46 | CY 65 - MAT |
| SB-P-25-(F) | 3 | 0 | 61.46 | 20.36 | 3.64 | 7.80 | CY 611 - MAT |
| SB-P-25-(F) | 4 | 0 | 102.85 | 34.07 | 6.08 | 13.05 | MIXED |
| SB-P-20-(F) | 1 | 0 | 107.71 | 35.68 | 4.17 | 11.47 | MATERIAL |
| <i>SB-P-20-(F)</i> | <i>2</i> | <i>0</i> | <i>41.37</i> | <i>13.70</i> | <i>1.60</i> | <i>4.40</i> | <i>CY 4 - MAT</i> |
| SB-P-20-(F) | 3 | 0 | 80.29 | 26.59 | 3.11 | 8.55 | MATERIAL |
| SB-F-30-(F) | 1 | 0.5 | 209.67 | 47.46 | 11.87 | 20.55 | INTERFACE |
| SB-F-30-(F) | 2 | 0.5 | 230.45 | 52.16 | 13.04 | 22.59 | INTERFACE |
| SB-F-30-(F) | 3 | 0.5 | 211.03 | 47.77 | 11.94 | 20.68 | MATERIAL |
| SB-F-25-(F) | 1 | 0.5 | 108.71 | 36.01 | 6.43 | 13.79 | INTERFACE |
| SB-F-25-(F) | 2 | 0.5 | 112.32 | 37.20 | 6.64 | 14.25 | MIXED |
| SB-F-25-(F) | 3 | 0.5 | 132.00 | 43.72 | 7.81 | 16.75 | MATERIAL |
| SB-F-20-(F) | 1 | 0.5 | 134.81 | 44.65 | 5.22 | 14.35 | MATERIAL |
| SB-F-20-(F) | 2 | 0.5 | 110.85 | 36.72 | 4.29 | 11.80 | MATERIAL |
| SB-F-20-(F) | 3 | 0.5 | 157.73 | 52.25 | 6.11 | 16.79 | INTERFACE |
| WB-P-30-(F) | 1 | 0 | 81.20 | 18.38 | 4.60 | 7.96 | INTERFACE |
| WB-P-30-(F) | 2 | 0 | 52.28 | 11.83 | 2.96 | 5.12 | INTERFACE |
| WB-P-25-(F) | 1 | 0 | 47.14 | 15.61 | 2.79 | 5.98 | CY 500 - IF |
| WB-P-25-(F) | 2 | 0 | 54.47 | 18.04 | 3.22 | 6.91 | INTERFACE |
| WB-P-20-(F) | 1 | 0 | 53.69 | 17.78 | 2.08 | 5.72 | INTERFACE |
| WB-P-20-(F) | 2 | 0 | 89.78 | 29.74 | 3.48 | 9.56 | INTERFACE |
| WB-P-20-(F) | 3 | 0 | 122.56 | 40.60 | 4.75 | 13.05 | MATERIAL |
| <i>WB-F-30-(F)</i> | <i>1</i> | <i>0.5</i> | <i>36.84</i> | <i>8.34</i> | <i>2.08</i> | <i>3.61</i> | <i>CY 2 - IF</i> |
| WB-F-30-(F) | 2 | 0.5 | 102.91 | 23.29 | 5.82 | 10.09 | INTERFACE |

| Specimen | # | V_f | P_{max} | σ_0 | σ_n | τ_n | Failure Mode |
|-------------|---|-------|-----------|------------|------------|----------|--------------|
| WB-F-30-(F) | 3 | 0.5 | 54.94 | 12.44 | 3.11 | 5.39 | INTERFACE |
| WB-F-30-(F) | 4 | 0.5 | 103.94 | 23.53 | 5.88 | 10.19 | INTERFACE |
| WB-F-25-(F) | 1 | 0.5 | 42.09 | 13.94 | 2.49 | 5.34 | INTERFACE |
| WB-F-25-(F) | 2 | 0.5 | 46.45 | 15.38 | 2.75 | 5.89 | INTERFACE |
| WB-F-25-(F) | 3 | 0.5 | 70.26 | 23.27 | 4.16 | 8.91 | INTERFACE |
| WB-F-20-(F) | 1 | 0.5 | 55.77 | 18.47 | 2.16 | 5.94 | INTERFACE |
| WB-F-20-(F) | 2 | 0.5 | 93.75 | 31.05 | 3.63 | 9.98 | INTERFACE |
| WB-F-20-(F) | 3 | 0.5 | 68.88 | 22.81 | 2.67 | 7.33 | INTERFACE |

A.3 Cyclic Loading Protocol

Italicized entries refer to specimens not considered due to premature failure during cyclic testing.

Table 13: Cyclic Slant Shear Test Results

| Specimen | # | V_f | P_{max} | σ_0 | σ_n | τ_n | Failure Mode |
|--------------------|----------|----------|---------------|--------------|-------------|--------------|---------------------|
| SB-P-30-(C) | 1 | 0 | 157.01 | 35.54 | 8.89 | 15.39 | CY 32 - MAT |
| SB-P-30-(C) | 2 | 0 | 165.90 | 37.55 | 9.39 | 16.26 | MATERIAL |
| <i>SB-P-30-(C)</i> | <i>3</i> | <i>0</i> | <i>116.98</i> | <i>26.48</i> | <i>6.62</i> | <i>11.47</i> | <i>CY 1 - MIXED</i> |
| <i>SB-P-25-(C)</i> | <i>1</i> | <i>0</i> | <i>80.31</i> | <i>26.60</i> | <i>4.75</i> | <i>10.19</i> | <i>CY 1 - MAT</i> |
| SB-P-25-(C) | 2 | 0 | 90.00 | 29.81 | 5.32 | 11.42 | CY 3 - MAT |
| SB-P-20-(C) | 1 | 0 | 148.16 | 49.07 | 5.74 | 15.77 | INTERFACE |
| SB-P-20-(C) | 2 | 0 | 162.70 | 53.89 | 6.30 | 17.32 | INTERFACE |
| SB-P-20-(C) | 3 | 0 | 164.98 | 54.65 | 6.39 | 17.56 | INTERFACE |
| SB-P-20-(C) | 4 | 0 | 156.43 | 51.81 | 6.06 | 16.65 | MATERIAL |
| SB-F-30-(C) | 1 | 0.5 | 199.90 | 45.25 | 11.31 | 19.59 | INTERFACE |
| SB-F-30-(C) | 2 | 0.5 | 161.04 | 36.45 | 9.11 | 15.78 | MATERIAL |
| SB-F-30-(C) | 3 | 0.5 | 208.04 | 47.09 | 11.77 | 20.39 | INTERFACE |
| SB-F-25-(C) | 1 | 0.5 | 156.99 | 52.00 | 9.29 | 19.92 | INTERFACE |
| SB-F-25-(C) | 2 | 0.5 | 96.11 | 31.83 | 5.69 | 12.19 | CY 60 - MAT |
| SB-F-25-(C) | 3 | 0.5 | 161.70 | 53.56 | 9.57 | 20.52 | INTERFACE |
| SB-F-25-(C) | 4 | 0.5 | 180.42 | 59.76 | 10.67 | 22.89 | INTERFACE |
| SB-F-20-(C) | 1 | 0.5 | 165.76 | 54.90 | 6.42 | 17.65 | MATERIAL |
| SB-F-20-(C) | 2 | 0.5 | 178.10 | 58.99 | 6.90 | 18.96 | INTERFACE |
| SB-F-20-(C) | 3 | 0.5 | 144.80 | 47.96 | 5.61 | 15.41 | INTERFACE |
| WB-P-30-(C) | 1 | 0 | 50.97 | 11.54 | 2.88 | 5.00 | INTERFACE |
| WB-P-30-(C) | 2 | 0 | 92.56 | 20.95 | 5.24 | 9.07 | INTERFACE |
| <i>WB-P-30-(C)</i> | <i>3</i> | <i>0</i> | <i>4.61</i> | <i>1.04</i> | <i>0.26</i> | <i>0.45</i> | <i>PRELM - IF</i> |
| WB-P-25-(C) | 1 | 0 | 43.34 | 14.35 | 2.56 | 5.50 | INTERFACE |
| WB-P-25-(C) | 2 | 0 | 47.81 | 15.83 | 2.83 | 6.07 | INTERFACE |
| WB-P-25-(C) | 3 | 0 | 40.73 | 13.49 | 2.41 | 5.17 | INTERFACE |
| WB-P-20-(C) | 1 | 0 | 57.63 | 19.09 | 2.23 | 6.14 | CY 95 - IF |
| WB-P-20-(C) | 2 | 0 | 92.64 | 30.68 | 3.59 | 9.86 | INTERFACE |
| <i>WB-P-20-(C)</i> | <i>3</i> | <i>0</i> | <i>51.94</i> | <i>17.20</i> | <i>2.01</i> | <i>5.53</i> | <i>CY 1 - INT</i> |
| WB-F-30-(C) | 1 | 0.5 | 78.84 | 17.85 | 4.46 | 7.73 | INTERFACE |

| Specimen | # | V_f | P_{max} | σ_0 | σ_n | τ_n | Failure Mode |
|--------------------|----------|-------------------------|-----------------------------|------------------------------|------------------------------|----------------------------|---------------------|
| WB-F-30-(C) | 2 | 0.5 | 35.62 | 8.06 | 2.02 | 3.49 | CY 1 - IF |
| WB-F-30-(C) | 3 | 0.5 | 39.42 | 8.92 | 2.23 | 3.86 | CY 1 - IF |
| WB-F-30-(C) | 4 | 0.5 | 47.42 | 10.73 | 2.68 | 4.65 | CY 1 - IF |
| WB-F-25-(C) | 1 | 0.5 | 61.74 | 20.45 | 3.65 | 7.83 | INTERFACE |
| <i>WB-F-25-(C)</i> | <i>2</i> | <i>0.5</i> | <i>14.72</i> | <i>4.87</i> | <i>0.87</i> | <i>1.87</i> | <i>CY 1 - IF</i> |
| <i>WB-F-25-(C)</i> | <i>3</i> | <i>0.5</i> | <i>10.78</i> | <i>3.57</i> | <i>0.64</i> | <i>1.37</i> | <i>CY 1 - IF</i> |
| WB-F-25-(C) | 4 | 0.5 | 64.88 | 21.49 | 3.84 | 8.23 | INTERFACE |
| WB-F-20-(C) | 1 | 0.5 | 103.38 | 34.24 | 4.01 | 11.01 | INTERFACE |
| WB-F-20-(C) | 2 | 0.5 | 135.61 | 44.92 | 5.25 | 14.44 | INTERFACE |
| <i>WB-F-20-(C)</i> | <i>3</i> | <i>0.5</i> | <i>49.39</i> | <i>16.36</i> | <i>1.91</i> | <i>5.26</i> | <i>CY 1 - IF</i> |

Appendix B - Monotonic DIC Strain Analysis

Strain distributions identified using DIC analysis of representative monotonic specimens are included herein as well as a summary of the total counted strain mode occurrences prior to failure.

B.1 Sandblasted Plain

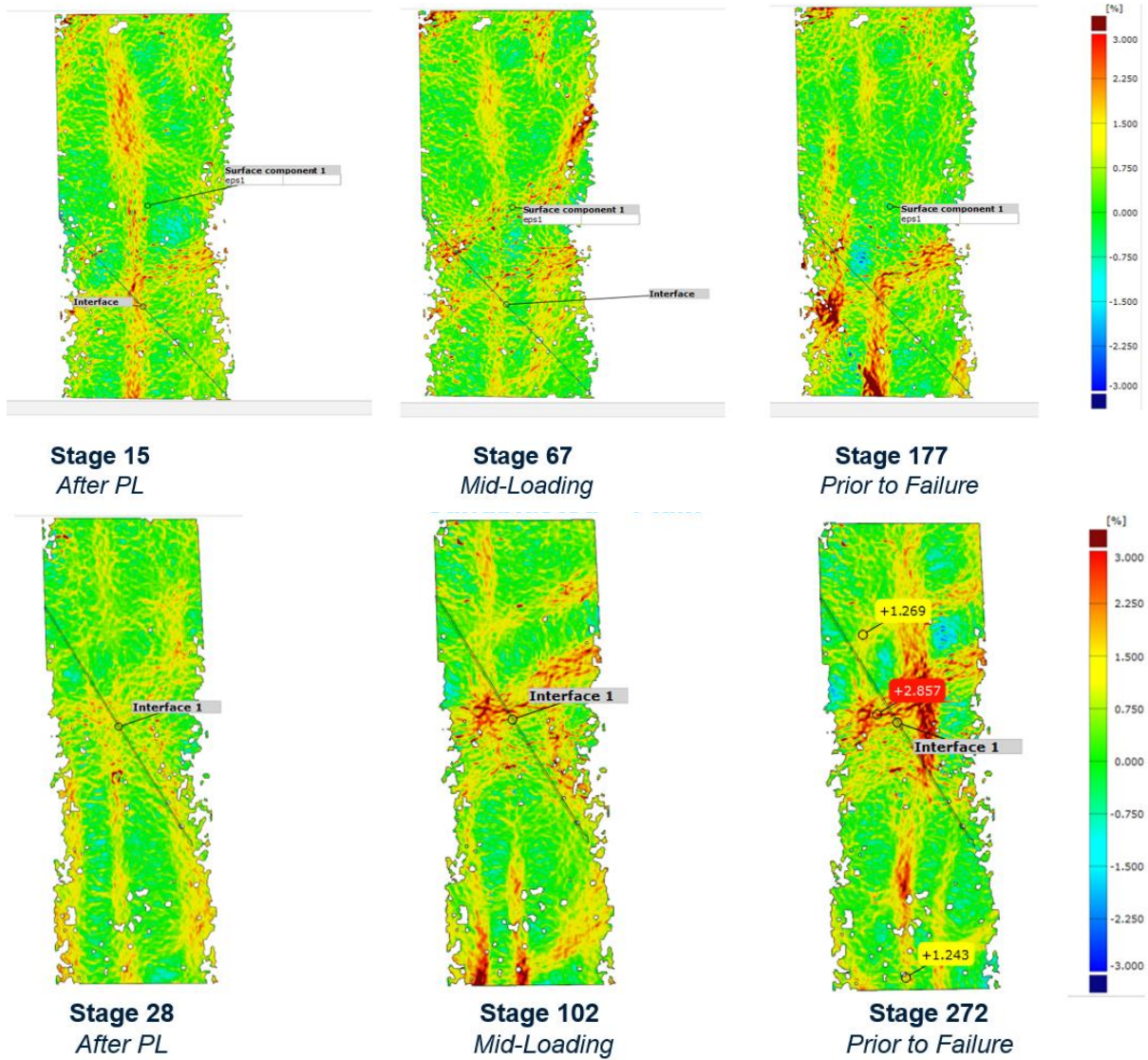


Figure 34: DIC Strain Distribution – Sandblasted Plain Monotonic

B.2 Sandblasted Fiber

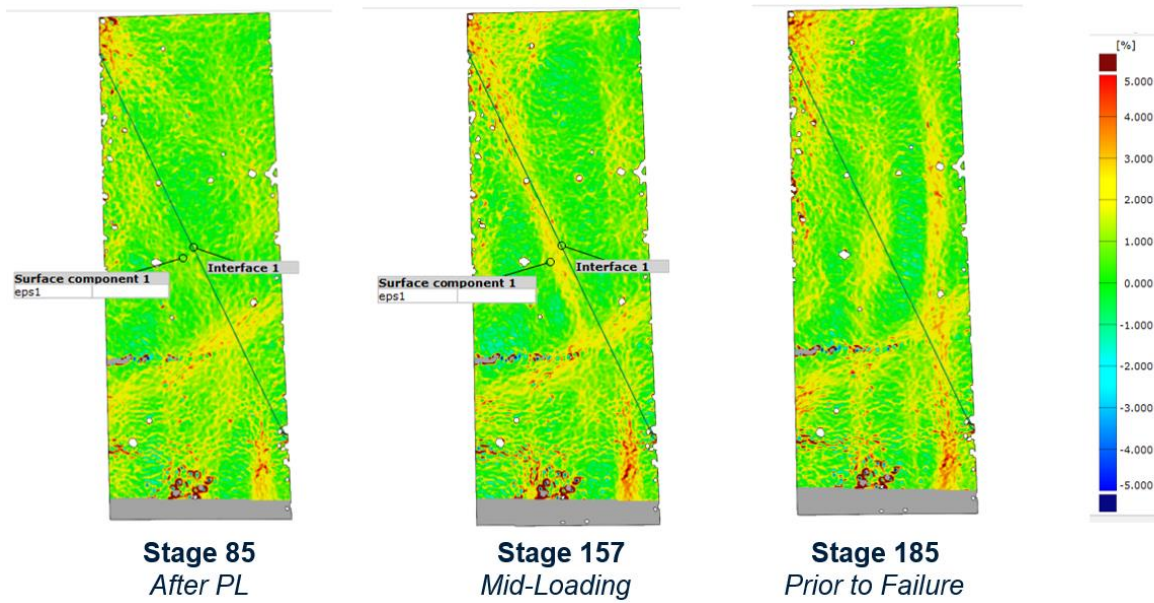


Figure 35: DIC Strain Distribution – Sandblasted Fiber Monotonic

B.3 Wirebrushed Plain

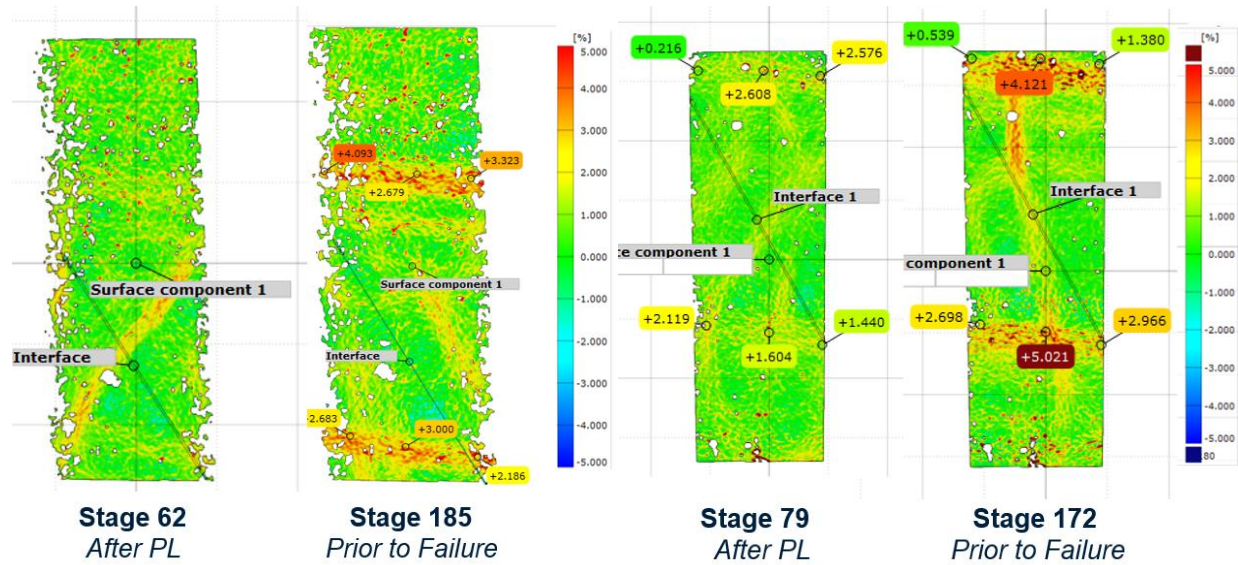


Figure 36: DIC Strain Distribution – Wirebrushed Plain Monotonic

B.4 Wirebrushed Fiber

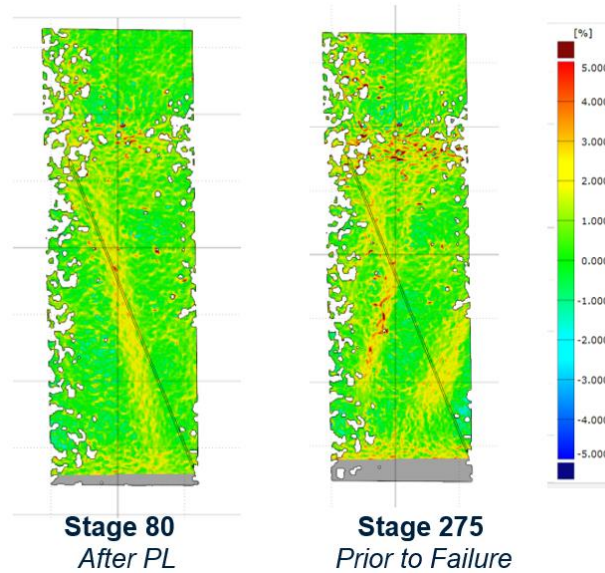


Figure 37: DIC Strain Distribution – Wirebrushed Fiber Monotonic

B.5 Strain Pattern Occurrences

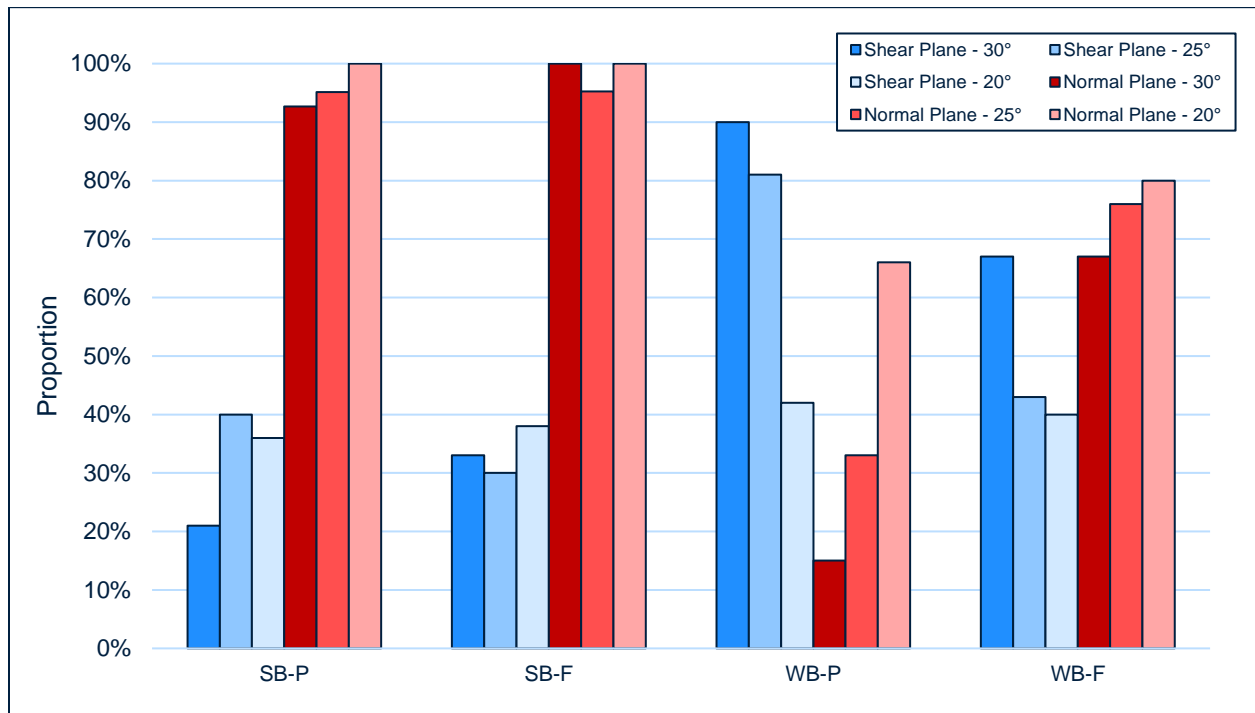


Figure 38: Occurrences of Strain Distribution Modes in Monotonic Specimens prior to Failure

Interpretation of figure:

- **Sandblasted Specimens:** Consistent & high occurrences of strain concentrations representing an adhesive mechanism of bond resistance; Concentrations representing loss of adhesion are less common and not reflective of applied normal stress.
- **Wirebrushed Specimens:** Concentrations representing adhesive bonding mechanism are less frequent, instead concentrations are more descriptive of adhesion loss.
- **Use of Steel Fibers:** generates increase in concentrations representing adhesive bonding, reducing the frequency of adhesion loss in both sandblasted and wirebrushed specimens.

Appendix C - Fatigue DIC Strain Analysis

Strain distributions identified using DIC analysis of representative fatigue-loaded specimens are included herein as well as a summary of the total counted strain mode occurrences prior to failure.

C.1 Sandblasted Plain

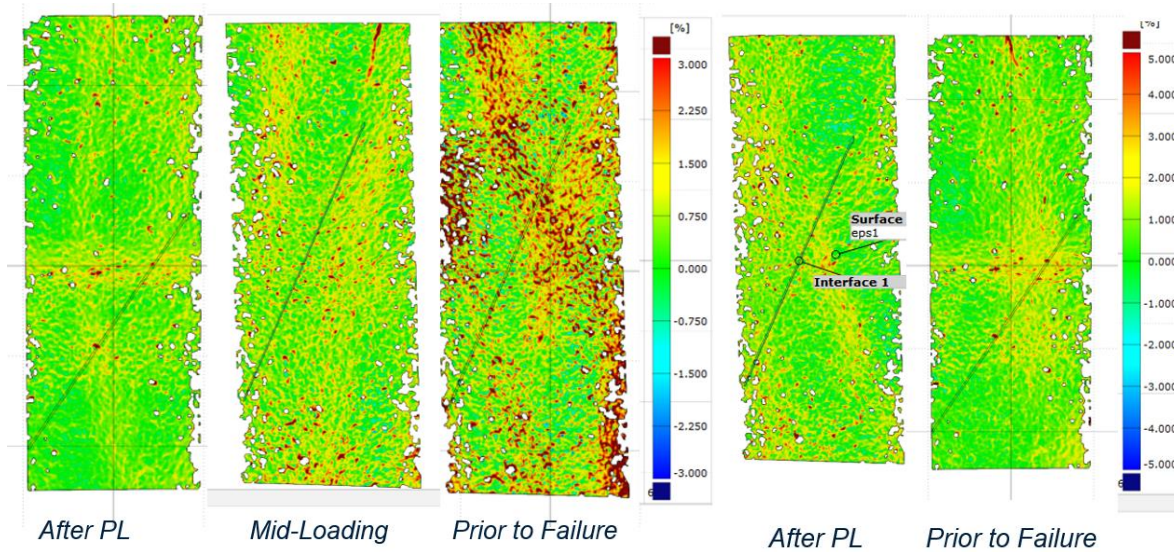


Figure 39: DIC Strain Distribution – Sandblasted Plain Fatigue

C.2 Sandblasted Fiber

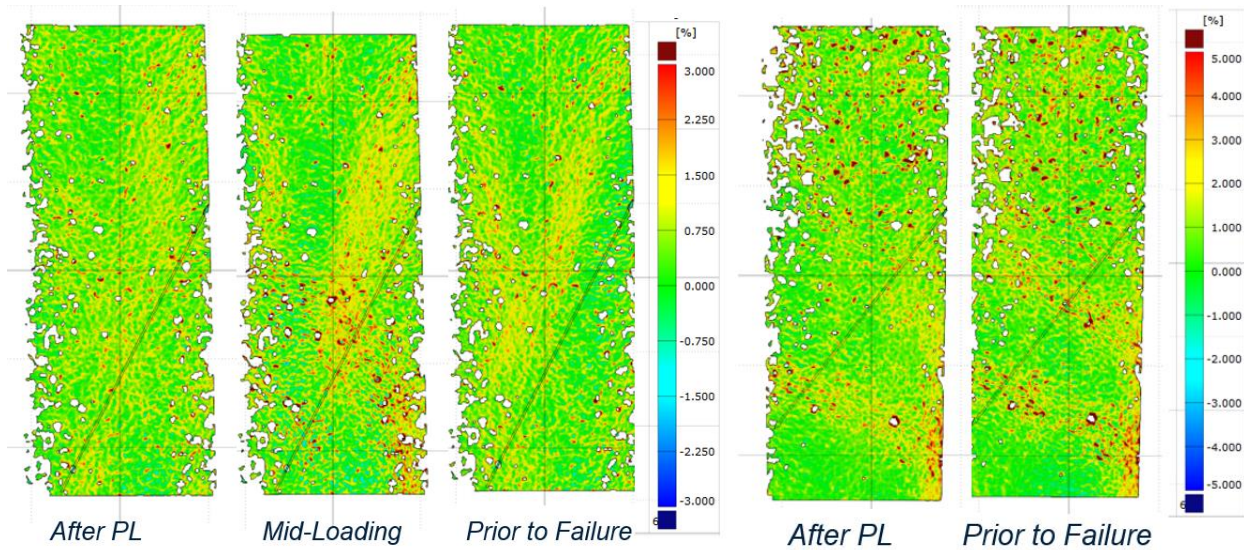


Figure 40: DIC Strain Distribution – Sandblasted Fiber Fatigue

C.3 Wirebrushed Plain

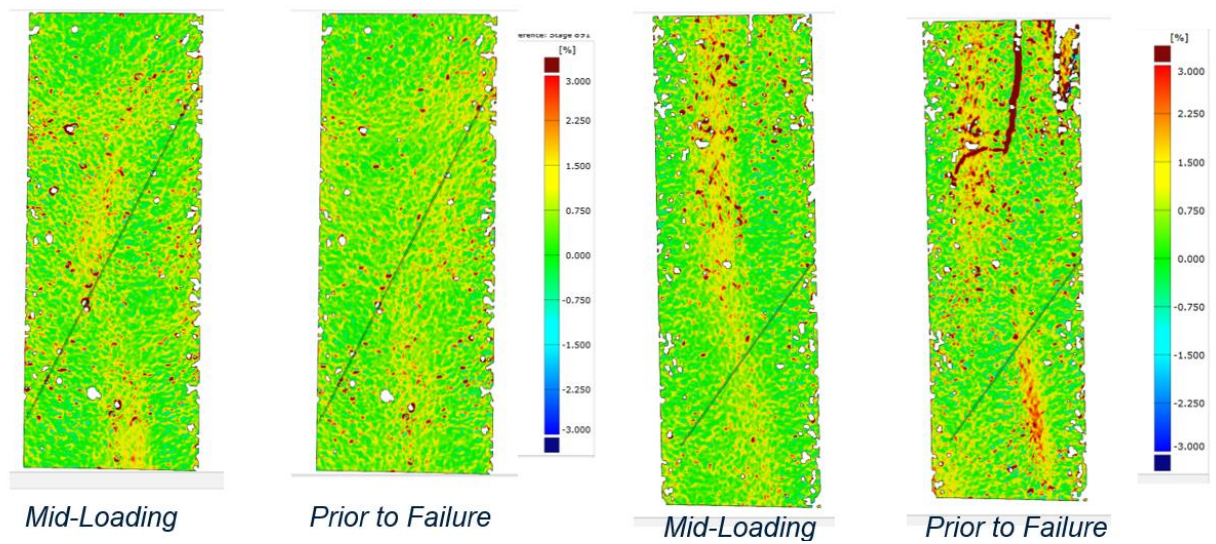


Figure 41: DIC Strain Distribution – Wirebrushed Plain Fatigue

C.4 Wirebrushed Fiber

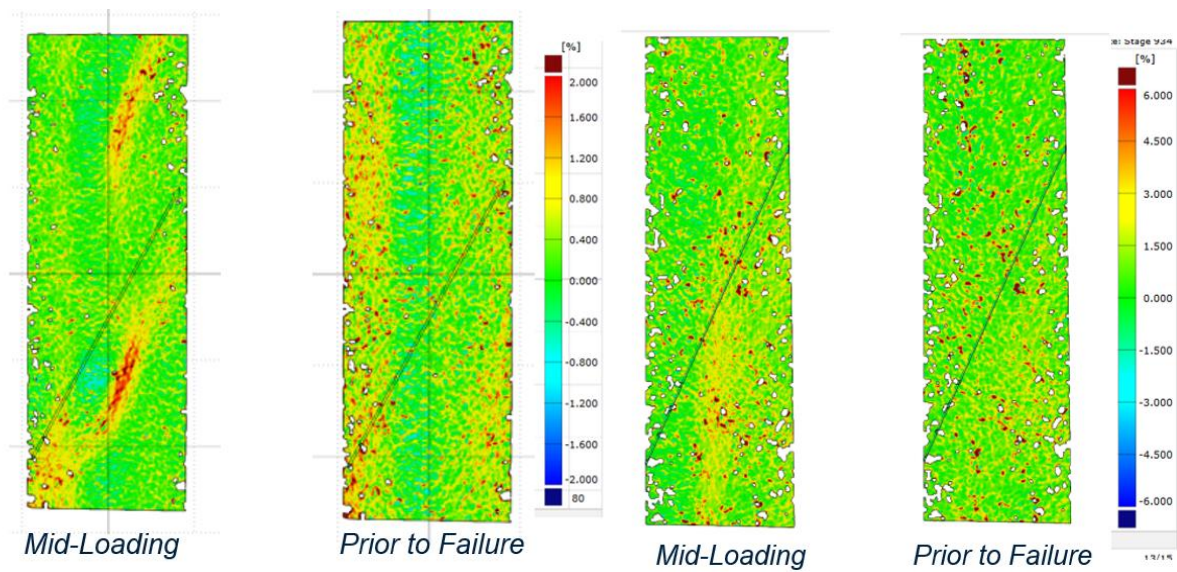


Figure 42: DIC Strain Distribution – Wirebrushed Fiber Fatigue

C.5 Strain Pattern Occurrences

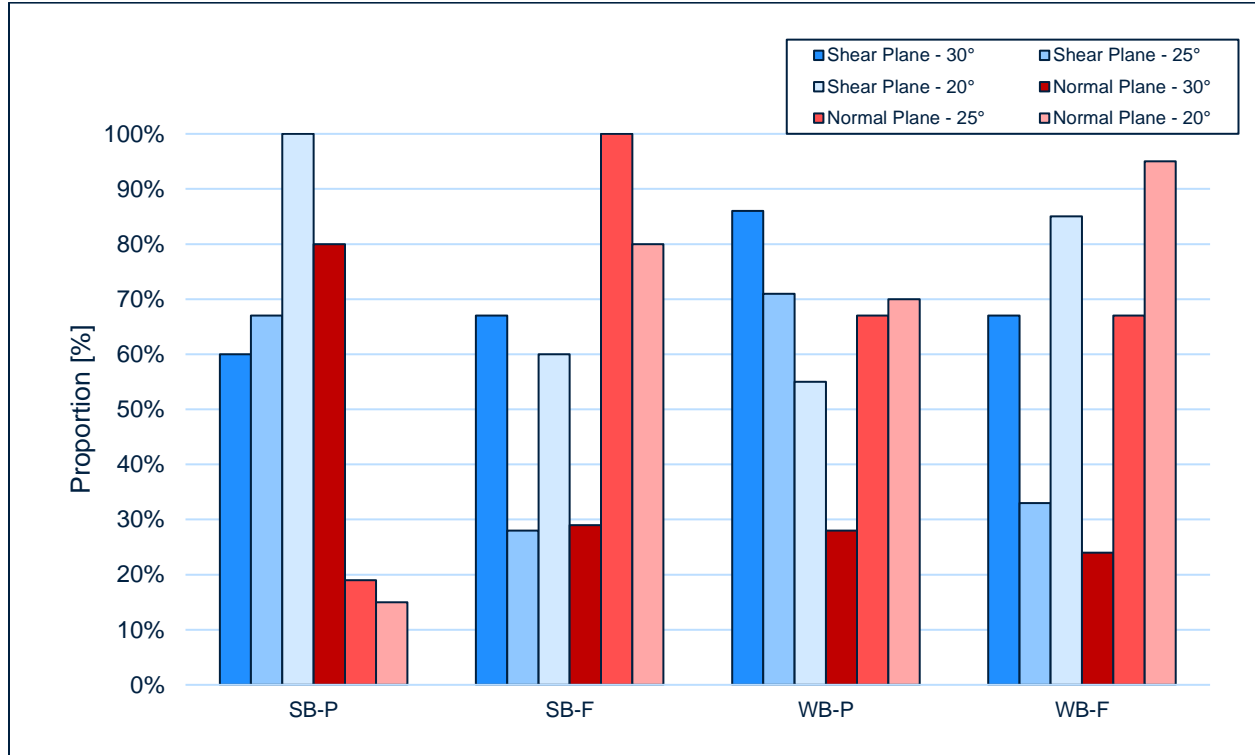


Figure 43: Occurrences of Strain Distribution Modes in Fatigue Specimens prior to Failure

Interpretation of Figure

- **Sandblasted Specimens:** Decrease in occurrences of strain concentration representative of adhesive bond, less common than occurrences representing loss of adhesion in sandblasted-plain specimens especially.
- **Wirebrushed Specimens:** Slight decrease in occurrences representing adhesive bond, changes are less severe than in sandblasted specimens.
- **Fibers:** Result in an increase in occurrences of concentrations representing adhesive bond in both WB and SB, suggesting less degradation of an adhesive mechanism.

Appendix D - Monotonic Failure Envelope Plots

Failure envelopes for individual material types (SB-P, SB-F, WB-P, WB-F) are herein presented for the monotonic loading protocol.

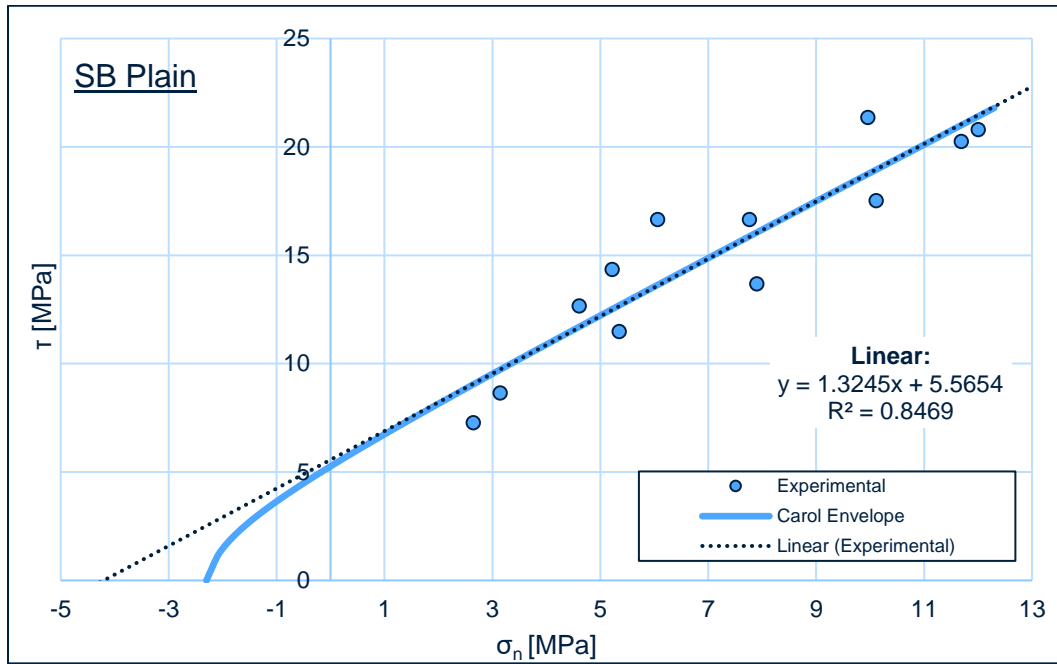


Figure 44: Sandblasted Plain Monotonic Carol & Linear Failure Envelope

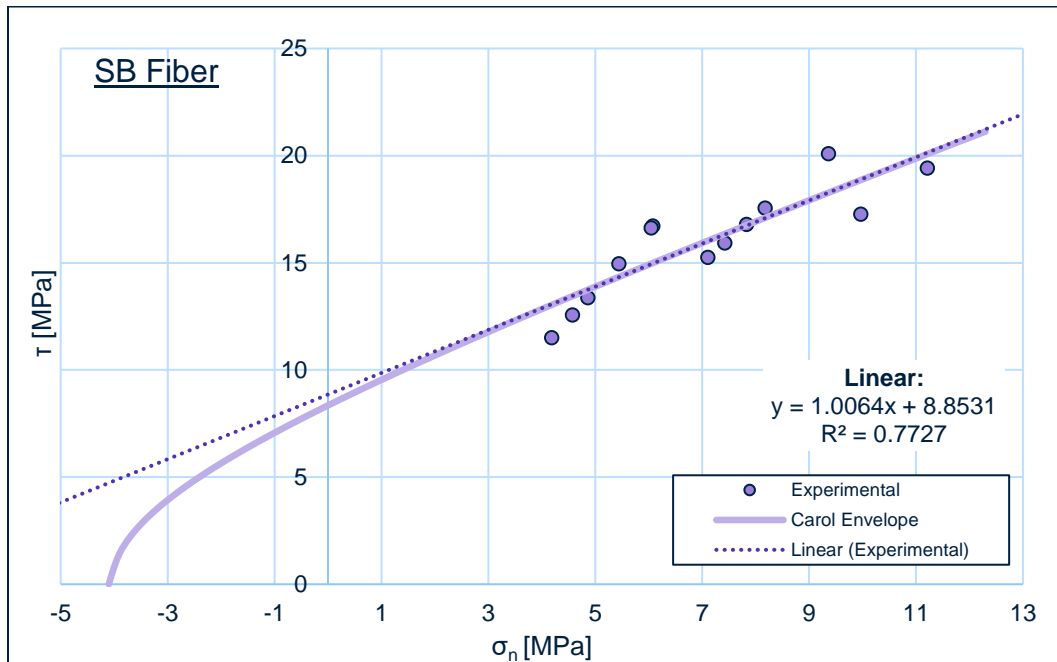


Figure 45: Sandblasted Fiber Monotonic Carol & Linear Failure Envelope

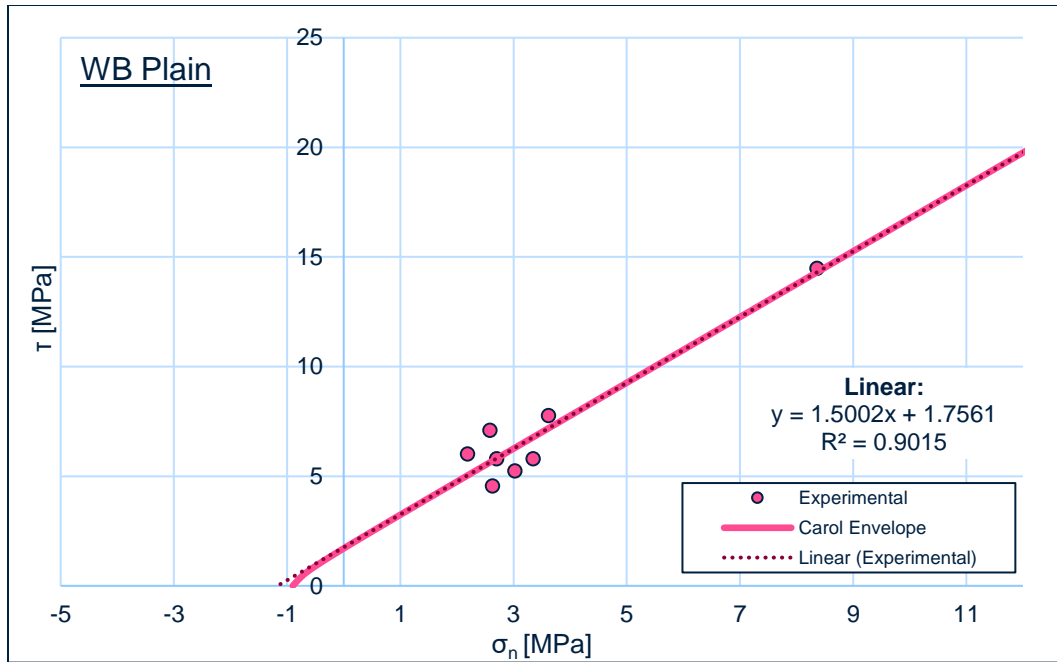


Figure 46: Wirebrushed Plain Monotonic Carol & Linear Failure Envelope

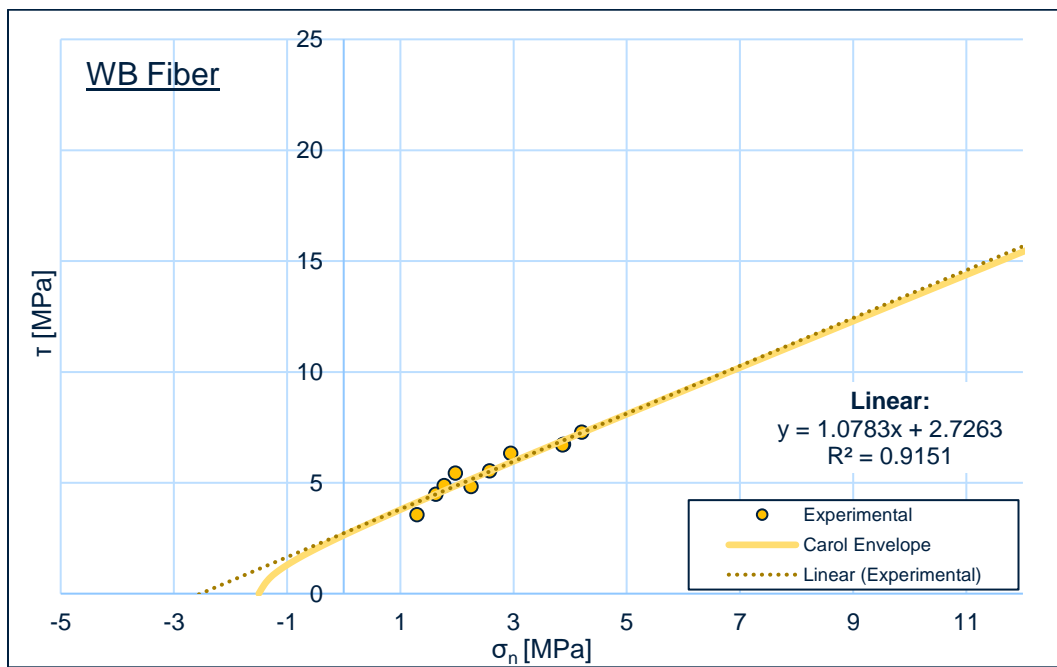


Figure 47: Wirebrushed Fiber Monotonic Carol & Linear Failure Envelope

Appendix E - Modified Failure Envelopes of Validation Data

The modified Carol failure envelopes for slant shear specimens with a “left as cast” smooth interface are presented. Data is courtesy of C.Zanotti & G.Rostagno from a previous experimental investigation at UBC and is presented for validation of the proposed friction angle modification factor.

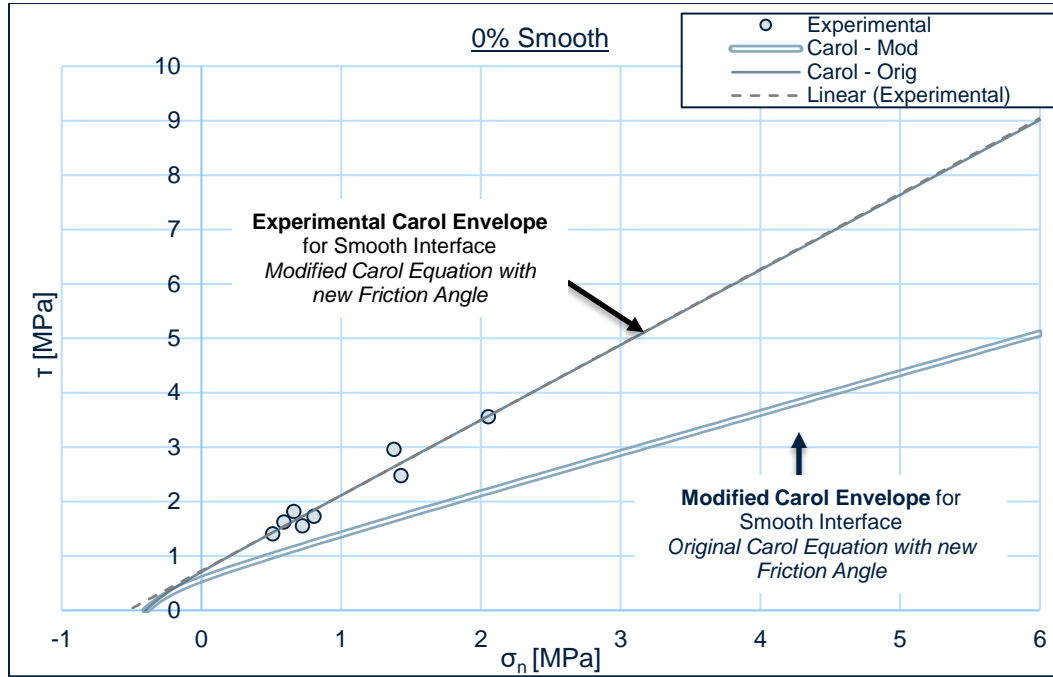


Figure 48: Modified Carol Envelope of Smooth 0% Specimens using Proposed Modification Factor

Table 14: Validation - 0% Smooth Extrapolated Bond Parameters

| Envelope / Equation | c | ϕ | R^2 |
|---|------|--------|-------|
| MC Linear $\tau = 1.3863\sigma_n + 0.7261$ | 0.73 | 54.2 | 0.94 |
| Carol - Original $\tau = \sqrt{(0.75 - \sigma_n \cdot \tan(54))^2 - (0.75 - 0.36 \cdot \tan(54))^2}$ | 0.75 | 54.0 | 0.94 |
| Carol - Modified $\tau = \sqrt{(0.75 - \sigma_n \cdot \tan(1.5 \cdot 36))^2 - (0.75 - 0.36 \cdot \tan(1.5 \cdot 36))^2}$ | 0.75 | 36.0 | 0.94 |

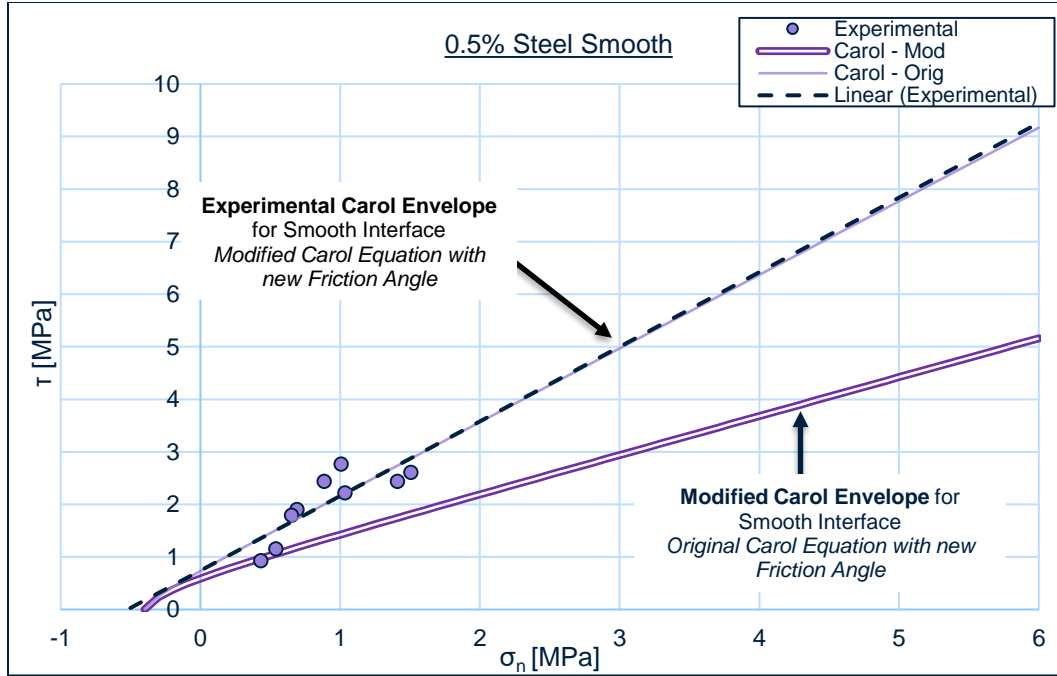


Figure 49: Modified Carol Envelope of Smooth 0.5% Steel Specimens using Proposed Modification Factor

Table 15: Validation – 0.5% Steel Smooth Extrapolated Bond Parameters

| Envelope / Equation | c | ϕ | R^2 |
|---|------|--------|-------|
| MC Linear $\tau = 1.3863\sigma_n + 0.7261$ | 0.74 | 54.8 | 0.68 |
| Carol - Original $\tau = \sqrt{(0.75 - \sigma_n \cdot \tan(54.4))^2 - (0.75 - 0.36 \cdot \tan(54.4))^2}$ | 0.78 | 54.4 | 0.68 |
| Carol - Modified $\tau = \sqrt{(0.75 - \sigma_n \cdot \tan(1.5 \cdot 36.3))^2 - (0.75 - 0.36 \cdot \tan(1.5 \cdot 36.3))^2}$ | 0.78 | 36.3 | 0.68 |